UNIVERSITY OF CALIFORNIA

Los Angeles

On Electron Acceleration at Planetary Foreshocks

A dissertation submitted in partial satisfaction
of the requirements for the degree
Doctor of Philosophy in Geophysics and Space Physics

by

Xiaofei Shi

2024

ABSTRACT OF THE DISSERTATION

On Electron Acceleration
at Planetary Foreshocks

by

Xiaofei Shi
Doctor of Philosophy in Geophysics and Space Physics
University of California, Los Angeles, 2024
Professor Vassilis Angelopoulos, Chair

Shock waves, where supersonic and subsonic plasma flows meet, are primiary sites for charged particle acceleration in various space plasma environments, including astrophysical and planetary bow shocks. Earth's bow shock is the most accessible site for experimental investigations of this acceleration process with in-situ measurements. Relativistic electrons, which are often observed near planetary bow shocks, show energy levels significantly higher than those of solar wind electrons, by at least four orders of magnitude. However, present electron acceleration mechanisms, viewed individually, fail to explain the full energization that electrons undergo in such settings. This thesis presents a compound scenario for such acceleration. Specifically, it investigates the combined role of electromagnetic whistler-mode waves and other plasma wave modes in electron acceleration and scattering in the foreshock region, studied in conjunction with Fermi and betatron acceleration, and applied in a realistic setting, as informed by multi-satellite observations. Whistler-mode waves are known for their role in electron scattering and acceleration in the inner magnetosphere, facilitating our studies of their role under the plasma conditions found in the foreshock. Statistical stud-

ies using in-situ observations from the THEMIS and MMS missions are utilized to reveal the properties of whistler-mode waves and their resonant interactions with electrons near Earth's bow shock and foreshock. Theoretical approaches are then developed to describe the effects of these waves on electron dynamics. Finally, a comprehensive acceleration model is constructed, which successfully replicates the observed near-relativistic electron energy spectra. The model assumes that acceleration to energies up to several hundred keV involves a complex, compound process, including shock acceleration, adiabatic heating, and resonant scattering by multiple plasma wave modes - a phenomenon previously underexplored. The model not only reproduces the observed power-law electron spectrum of $\sim E^{-4}$ but also addresses the longstanding challenge of generating energetic and relativistic electrons at planetary shocks. This extends the theoretical framework of electron-wave interactions from the inner magnetosphere to the foreshock and opens new avenues for numerical simulations of electron acceleration in astrophysical shocks, potentially revolutionizing our understanding of particle acceleration in space plasmas.

The dissertation of Xiaofei Shi is approved.

Anton Artemyev

Jacob Bortnik

Hao Cao

Zixu Liu

Marco CM Velli

Vassilis Angelopoulos, Committee Chair

University of California, Los Angeles

2024

Take courage. Let me tell you all I know.

– Homer's Odyssey

TABLE OF CONTENTS

LIST OF FIGURES

LIST OF TABLES

ACKNOWLEDGMENTS

Completing this dissertation has been a challenging yet rewarding experience, and I could not have done it without the support of my colleagues, friends and family.

First and foremost, I want to thank my advisor, Prof. Vassilis Angelopoulos, for his continuous support, patience, and invaluable feedback throughout the duration of my Ph.D. His dedication to excellence and his mentorship have been instrumental in the completion of this work. I would like to thank Dr. Anton Artemyev and Dr. Terry Z. Liu for their time, effort, and insightful suggestions that helped shape this dissertation into its final form.

I also would like to thank my colleagues and collaborators for their guidance and outstanding feedback.

Lastly, thanks to my friends and family for their encouragement and support.

This thesis is essentially based on the analysis and measurements of the NASA THEMIS mission supported through the contract NAS5-02099.

VITA

2016-2020 B.S. in Space physics, Peking University

2020-2022 M.S. in Geophysics and Space Physics, UCLA

2022-present Ph.D. in Geophysics and Space Physics, UCLA

PUBLICATIONS

1. **Shi, X.**, Artemyev, A., Angelopoulos, V., Liu, T., and Wilson, L., (2024) "Compound electron acceleration at planetary foreshocks", Nature Communication, under review.

2. **Shi, X.**, Artemyev, A., Zhang, X.-J., Mourenas, D., An, X., Angelopoulos, V. (2024). Properties of intense H-band electromagnetic ion cyclotron waves: Implications for quasi-linear, nonlinear, and nonresonant wave-particle interactions. Journal of Geophysical Research: Space Physics, 129, e2023JA032179. https://doi.org/10.1029/2023JA032179

3. **Shi, X.**, Tonoian, D. S., Artemyev, A. V., Zhang, X.-J., and Angelopoulos, V., "Electron resonant interaction with whistler-mode waves around Earth's bow shock I: The probabilistic approach", Physics of Plasmas, vol. 30, no. 12, AIP, 2023. doi:10.1063/5.0172231.

4. Tonoian, D. S., **Shi, X.**, Artemyev, A. V., Zhang, X.-J., and Angelopoulos, V., "Electron resonant interaction with whistler-mode waves around Earth's bow shock. II: The mapping technique", Physics of Plasmas, vol. 30, no. 12, AIP, 2023. doi:10.1063/5.0172285.

5. **Shi, X.**, Artemyev, A., Angelopoulos, V., Liu, T., and Zhang, X.-J., "Evidence of Electron Acceleration via Nonlinear Resonant Interactions with Whistler-mode Waves at Foreshock Transients", The Astrophysical Journal, vol. 952, no. 1, IOP, 2023. doi:10.3847/1538-4357/acd9ab.

6. **Shi, X.**, Liu, T., Artemyev, A., Angelopoulos, V., Zhang, X.-J., and Turner, D. L., "Intense Whistler-mode Waves at Foreshock Transients: Characteristics and Regimes of Wave-Particle Resonant Interaction", The Astrophysical Journal, vol. 944, no. 2, IOP, 2023. doi:10.3847/1538-4357/acb543.

7. **Shi, X.**, Zhang, X.-J., Artemyev, A., Angelopoulos, V., Hartinger, M. D., Tsai, E., & Wilkins, C. (2022). On the role of ULF waves in the spatial and temporal periodicity of energetic electron precipitation. Journal of Geophysical Research: Space Physics, 127, e2022JA030932. https://doi.org/10.1029/2022JA030932

8. Artemyev, A. V., **Shi, X.**, Liu, T. Z., Zhang, X.-J., Vasko, I., Angelopoulos, V., & (2022). Electron resonant interaction with whistler waves around foreshock transients and the bow shock behind the terminator. Journal of Geophysical Research: Space Physics, 127, e2021JA029820. https://doi.org/10.1029/2021JA029820

9. **Shi, X.**, Liu, T. Z., Angelopoulos, V., & Zhang, X.-J. (2020). Whistler mode waves in the compressional boundary of foreshock transients. Journal of Geophysical Research: Space Physics, 125, e2019JA027758. https://doi.org/10.1029/2019JA027758

10. **Shi, X.**, Ren, J., & Zong, Q. G. (2020). The dynamics of the inner boundary of the outer radiation belt during geomagnetic storms. Journal of Geophysical Research: Space Physics, 125, e2019JA027309. https://doi.org/10.1029/2019JA027309

CHAPTER 1

Introduction

1.1 Summary

When the supersonic solar wind meets an obstacle, such as a planet's magnetic field, it slows from supersonic to a subsonic speed and flows around the barrier. This interaction creates a collisionless shock wave, known as the bow shock, where there are sudden changes in speed, temperature, and plasma density. These changes occur as a result of processes such as charged particle acceleration, shock-crossing, and shock-reflection. Reflected particles generate a foreshock region upstream of the bow shock. The foreshock is dynamic, marked by numerous large-scale transient plasma and magnetic field structures and various wave modes. The primary interest in the bow shock and foreshock regions stems from their crucial role in charged particle acceleration.

Shock acceleration is a key process for generating energetic charged particles, especially electrons, in astrophysical systems. However, for this process to operate efficiently, it requires seed electrons with energies above a minimum "injection" level. The injection problem concerns how these high-energy seed particles emerge from the predominantly thermal population in the upstream plasma flow. Solving this problem is a challenge in space plasma physics and astrophysics, as it is essential for uncovering the origins of the universe's most energetic particles. However, investigating astrophysical shocks is challenging because of the lack of direct observations on plasma, waves, and magnetic field configurations at these distant locations. In-situ spacecraft measurements at interplanetary shocks [Dresing et al.,

2016] and planetary bow shocks [Wilson et al., 2016a, Masters et al., 2013] within the heliosphere provide a natural way of testing and exploring particle acceleration models and hypotheses. Earth's bow shock is mostly accessible for such in-situ measurements. Observations suggest that Earth's foreshock, the region upstream of the bow shock, plays an important role in pre-accelerating electrons to seed-electron energies and thus contributes significantly to shock acceleration. However, the precise mechanism by which electrons are pre-accelerated to these seed-electron energies remains an open question.

Although basic theoretical concepts suggest that plasma waves may contribute to electron pre-acceleration, the contribution of foreshock plasma waves on the electron scattering and acceleration process remains relatively unexplored. Foreshock plasma waves exhibit diverse characteristics which complicates their analysis. However, the extensive theoretical and observational knowledge gained on electron resonant interactions with similar wave modes at Earth's inner magnetosphere can provide a solid foundation for investigating similar processes at the foreshock region. An important difference between the bow shock and foreshock transients compared to Earth's inner magnetosphere is the abundance of large-scale field and plasma fluctuations. These render the bow shock and foreshock randomly inhomogeneous, making studies of wave-particle interactions challenging for investigating wave-particle interactions in such environments.

This thesis expands on the role of one of the most widespread wave emissions, electromagnetic whistler-mode waves, in electron acceleration and scattering. Besides whistler-mode waves, this thesis also discusses the effects of other wave modes observed in the foreshocks. The overall goal is to understand how the electrons are accelerated in planetary foreshocks. Towards this goal, we incorporate in-situ observations with theoretical analysis: utilizing in-situ observations we (1) investigate the wave properties in the foreshock region and determine regimes of resonant interactions of electrons and whistler-mode waves, thereby deepening our understanding of their effects on electron dynamics; we then (2) develop a theoretical framework to study these resonant interactions using realistic whistler waves found in the

foreshocks; and finally we (3) build a model to simulate solar wind electron acceleration, incorporating the observations and theoretical model, and considering the effects of different plasma waves, to explain the origin of high-energy (relativistic) electrons observed at planetary foreshocks.

1.2 Background

1.2.1 Shock Acceleration

In collisionless space plasmas, shocks have the capacity to heat and energize charged particles [Jones and Ellison, 1991, Giacalone, 2005, Perri et al., 2022]. Astrophysical collisionless shocks are among the most powerful particle accelerators in the Universe [Koyama et al., 1995, Aharonian et al., 2004, Masters et al., 2013]. Shocks resulting from supernova explosions propagating through the interstellar medium are believed to contribute significantly to the acceleration of galactic cosmic rays [Blandford and Ostriker, 1978, Blandford and Eichler, 1987]. High-energy particles in the vicinity of a shock are scattered by Alfvén waves carried by the converging fluid flow, leading to a first-order acceleration process in which the escape time is comparable to the acceleration time. Emissions associated with ultrarelativistic electrons produced at supernova shocks have been extensively studied using both Earth-based and space-based telescopes [Aharonian et al., 2004]. Galaxy cluster shocks have also been demonstrated to be capable of accelerating electrons [van Weeren et al., 2017]. Galaxy clusters grow through accretion from large-scale filaments and mergers with other clusters and groups. In galaxy clusters, radio sources, also known as radio relics, have been discovered. These regions of diffuse radio emission are believed to be tracers of relativistic electrons in the intracluster plasma, accelerated by low-Mach-number shocks cluster-cluster merger events. Figure 1.1 depicts an observation of galaxy cluster Abell 3411–3412, where radio emission, shown in red, can be used to infer relativistic electrons, and a weak shock with a Mach number below 1.7 is also observed. The discovery of a direct connection between

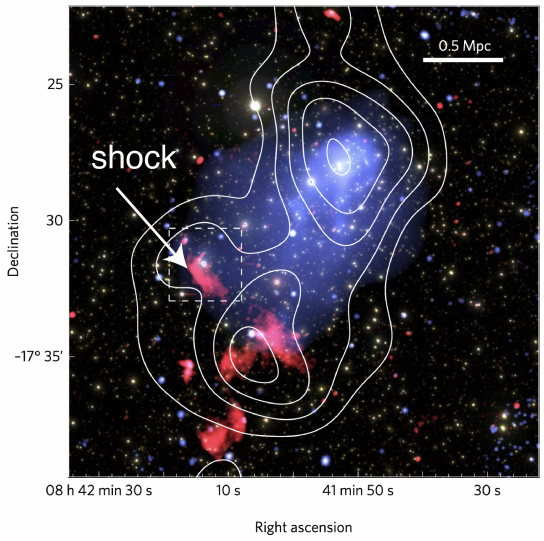

Figure 1.1: Colour image of the merging cluster Abell 3411–3412. Radio emission at 610 MHz is shown in red. The 0.5–2.0 keV Chandra X-ray image is shown in blue. The galaxy distribution is shown with white contours (Figure after [van Weeren et al., 2017])

a radio relic and a radio galaxy in this merging galaxy cluster indicates that radio galaxies in clusters provide seed electrons that can be accelerated and revived (re-accelerated to relativistic energies and able to radiate again through Bremsstrahlung radiation) by shocks [van Weeren et al., 2017].

Studying distant shocks is challenging due to limitations in observations and understanding the details of the shock structure conditions [Treumann, 2009]. Therefore, laboratory experiments can help better analyzing shock acceleration. A study by [Fiuza et al., 2020] utilized results from laser-driven plasma flow experiments, which probe the formation of turbulent collisionless shocks under conditions relevant to young supernova remnants, to study the acceleration process. They generated the shock using laser plasma flow and measured the time-integrated electron spectrum. Figure 1.2 illustrates that when the two flows collide at high Mach numbers, electrons are accelerated up to 500 keV, exceeding the thermal energy of the shocked plasma by more than a factor of 100. Conversely, when only one of the

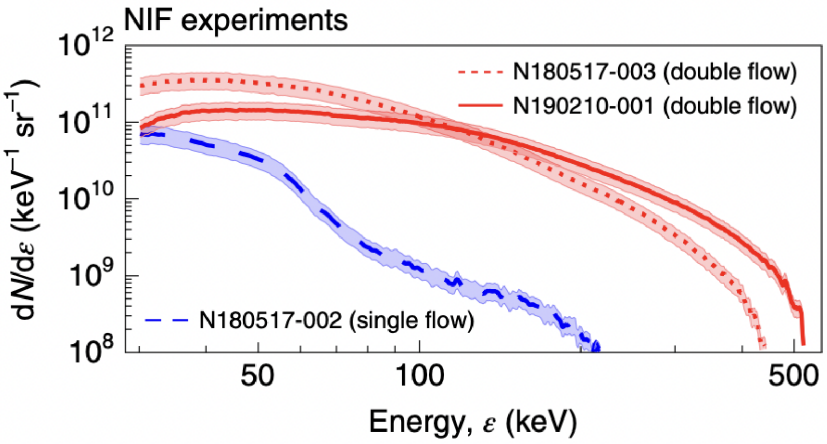

Figure 1.2: Comparison of the measured time-integrated electron spectrum in double-flow (solid and dotted red lines) and single-flow (dashed blue line) experiments indicates that when a shock is formed electrons are accelerated up to 500 keV. N is the number of electrons. (Figure after [Fiuza et al., 2020])

flows is produced (the case of a low Mach number), the measured electron spectrum differs significantly, with electrons exhibiting energies below 200 keV [Fiuza et al., 2020]. This result indicates that shocks with varying Mach numbers exhibit differences in their particle acceleration efficiency. Planetary shocks in the solar system exhibit various Mach numbers and are accessible to in-situ observation for studying shock acceleration.

Planetary shocks form due to the interaction between the solar wind and planetary magnetic fields. Observations made by spacecraft during encounters with collisionless shocks in the solar system can offer valuable insights into the physics of the particle acceleration of shocks. Specifically, planetary shocks have been implicated in electron acceleration up to relativistic energies. The Mach number of shocks typically increases with distance from the Sun. Electrons in Saturn's high Mach number (~ 25) quasi-parallel shock can be accelerated to relativistic energies observed by Cassini spacecraft [Masters et al., 2013, Masters et al., 2016]. Figure 1.3 shows the electron spectra obtained from in-situ observations [Masters et al., 2013], indicating that the electrons can be accelerated up to several hundreds of keV

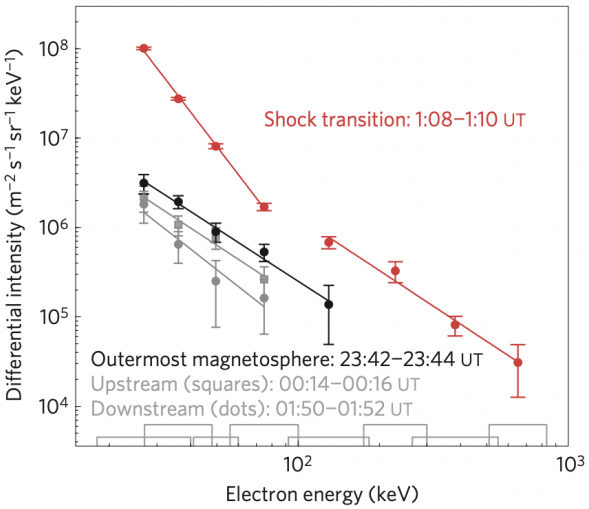

Figure 1.3: Grey rectangles indicate the range of each energy channel. Power-law fits are shown as straight lines. (Figure after [Masters et al., 2013])

with a power-law distribution around the shock. However, in-situ measurements around Earth's bow shock, with a Mach number around 4, also show observations of relativistic electrons with a power-law distribution [Wilson et al., 2016a]. The formation of such a power-law distribution remains to be fully understood. A well-known difficulty is the so-called "injection problem": the effective shock acceleration requires exceeding an energy threshold (well above the electron thermal energy) for electron acceleration [Balogh and Treumann, 2013]. This makes it challenging to explain how thermal electrons can be accelerated to such high threshold energies required to participate in the shock acceleration. The remainder of Section 1.2.1 will discuss the standard mechanism for shock acceleration.

1.2.1.1 Shock Drift Acceleration

Shock drift acceleration (SDA), is due to the drift of particles along the shock surface when they encounter a compressive, collisionless shock. This acceleration results from particles experiencing magnetic drift due to an increase in magnetic field strength across the shock. This drift is aligned with the direction of the convection electric field (in the normal incidence

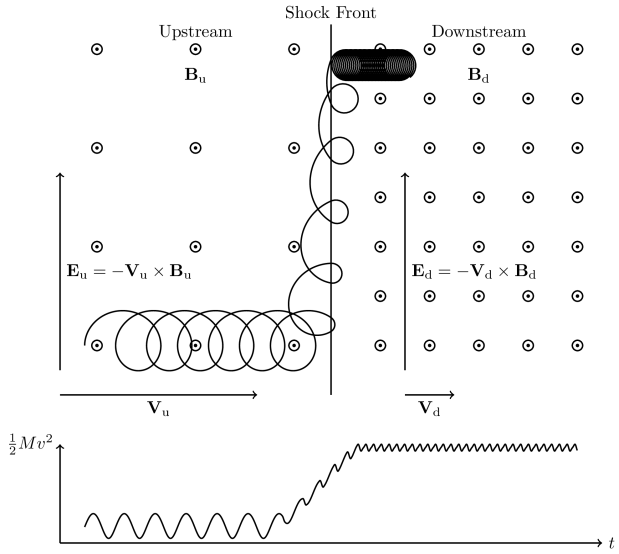

Figure 1.4: Cartoon illustrating shock drift acceleration across a fast mode shock. (Figure after [Ball and Melrose, 2001].)

frame). Consequently, particles can gain kinetic energy as they traverse the bow shock, converting electric potential energy into kinetic energy [Sonnerup and Su, 1967, Terasawa, 1979]. Figure 1.4 illustrates the SDA mechanism: as depicted, the magnetic field, coming out of the page, intensifies from upstream to downstream, thereby reducing the gyroradius of the incoming particle. The particle continues to drift downstream during its repeated encounters with the shock front, until eventually escaping downstream (upstream reflection is also possible). The bottom panel of the figure displays the kinetic energy of the particle over time, demonstrating how energy gain occurs in several discrete steps, coinciding with each shock encounter.

It is commonly understood that the thickness of the collisionless shock transition layer is approximately determined by u_0/Ω_{ci}, where u_0 is the upstream flow speed parallel to the shock normal direction, and Ω_{ci} is the ion cyclotron frequency calculated with the upstream magnetic field strength [Leroy et al., 1982]. For both thermal and suprathermal electrons with gyroradii much smaller than the shock thickness, the adiabatic theory is often considered

a reasonable approximation for electron dynamics. This is because from the perspective of such electrons, the shock appears not as a discontinuity but as a smooth magnetic field gradient. Under this assumption, the first adiabatic invariant $M = m_e v_\perp^2/2B$ (defined with the perpendicular velocity $v_\perp$ and the magnetic field strength B) is constant during the electron interaction with the shock.

The energy increase is most significant for particles that undergo reflection, though particles that pass through the shock can also experience energy gain. To estimate the energy gain from shock drift acceleration, we use the de-Hoffmann–Teller frame (HTF), where the electric field vanishes ($\vec{E} = -\vec{u} \times \vec{B} = 0$) both upstream and downstream and the particle's kinetic energy is also conserved. For electrons that escape downstream, the energy gain can be calculated using the conservation of $M = m_e v_\perp^2/2B$ (the energy gain is proportional to the magnetic field increase downstream, which is about a factor of 4). For electrons that can be reflected from the shock due to the mirror force, their pitch angles should be greater than the loss-cone angle. This reflection results in a finite velocity increase which can be expressed as $\Delta v = 2u_{sh}$, where $u_{sh} = u_0 \cos\theta_{Bn}$ is the upstream plasma flow speed measured in the HTF. This acceleration preferentially increases the parallel energy (the direction along the magnetic field line) of a reflected particle, and therefore, leads to a decrease in the pitch angle. A more precise analysis of the particle energy gain predicts that for a magnetic field increasing by a factor of four, the maximum value of the energy ratio after reflection to initial energy (E_r/E_i) is around 14 [Ball and Melrose, 2001]. Figure 1.5 illustrates a plot of the energy ratio of the reflected particles, indicating that the maximum energy gain is around 14, with a small portion of particles in the phase space being able to achieve such a significant energy increase.

Although SDA can lead to an increase in energy, the energy gain is limited by a maximum factor of 14 [Ball and Melrose, 2001], and the observed fluxes and spectra of energetic electrons cannot be quantitatively explained by SDA alone. Also, the field perturbations near the shock can cause electron pitch-angle scattering, which breaks the assumption of

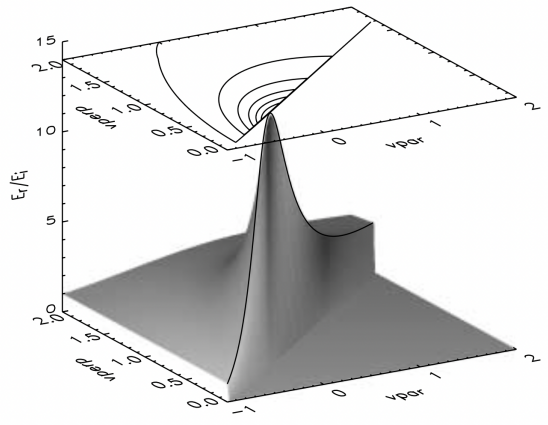

Figure 1.5: Energy ratio for particles reflected upstream from a shock with $B_{down}/B_{up} = 4$, as a function of pre-shock velocity with **vpar** the normalized parallel velocity and **vperp** is the noramlized perpendicular velocity. The lowest contour shown corresponds to an energy ratio of 2, and the contour values increase in units of 2. (Figure after [Ball and Melrose, 2001].)

the first adiabatic invariant. Such pitch-angle scattering may confine a portion of electrons within the shock acceleration region for a longer time and result in an enhancement of energy gain [Vandas, 2001]. This pitch-angle scattering effect is considered in diffusive shock acceleration (DSA) and stochastic shock drift acceleration (SSDA).

1.2.1.2 Diffusive Shock Acceleration and Stochastic Shock Drift Acceleration

The DSA assumes that the particles are scattered by magnetohydrodynamics (MHD) turbulence around the shock front [Blandford and Eichler, 1987]. Efficient resonant pitch-angle scattering, which determines the threshold energy for injection, occurs under certain conditions. Since MHD turbulence has large spatial scales, resonance can occur only when particles gyroradii are comparable to the MHD wavelength. Though pitch-angle scattering via cyclotron resonance with MHD turbulence may occur relatively easily for protons, low-energy (non-relativistic) electrons face challenges in satisfying the resonance condition due

to their small gyroradii. Theoretical considerations suggest that electron acceleration via DSA is inefficient, as low-energy electrons lack opportunities to be scattered.

Stochastic shock drift acceleration (SSDA) overcomes the limitation of DSA by assuming electrons interact with electromagnetic or electrostatic waves (which have a wavelength much smaller than that of MHD turbulence) and the pitch-angle scattering of electrons is confined within the shock transition layer [Amano et al., 2022]. This allows electrons around the transition layer to spend sufficient time near the shock to be accelerated to high energies. The efficiency of SSDA depends on the effectiveness of pitch-angle scattering of electromagnetic or electrostatic waves. Figure 1.6 shows schematics that illustrate the relationship between the DSA and SSDA models [Amano et al., 2020]: Particle acceleration through DSA occurs over a spatial extent much larger than the shock's thickness. Conversely, electrons accelerated by SSDA are confined within the shock transition layer, typically of the order of the ion gyroradius. SSDA has the potential to accelerate subrelativistic electrons due to the presence of intense whistler waves within this transition layer, and these electrons could potentially serve as a seed population for DSA.

Figure 1.7 shows the acceleration of electrons by SSDA in velocity space [Katou and Amano, 2019]. The red curves represent the expected particle trajectory according to the standard SDA. Pitch-angle scattering induces particle diffusion along the blue diffusion curves. The schematic trajectory of an electron accelerated by SSDA is represented by the thick arrows. The contours show the velocity distribution function of the upstream population. Mirror reflection occurs only for particles outside the loss cone, depicted by the gray-hatched area. The work from [Amano et al., 2020] shows that the magnetosonic whistler-mode waves around the shock transition region can scatter electrons via the cyclotron resonance, which leads to electron pitch-angle changes and makes electrons spend longer time in the acceleration region. As the energy increases, the electrons start to interact with lower-frequency larger-amplitude MHD waves. Although SSDA can explain the source of high-energy seed population needed for DSA acceleration, it is mainly effective

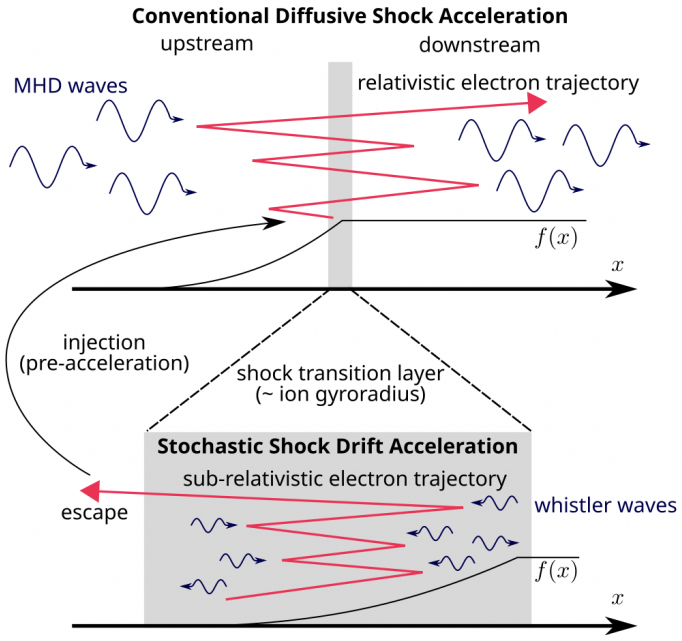

Figure 1.6: Schematics illustrating the relation between conventional diffusive shock acceleration and stochastic shock drift acceleration models. (Figure after [Amano et al., 2020].)

for electrons with $\geq$ 10 keV, which still significantly exceeds the thermal energy of solar wind electrons. Therefore, additional mechanisms are required to accelerate thermal energy electrons.

1.2.2 Bow Shock and Foreshock Transients

Electron acceleration has been observed at planetary bow shocks and their upstream regions. The bow shocks of planetary magnetospheres exhibit curvature, causing variations in shock geometry across its surface even under uniform upstream conditions. The orientation of the interplanetary magnetic field (IMF) significantly influences bow shock physics. In quasi-perpendicular conditions, where the angle between the IMF vector and the shock normal (Θ_{Bn}) exceeds 45°, ions from the incident solar wind are reflected from the shock front and subsequently drift along the IMF to the magnetosheath region behind the shock wave. Under quasi-parallel conditions ($\Theta_{Bn} < 45°$), ions and electrons can drift along the IMF in

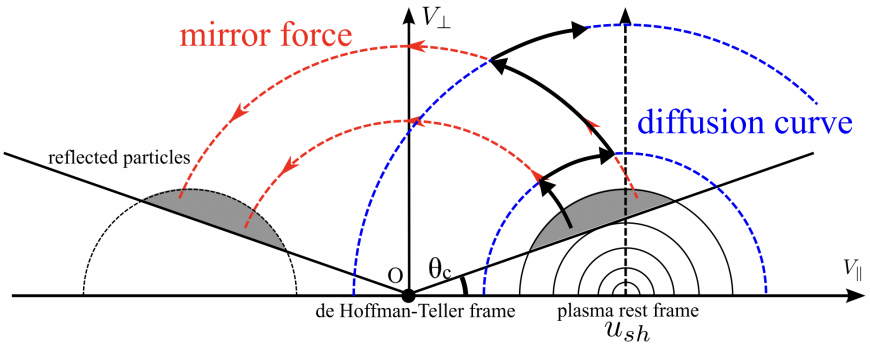

Figure 1.7: Schematic illustration for the particle trajectory accelerated by the SSDA in velocity space.(Figure after [Katou and Amano, 2019].)

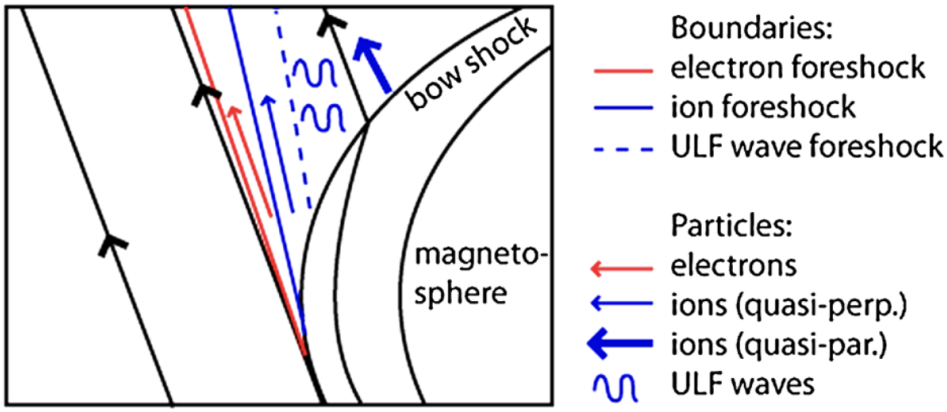

Figure 1.8: Geometry of the bow shock and foreshock from [Eastwood et al., 2005]

the direction opposite to the incident solar wind flow. These suprathermal particles create an extended region in front of the bow shock, known as the foreshock [Eastwood et al., 2005]. Figure 1.8 shows an illustration of a bow shock and its foreshock. In the foreshock, kinetic instabilities develop in the solar wind plasma, generating numerous transient structures and waves that lead to additional particle scattering.

Observations of foreshock transient structures have been reported at different planets, including Mercury [Slavin et al., 2007], Venus [Erickson and Wolf, 1980], Earth [Turner et al., 2013], Mars [Penz et al., 2004], and Saturn [Kivelson and Pu, 1984]. Among these,

Earth's foreshock has been extensively studied due to ample in-situ measurements. The largest transients observed in Earth's foreshock include foreshock bubbles [Omidi et al., 2010, Turner et al., 2013], large-scale kinetic structures resulting from interactions between solar wind discontinuities and suprathermal particles reflected from the shock wave, and hot flow anomalies (HFAs) [Schwartz et al., 1985], which arise from interactions between tangential discontinuities in the interplanetary magnetic field and quasi-parallel bow shocks. Figure 1.9 shows the result of a hybrid simulation of a foreshock bubble located in Earth's foreshock. The formation of the core of the foreshock bubble depends on discontinuities in the interplanetary magnetic field, in which the ions emanating from the bow shock are located. The shock wave is also part of its structure, and the entire structure drifts along with the solar wind approximately in the antisolar direction.

Foreshock bubbles, along with hot flow anomalies, both have a hot, tenuous core associated with strong plasma deflection and are surrounded by compressional boundaries or a shock with a spatial scale of several R_E. The dynamic pressure within the core regions of foreshock transients is significantly lower compared to the surrounding solar wind, and consequently, they can disturb not only the bow shock itself, but also the magnetosheath, magnetopause, and the entire magnetosphere-ionosphere system [Archer et al., 2015]. An example of a foreshock bubble (FB) observed by THEMIS is illustrated in Figure 1.10, revealing a heated and tenuous core with significant flow deflection. As a result of the superfast sunward magnetosonic expansion, a shock forms upstream of the core, and the size of FB in the expansion direction can reach $5 - 10R_E$. In addition to their significant dynamic pressure perturbations, foreshock transients also serve as efficient particle accelerators due to the presence of the shock (e.g., shock drift acceleration and Fermi acceleration as the shock converges towards the bow shock).

Observations have shown that particles can be accelerated inside foreshock transients [Liu et al., 2017b, Wilson et al., 2016a]. Figure 1.11 shows three examples of relativistic electrons produced by foreshock disturbances upstream of Earth's bow shock. Energetic

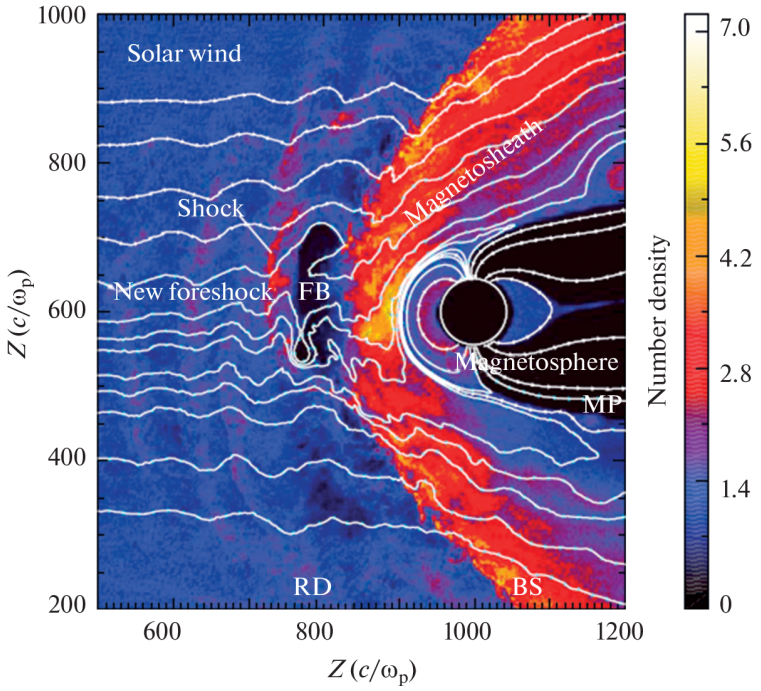

Figure 1.9: Result of hybrid simulation [Omidi et al., 2010] of a foreshock bubble, color indicates proton number density normalized by the solar wind, white lines are magnetic field direction. FB is foreshock bubble, BS is bow shock, and MP is magnetopause. Units of X and Z axes are in skin depth c/ω_p (c is the speed of light, ω_p is plasma frequency). The white circle around Earth indicates the simulation's inner boundary. RD is the position of rotational discontinuity in interplanetary magnetic field.

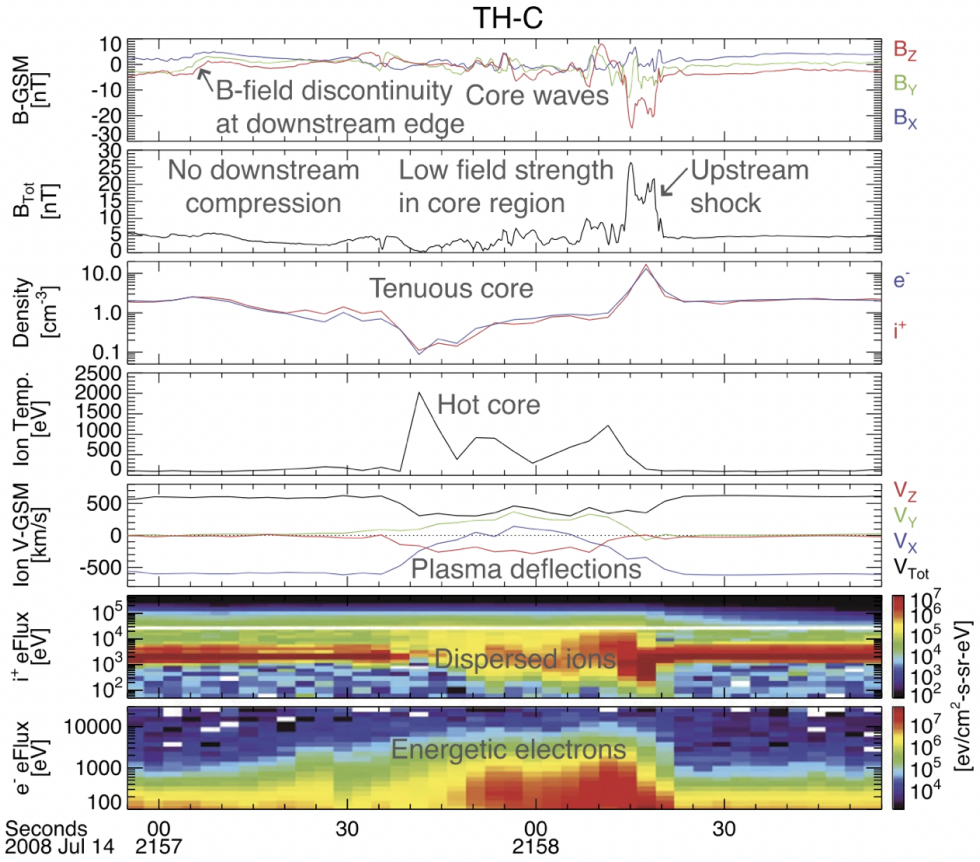

Figure 1.10: A foreshock bubble observed by THEMIS C upstream from the bow shock. From top to bottom: components of the magnetic field in the GSM coordinate system, magnetic field magnitude, plasma ion and electron density, ion temperature, components and magnitude of plasma flow in the GSM coordinate system, plasma ion spectrum, plasma electron spectrum with 3 s time resolution [Turner et al., 2013].

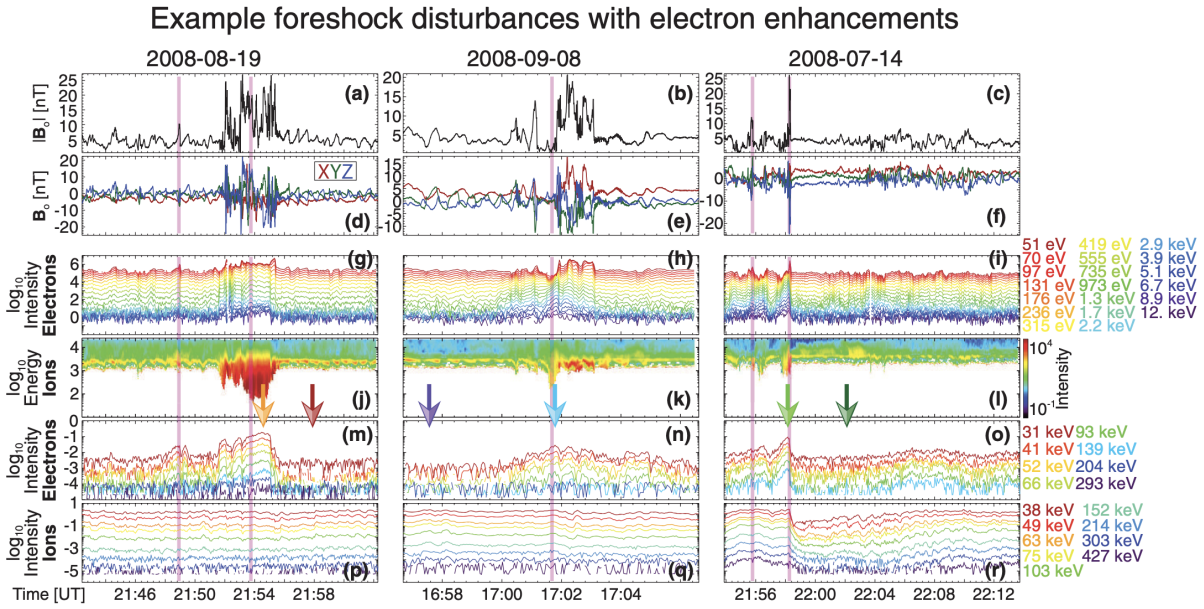

Figure 1.11: Three example foreshock disturbances with energetic electron enhancements from [Wilson et al., 2016a].

($\geq$ 30 keV) electron enhancements are observed as short-duration (tens of seconds to a few minutes) enhancements in the electron fluxes above the background by factors of $\sim$ 10–200. The electron spectra (Figure 1.12) show a power-law form (with $f(E) \propto E^{-4}$) from as low as $\sim$ 0.25 keV up to the highest energies observed during each enhancement (Figure 1.12 (a-c)). The distributions observed outside the enhancements (Figure 1.12 (d-f)) show far more variability, with only noise $>$ 12 keV, and in some cases significant anisotropies. Several mechanisms are proposed for this observed electron acceleration. For example, as a foreshock transient boundary convects earthward towards the bow shock, particles inside the core could bounce between the converging boundary and the bow shock and gain energy through Fermi acceleration [Liu et al., 2017b, Turner et al., 2018]. Other than Fermi acceleration, electrons can also be energized through adiabatic betatron acceleration, caused by the change in magnetic field strength in the foreshock region. [Liu et al., 2019]. However, shock acceleration or adiabatic acceleration (Fermi and betatron) alone cannot explain the generation of near-

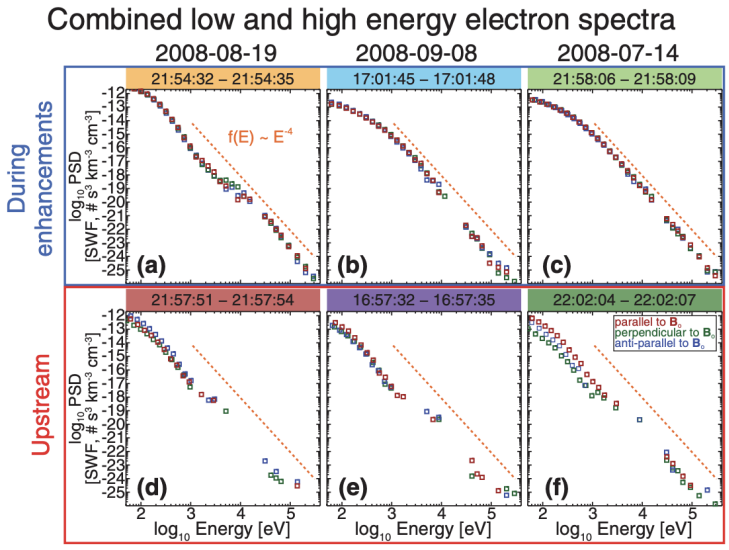

Figure 1.12: Combined low and high energy electron spectra from [Wilson et al., 2016a]. (a)–(c) Distributions during the peak energetic electron enhancements in Figure 1.11. (d)–(f) Distributions in upstream region in Figure 1.11.

relativistic electrons.

Inside foreshock transients, many field fluctuations typically occur. Efficient electron pitch-angle scattering caused by these fluctuations is assumed in the aforementioned Fermi and betatron acceleration models. However, no detailed study has been conducted to analyze the properties of such field fluctuations and exactly how they interact with electrons to affect the acceleration processes. One of the most effective wave modes for electron scattering and acceleration is electromagnetic whistler-mode waves [Gary, 2005, Gurnett and Bhattacharjee, 2005]. These waves can be generated by the heat flux anisotropy [Gary and Feldman, 1977] or the temperature anisotropy of electron distributions [Sagdeev and Shafranov, 1961, Kennel, 1966]. There is good evidence that both types of anisotropy can arise when solar wind electrons interact with the bow shock and foreshock transients [Vasko et al., 2020, Page et al., 2021]. The importance of whistler-mode waves for electron scattering and acceleration has been extensively investigated and discussed in the inner magnetosphere [Horne and

Thorne, 1998, Meredith et al., 2001]. The role of these waves on electron energization around foreshock transients, however, has not been adequately explored or quantified.

1.2.3 Plasma Waves

In collisionless plasmas, various wave modes are generated and have the ability to transfer energy and momentum between waves and particles. These interactions can result in changes in particle energies and pitch angles. We focus on wave modes that interact with electrons, which can include those generated by electron populations themselves or high-frequency waves generated by ions [Sagdeev and Shafranov, 1961, Kennel, 1966]. Extensive research has been conducted on plasma waves in the inner magnetospheric environment, where waves play a significant role in the interactions with radiation belt electrons [Thorne, 2010]. Based on the knowledge obtained from studies in the inner magnetosphere, we can extend our understanding to the foreshock region to investigate waves effects on electron acceleration. In this section, we discuss various wave modes present in the magnetosphere and their impact on electron dynamics. Additionally, we compare the plasma conditions between the inner magnetosphere and foreshock regions.

There is a wide variety of waves in the inner magnetosphere, including whistler mode waves, electrostatic waves, and other nonlinear waves, which can interact with radiation belt electrons and change their dynamics [Thorne, 2010, Li and Hudson, 2019]. These plasma waves are typically generated by plasma injections during geomagnetically active periods [Cornwall et al., 1970, Jordanova et al., 2012, Kennel and Petschek, 1966, Kozyra et al., 1997, Li et al., 2008, Meredith et al., 2013, Malaspina et al., 2015]. Figure 1.13 shows an observation of an injection event and waves associated with the injection [Malaspina et al., 2018]. Panels (a-c) show a plasma injection that transports unstable ion and electron populations around 20:50 UT. Various types of waves are observed near the injection front: electrostatic electron cyclotron harmonics (ECH) generated by loss-cone or beam instabilities, with frequency larger than electron cyclotron frequency [Zhang et al., 2021] (panel (c));

Time domain structures (TDS), electrostatic waves that form nonlinear structures (electron holes, solitary waves) [Mozer et al., 2015] (panel(c)); Electromagnetic whistler-mode waves with frequency smaller than electron cyclotron frequency, are generated by the instability of transversely anisotropic electron population [Zhang et al., 2018a] (Panel (d)); and Kinetic Alfvén waves (KAW), with frequency smaller than ion gyrofrequency, are generated by ion flows and carry a finite field-aligned electric field due to a finite gyroradius effect [Chaston et al., 2012].

Among these wave-modes, the whistler-mode waves are particularly significant in interacting with electrons. Their key role in accelerating and scattering radiation belt electrons during magnetic storms has long been appreciated [Horne and Thorne, 1998, Meredith et al., 2001, Thorne et al., 2013]. In the inner magnetosphere whistler-mode waves are generated by anisotropic electrons injected from the magnetotail [Tao et al., 2011, Fu et al., 2014]. The frequency (ω) of whistler-mode waves is in the range of (Ω_{ci}, Ω_{ce}) where Ω_{ci} is the ion cyclotron frequency and Ω_{ce} is the electron cyclotron frequency; note that the whistler-mode waves with frequency between Ω_{ci} and the lower hybrid frequency $\omega_{LH} = \sqrt{\Omega_{ci}\Omega_{ce}}$ are also called magnetosonic waves. Plasma waves have two key characteristics: wavevector (k) and frequency (ω). The dispersion relation links k and ω via a single equation, offering information about the phase and group velocities that define wave propagation. The dispersion relation under the high-density assumption for whistler-mode waves has been derived as:

$$\omega^2 = \frac{\omega_{ce}^2 \cos^2 \psi}{(1 + (\omega_{pe}/kc)^2)^2} + \frac{\omega_{LH}^2}{1 + (\omega_{pe}/kc)^2} \tag{1.1}$$

where ω_{pe} is the electron plasma frequency, c is the speed of light, and ψ is the wave normal angle which denotes the angle between wave vector k and the background magnetic field. For parallel propagating high-frequency whistler-mode waves, Equation 1.1 can be simplified as:

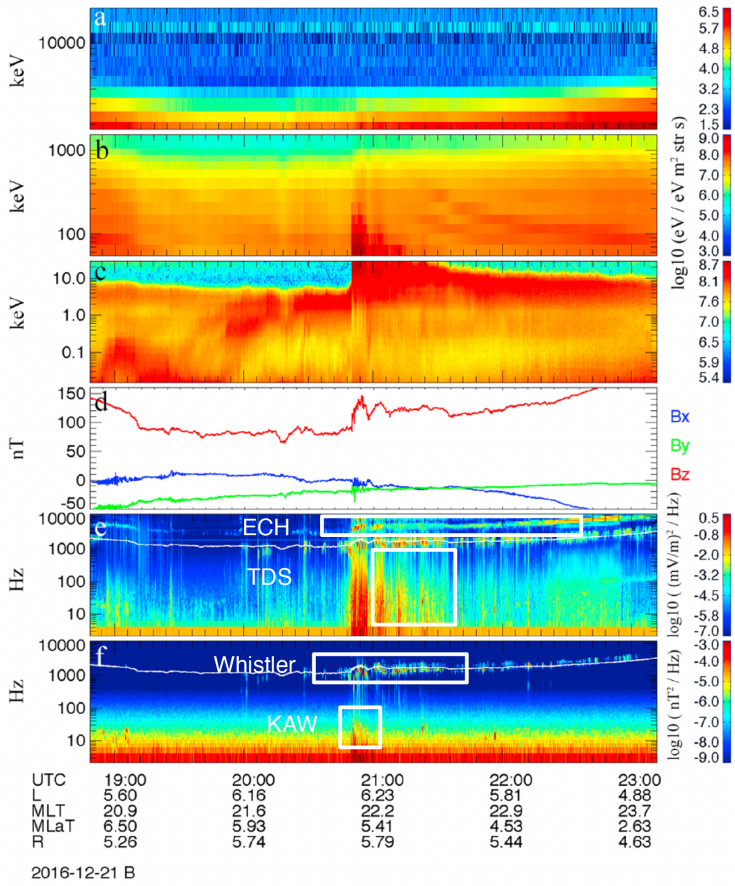

Figure 1.13: Overview of an injection event observed by Van Allen Probe B on 21 December 2016. (a–c) Omnidirectional electron energy flux as a function of electron energy and time from the REPT, MagEIS, and HOPE instruments, respectively. (d) Fluxgate magnetometer data in GSM coordinates. (e) Electric field wave power spectra. (f) Magneticfield wave power spectra. (Figure after [Malaspina et al., 2018]).

$$\omega^2 = \frac{\omega_{ce}^2}{(1 + (\omega_{pe}/kc)^2)^2} \tag{1.2}$$

Theoretical and observational investigations have demonstrated effective interactions between whistler-mode waves and electrons [Lyons and Williams, 1984, Schulz and Lanzerotti, 1974, Millan and Baker, 2012]. These waves, operating at electron scales, exhibit right-hand circular polarization. When these waves are Doppler-shifted such that the electron gyrofrequency aligns with the shifted wave frequency, cyclotron resonance can occur between electrons and whistler-mode waves. The effects of such resonant interactions have been widely studied in Earth's radiation belt for decades.

Whistler-mode waves in the inner magnetosphere can be classified into several categories, including hiss waves, chorus waves, and low-frequency magnetosonic waves. Figure 1.14 demonstrates the spectrogram of these waves, showing various magnetospheric waves that resonate with energetic electrons [Kletzing et al., 2013]. Chorus waves, a type of whistler-mode wave, are commonly observed in the low-density region outside the plasmapause, which marks the outer boundary of the plasmasphere. They often exhibit coherent and discrete elements [Burtis and Helliwell, 1969, Koons and Roeder, 1990, Santolík et al., 2014], with a frequency range typically spanning from $0.1\Omega_{ce}$ to $0.8\Omega_{ce}$ and occur in two distinct bands above and below one-half the electron cyclotron frequency. Chorus waves are recognized for their dual role in radiation belt electron dynamics. They contribute to electron acceleration by facilitating efficient energy diffusion and can also lead to electron precipitation into the upper atmosphere through pitch angle scattering [Bortnik and Thorne, 2007, Ni et al., 2016]. Within the plasmasphere, broadband whistler mode waves, known as plasmaspheric hiss, are prevalent, typically spanning frequencies from 20 to 4000 Hz [Meredith et al., 2004, Meredith et al., 2018]. Hiss waves play a critical role in modulating radiation belt electron dynamics within the plasmasphere by inducing electron precipitation into the upper atmosphere through pitch angle scattering [Meredith et al., 2007, Ni et al., 2013]. In particular, plasmaspheric hiss is crucial for forming the slot region, which lies between the

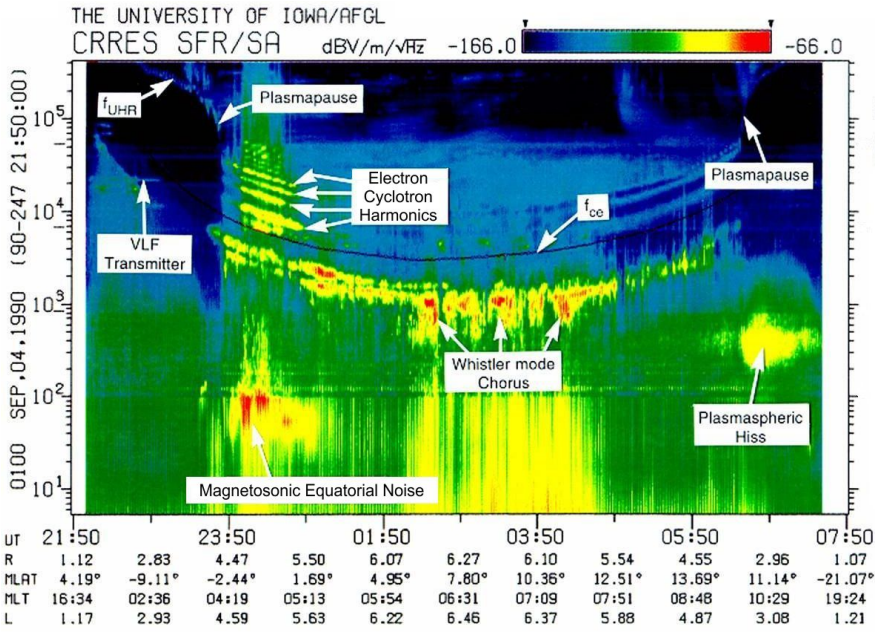

Figure 1.14: Spectrogram of waves observed on Combined Release and Radiation Effects Satellite (CRRES), showing various magnetospheric waves which resonate with energetic electrons (Figure after [Kletzing et al., 2013]).

inner and outer electron radiation belts. Equatorial magnetosonic waves, which fall within the frequency range of ω_{ce} to ω_{LH}, are highly oblique whistler mode waves. These waves are observed in both inner and outer regions of the plasmasphere [Němec et al., 2005, Santolík et al., 2004]. Magnetosonic waves have been proposed as another mechanism for accelerating radiation belt electrons, potentially through Landau resonance and transit-time scattering [Bortnik et al., 2015].

The foreshock and bow shock region also contain various types of plasma waves, including whistler-mode waves, electrostatic waves, and ultra-low-frequency perturbations. Whistler-mode waves have been observed within and upstream of Earth's bow shock [Hull et al., 2012, Oka et al., 2017, Oka et al., 2019]. Because some of them are close to 1 Hz in the spacecraft frame, they are a type of magnetosonic waves, which are often referred to as "1-Hz waves". These waves propagate obliquely and are either left-hand or right-hand polarized

in the spacecraft frame. The source of these waves was believed to be shock-reflected ions [Hoppe and Russell, 1980] or electron beams[Tokar et al., 1984]. Some whistler waves at higher frequencies ($>$ 10 Hz) have also been observed at Earth's bow shock [Lalti et al., 2022b] and in the foreshock region [Shi et al., 2020]. These waves propagate either parallel or obliquely to the magnetic field and tend to become more parallel as their frequencies increase. The whistler-mode waves may play an important role in the scattering and acceleration of electrons in the foreshock region. Other than whistler-mode waves, ultra-low-frequency perturbation, and electrostatic waves are also frequently observed in the foreshock region [Zhang et al., 2022, Kamaletdinov et al., 2022]. These waves may also play a role in electron scattering and acceleration. We will discuss the combined effects of different wave modes in Chapter 5.

Table 1.1: Comparison between foreshock and radiation belt

	Foreshock transient	Outer radiation belt
Backgroud field strength	$\sim 5-50$ nT	>100 nT
ω_{pe}/ω_{ce}	~ 100	<10
Electron energy	$10-100s$ eV	$10s-1000s$ keV

Plasma conditions in the foreshock differ from those in the inner magnetosphere. The foreshock is characterized by backstreaming solar particles with considerably lower energy compared to those in the radiation belt, and the magnetic field in this region is also weaker. Table 1.1 presents a comparison of plasma parameters between foreshock transients and the outer radiation belt. Despite these differences, extensive theoretical and observational studies on electron resonant interactions with plasma waves in the Earth's inner magnetosphere provide a solid basis for exploring how these interactions facilitate electron acceleration in the foreshock. Detailed observations and theoretical analyses of whistler mode waves in foreshock regions, and their impact on electron acceleration, will be discussed from Chapter 2 to Chapter 4.

1.3 Thesis Organization

The overall goal of this thesis is to understand how electrons are accelerated in planetary foreshocks and the role of waves in electron acceleration. To that end, this work is organized into the following 6 chapters.

Chapter 1 begins by contextualizing the injection problem of shock acceleration and addresses why studying resonant wave-particle interactions between waves and electrons is important for electron acceleration in planetary foreshocks. Particle acceleration has been observed around astrophysical shocks, laboratory shocks, and also planetary shocks. Accessible in-situ measurements for planetary shocks, especially at Earth's bow shock and foreshock regions, provide ample observational dataset to study one of the most mysterious parts of shock acceleration, the injection problem. Current models can partially resolve the injection problem but still cannot fully explain the observed acceleration from thermal energy up to relativistic energies. This thesis examines the impact of plasma waves in the foreshock region on electron scattering and acceleration, which play a crucial role in the formation of near-relativistic electrons observed in foreshock regions.

Chapter 2 and Chapter 3 discuss one of the most important wave modes, the whistler mode. Chapter 2 shows the observations and statistical characteristics of whistler-mode waves in the foreshock region. It also shows the efficiency of wave-particle interactions and the potential of nonlinear interactions between waves and particles due to the intense whistler wave activities. Chapter 3 focuses on the theory of nonlinear effects by deriving the equations of motion for nonlinear resonant wave-particle interactions. Importantly, wave packet sizes can affect the efficiency of nonlinear interactions, and the observed waves mostly propagate in short wave packets. We conduct test-particle simulations including the size of wave packets to show that electrons can be accelerated by nonlinear interactions with waves.

Although test particle simulations can trace the electron dynamics, they require a large amount of computational time, especially when studying the dynamics of a large population

of electrons in realistic plasma conditions, including varying initial energies, frequencies, and distributions of wave amplitudes. Therefore, Chapter 4 discusses a theoretical probabilistic approach and a mapping technique that can reproduce electron dynamics in an analytical way without time-consuming test-particle simulations. The probabilistic approach uses the Monte Carlo method to trace electron dynamics, allowing for the incorporation of realistic distributions of wave characteristics and background plasma conditions. We further develop the probabilistic approach in Chapter 5 to include multiple components that influence electron dynamics during the acceleration process. Chapter 5 proposes a compound acceleration mechanism by including the effect of waves, shock acceleration, and adiabatic heating to reproduce the high-energy tail observed in the foreshock region.

Chapter 6 summarizes the topic and discusses the future direction of including the effects of magnetic pumping and oblique whistler-mode waves.

CHAPTER 2

Whistler-Mode Wave Properties in Foreshock Transients

2.1 Introduction

Recent observations of energetic electrons in Earth's foreshock transients [Wilson et al., 2016b, Liu et al., 2017a] suggested that such transients can accelerate electrons and may provide a seed population for further acceleration at the bow shock – the main source of energetic particles at the dayside. Around the bow shock and inside foreshock transients there are many field fluctuations and waves that could either directly accelerate electrons or modulate other acceleration processes (e.g., Fermi and betatron acceleration) [Oka et al., 2019, Lichko and Egedal, 2020]. Foreshock transients also exist at other high Mach number quasi-parallel shocks (e.g., at outer planets, where the solar wind Mach number is high, or occasionally even at Mars, [Collinson et al., 2015]). The studies of these waves are therefore, by analogy, likely common and significant for electron acceleration inside foreshock transients in planets and in other astrophysical contexts (such as at supernova shocks which can produce cosmic rays). One of the most effective wave modes for electron scattering and acceleration is electromagnetic whistler-mode waves [Gary, 2005, Gurnett and Bhattacharjee, 2005]. They can be generated by heat flux anisotropy [Gary and Feldman, 1977] or temperature anisotropy [Sagdeev and Shafranov, 1961, Kennel, 1966] that arises when solar wind electrons interact with the bow shock and foreshock transients [Vasko et al., 2020, Page et al., 2021]. Whistler-mode waves are frequently observed around the bow shock [Hull et al.,

2012, Oka et al., 2017, Oka et al., 2019, Amano et al., 2020]. However, the role of these waves on electron energization in foreshock regions remains to be fully understood.

In this chapter, we statistically evaluate the properties of whistler-mode waves and determine the regimes of resonant interactions between waves and electrons. In-situ measurements around Earth's bow shock allow us to examine these waves in great depth, facilitating the extension of findings to other planetary foreshocks with similar plasma conditions.

2.2 Observations

2.2.1 Data and Instrument

For observations, we used the dataset from the Time History of Events and Macroscale Interactions during Substorms (THEMIS) mission [Angelopoulos et al., 2008] and the Magnetospheric Multiscale (MMS) mission [Burch et al., 2016]. THEMIS mission contains five identically instrumented probes (TH-A, TH-B, TH-C, TH-D, and TH-E) launched in 2007. We examined TH-C data from 2008 to 2009 when TH-C was within the foreshock during the dayside phase. We analyze magnetic field data from its fluxgate magnetometer (FGM) [Auster et al., 2008], plasma data from its electrostatic analyzer (ESA) [McFadden et al., 2008], electric field data from its electric field instrument (EFI) [Bonnell et al., 2008], and magnetic fluctuation data from its search coil magnetometer (SCM) [Roux et al., 2008]. We selected events with foreshock transients from 2008 to 2009 and focused on those encompassing onboard triggered wave burst mode data (SCM data up to 4 kHz). MMS mission consists of four identical satellites in a tetrahedral configuration. The low-frequency magnetic field is measured by the fluxgate magnetometer (FGM) [Russell et al., 2016] and the high frequency by the search coil magnetometer (SCM) [Le Contel et al., 2016] at a rate of 128 S/s and 8192 S/s, respectively, while in burst mode (as is the case here). The fast plasma investigation (FPI) [Pollock et al., 2016] instrument provides ion and electron measurements at a resolution of 150ms and 30ms, respectively (also in burst mode).

We focus on whistler-mode waves observed around HFAs and FBs, two types of foreshock transients with the most significant plasma and field fluctuations. Whistler-mode waves occur regularly within and around them. Such transients occur at least ten times per day, particularly during conditions of above-average solar wind speed [Lu et al., 2022, Chu et al., 2017a]. Both transient types have a hot, tenuous core associated with strong plasma deflection. HFAs are surrounded by compressional boundaries on either side, while FBs have an upstream compressional boundary bounded by their own mini-shock. They have a scale of one to several Earth radii (R_E). Figure 2.1 (a) shows a sketch of an HFA that forms in response to an approaching solar wind discontinuity. The hot plasma generated in the core expands and the large-gyroradius hot foreshock ions at its edge form the core compressional boundaries at its two sides. Whistler-mode waves are observed in the core and compressional boundaries. The HFA moves anti-sunward along the bow shock (downward in the figure); the dashed blue line shows the spacecraft trajectory relative to the HFA.

We identified HFA and FB using the following criteria: (1) they have a hot core with one or two compressional boundaries; (2) inside the core, density, velocity, and field strength are reduced, but temperature is increased; (3) compressional boundaries are accompanied by a sharp increase in magnetic field strength and density. Figure 2.1(b-f) represents an observation of a typical HFA with two compressional boundaries. Quasi-parallel propagating whistler waves, evidenced by an increase in wave power are observed within the compressional boundaries and on the edge of the core (Figures 2.1i-j). The observed whistler waves coincide with increases in the electron perpendicular temperature anisotropy (Figures 2.1 (g) and (h)).

2.2.2 Wave Analysis Technique

For whistler waves analyzation, we use the power spectral density (PSD) to determine the mean frequency ($\langle f \rangle$) and the frequency width (Δf) of whistler waves:

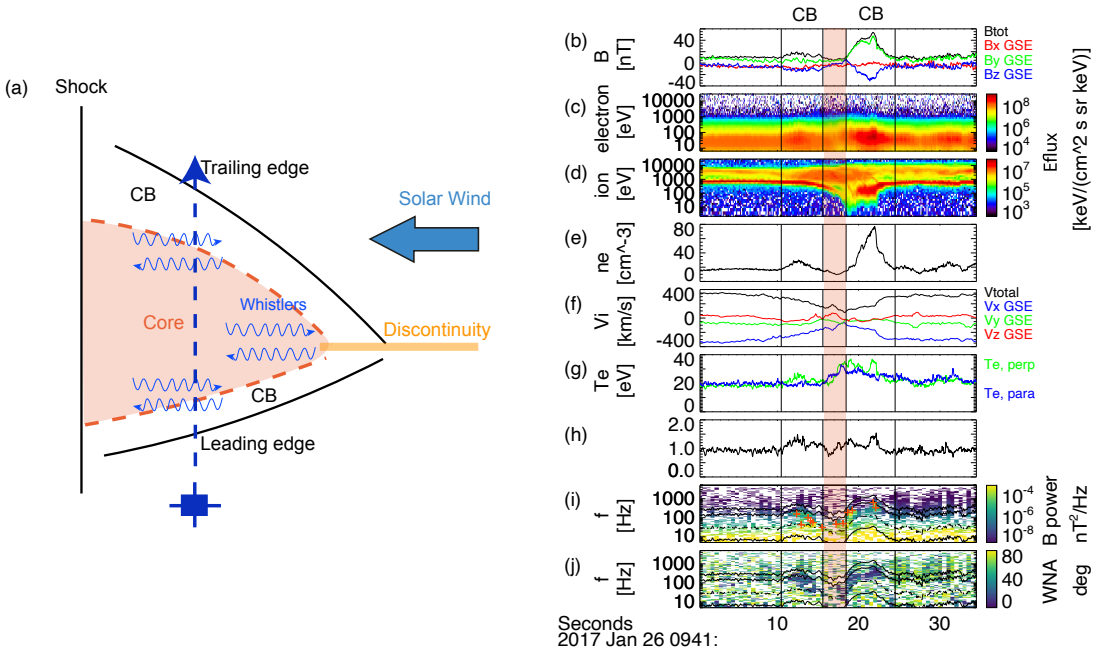

Figure 2.1: (a) Sketch of an HFA cross-section in the HFA reference frame, at an instant in time as it moves along the shock, past a spacecraft (down). The HFA's hot plasma core is flanked by compressional boundaries (CB). Whistler waves are observed around the edge of the core. The blue dashed line shows the spacecraft trajectory (up) relative to the HFA in this frame. (b) Magnetic field, (c,d) Energy flux of electrons and ions, (e) Electron density, (f) Plasma velocity, (g) Electron perpendicular temperature and parallel temperature, (h) Electron temperature anisotropy ($T_\perp/T_\parallel$), (i) Magnetic field power spectral density (red crosses depict mean frequency determined as discussed in the text), and (j) Wave normal angle. The core of the HFA is demarcated by the orange-shaded region.

$$\langle f \rangle = \frac{\int_{f_{low}}^{f_{ce}} PSD_w f df}{\int_{f_{low}}^{f_{ce}} PSD_w df} \tag{2.1}$$

$$(\Delta f)^2 = \frac{\int_{f_{low}}^{f_{ce}} PSD_w (f - \langle f \rangle)^2 df}{\int_{f_{low}}^{f_{ce}} PSD_w df} \tag{2.2}$$

where $PSD_w(f) = PSD(f) - PSD_b(f)$, and $f_{low} = max\{4Hz, f_{lh}\}$. PSD is averaged over every 0.5s and PSD_b is the background power spectrum (partly due to instrument noise), subtracted here in order to detrend the spectrograms and better reveal the waves. This background spectrum was obtained at each frequency by averaging all times when the PSD fell to $< 30\%$ of its average in each event. We used the 0.5-s (corresponding to 2 Hz) time interval for PSD, and therefore, we used 4 Hz ($2 \times 2Hz$) as the lower frequency limit. Using the wave frequency $\langle f \rangle$ and the frequency width Δf, we compute the average wave amplitude ($\langle B_w \rangle$) and maximum wave amplitude (B_w) from band-pass filter data in each 0.5s wave interval.

Using timing and MVA (minimum variance analysis, see [Sonnerup and Cahill, 1968, Sonnerup and Scheible, 2000]) methods to determine the magnitude and direction of the wave vector ($\vec{k}$), we then calculated the wave normal angle and the wave frequency in the plasma frame by correcting for its Doppler-shift relative to the spacecraft frame (note that all wave properties have been averaged at each wave measurement which is defined as the consecutive series of time points when $\int_{f_{low}}^{f_{ce}} PSD_w df > 0$). MMS provides four-point observations from close separations. As the plasma frequency (f_{pe}) in foreshock transients is usually around 10^4Hz, the wavelength ($\lambda = 2\pi/k \sim 10s$ km) is comparable to the average separation between the MMS satellites. Therefore, the timing method can be applied to directly obtain the value and direction of $\vec{k}$ [Paschmann and Schwartz, 2000a, Turner et al., 2017]. For a coherent wave signal, $\vec{k}$ obeys the following linear equations:

$$\begin{pmatrix} R_{12x} & R_{12y} & R_{12z} \\ R_{13x} & R_{13y} & R_{13z} \\ R_{14x} & R_{14y} & R_{14z} \end{pmatrix} \begin{pmatrix} k_x \\ k_y \\ k_z \end{pmatrix} = \begin{pmatrix} \Delta\phi_{12} \\ \Delta\phi_{13} \\ \Delta\phi_{14} \end{pmatrix} \tag{2.3}$$

where R is the separation between two satellites; $\Delta\phi = 2\pi\delta t/T$ is the phase difference between two satellites, where δt is the lag time corresponding to the peak cross-correlation and T is the observed period of the wave. The peak cross-correlations between the wave fields observed by four satellites allow us to assess the accuracy of the results. We applied the timing method at each wave measurement. For measurements with cross-correlation > 0.8 we then calculated the mean wave frequency in the plasma frame: $2\pi f = 2\pi\langle f\rangle - \vec{k}\cdot\vec{v_p}$, where $\vec{v_p}$ is the plasma (ion) velocity. If the cross-correlation is smaller than 0.8, we applied an alternative method (MVA) to calculate the wave vector.

While the timing method, used above, can directly measure the magnitude and absolute direction of $\vec{k}$, it requires coherent four-point measurements of the wave fields. For this reason, we also used the one-point MVA technique to estimate the orientation of $\vec{k}$ when the timing method is not applicable. The MVA method calculates the principal variance directions and their associated eigenvalues [Paschmann and Schwartz, 2000a]. The direction of $\vec{k}$ is the minimum variance direction. To ensure that the minimum variance direction is well determined and the waves are circularly polarized, we only kept the points with $\lambda_{int}/\lambda_{min} > 10$ (referring to the ratio of intermediate to minimum eigenvalues). We then used the wave dispersion relation to compute the wave number ($|\vec{k}|$) for the waves of interest [Wilson et al., 2013]. The 180° ambiguity in the $\vec{k}$ direction in the MVA method can be eliminated by using the Poynting vector $\vec{S}$ to determine the direction of $\vec{k}$ even for oblique waves [Verkhoglyadova et al., 2010, Verkhoglyadova et al., 2013] – we computed $\vec{S}$ using both electric and magnetic field data [Wilson et al., 2013] for all our events and determined the sign of wave propagation for MVA-computed $\vec{k}$ values. We then used this $\vec{k}$ to compute the Doppler-shifted wave frequency in the plasma frame from the MVA method.

2.2.3 Statistic Characteristics

Whistler waves were observed in 85% of all foreshock transient events in our database. The wave spatial distribution within the foreshock transients (in the core or the compressional boundary) is important because it highlights where the waves are preferentially generated and where they may interact with electrons. To reveal the spatial distribution of whistler waves, we normalized the time interval of the core region to $[0, 1]$, based on crossing times specific to each event. The leading and tailing boundaries were located at normalized times ≤ 0 and ≥ 1, respectively. As mentioned previously, the compressional boundary forms along the edge of the foreshock and is characterized by the enhanced magnetic field and plasma density. We defined the edge of the boundary by where the magnetic field magnitude equals the background value, where the background field was calculated by averaging the magnetic field strength in the relatively quiescent region upstream of each foreshock transient. (For example, in Figure 2.1 (b), the edges of the compressional boundary are shown by vertical lines.) Note that FBs usually only have one trailing boundary. Therefore, the normalized FB event cores starting at position 0 are typically not preceded by a foreshock compressional boundary. Figures 2.2 and 2.3 depict the superposed epoch analysis of whistler wave properties and their spatial distribution in foreshock transients versus the normalized time (to be interpreted as the spatial location within the core, or relative distance from the core boundaries).

Figures 2.2(a,b) show the number histograms of the normalized mean frequency ($\langle f \rangle / f_{ce}$) in the core and in the compressional boundary regions of our events, respectively. The median frequency in both regions is around $0.2 f_{ce}$. The spatial distribution (versus normalized time) of $\langle f \rangle / f_{ce}$ is shown in Figure 2.2(c). The solid and dashed black lines are the mean and median values of $\langle f \rangle / f_{ce}$; they are $\sim 0.2 f_{ce}$ at all locations, despite the sharp change of the background magnetic field strength and density at the compressional boundary. This indicates a local generation mechanism for most of the observed waves.

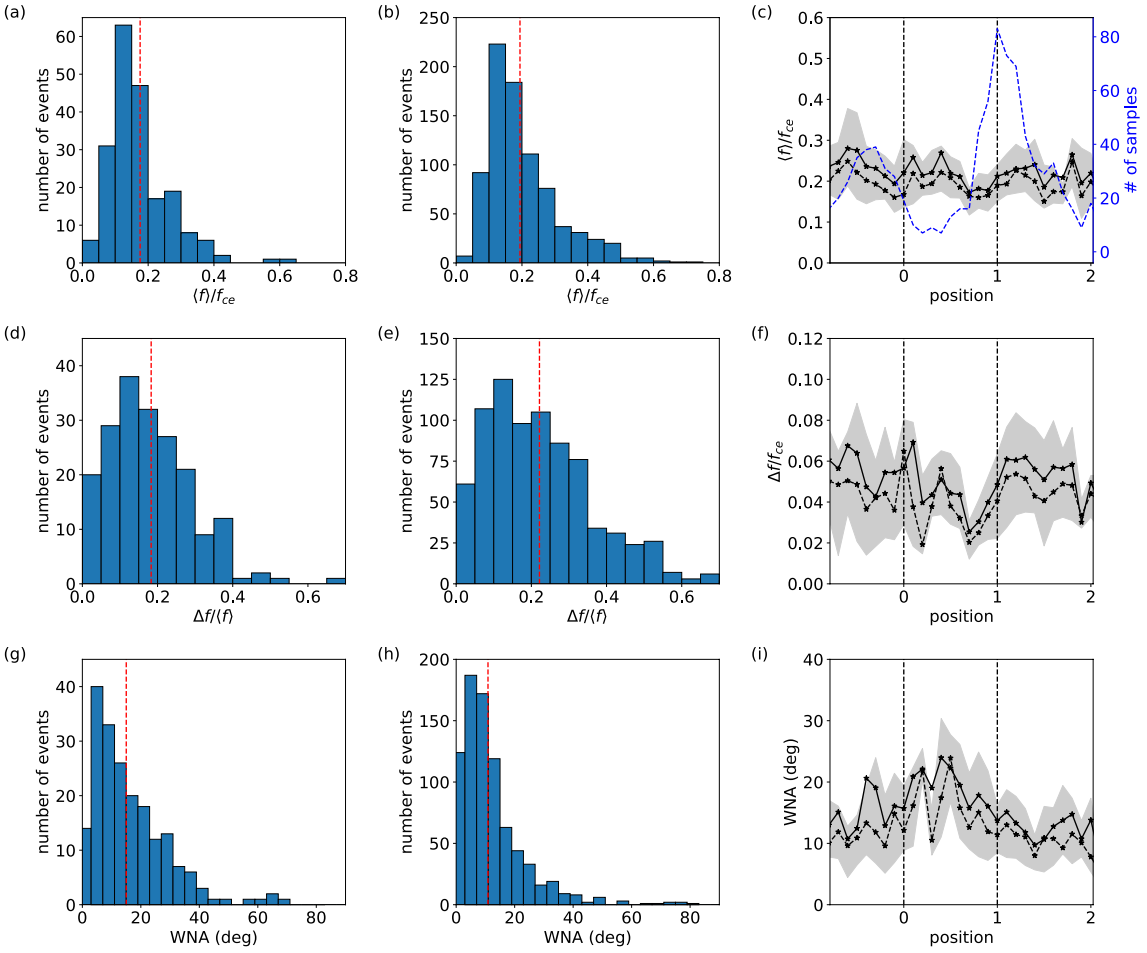

Figure 2.2: The number histograms and spatial distribution of (a-c) wave frequency; (d-f) wave frequency width normalized to mean frequency; and (g-i) wave normal angle. The left and middle columns show histograms in the core and in the compressional boundaries, respectively. Dashed red lines are medians. The right column shows average and median values, in solid black lines and dashed black lines, respectively; the lower and upper bound of the shaded region represents the 25^{th} and 75^{th} percentile of the data, respectively; the dashed blue line in Panel (c) is the number of whistler waves observed at different locations.

There are more waves with $\langle f \rangle / f_{ce} \geq 0.3$ observed in the core, than in the boundary (compare Figures 2.2(a) and (b)). Although this difference between the core and boundary $\langle f \rangle / f_{ce}$ distribution is not large (less than 15% of total number of observations), it may imply that some fraction of the waves observed in the core, especially with $\langle f \rangle / f_{ce} \in [0.3, 0.5]$, may be generated within the boundaries and then propagate to the core region. Because the core region is characterized by smaller background magnetic fields, when whistler waves propagate into it, their relative frequency ($\langle f \rangle / f_{ce}$) increases.

The dashed blue line in Figure 2.2(c) shows the number of events with whistler waves as a function of position. It is equivalent to the spatial statistical distribution of the waves as a function of location within the foreshock transient. It shows that whistler-mode waves are most probable near the edge of the core where the magnetic field gradient is large. More events are located near position=1 versus position=0 mainly due to the following reason: the trailing boundary (at ≥ 1 region) is usually stronger (with higher magnetic field strength) than the leading one for foreshock transients. This feature has been shown in previous observations and simulation studies [Liu et al., 2016, Vu et al., 2022a], and Figure 2.1 is also an example. As a result, the change of the magnetic field strength is sharp at the region around 1 but smoother around 0. The wave generation is favorable in the region with a large field gradient where magnetic field compression drives the transverse electron heating required for wave generation, and therefore, is more likely to be observed around position $\sim$1.

Figures 2.2 (d-f) show the number histograms and spatial distribution of the normalized wave frequency width ($\Delta f / \langle f \rangle$) in a similar manner as the frequency panels, Panels (a-c) above. The median value of $\Delta f / \langle f \rangle$ is ~ 0.2 in the core and in the compressional boundaries. A large portion of the observed waves are quite narrow-banded, which suggests a narrow resonance energy range of electrons responsible for wave generation, i.e. the anisotropic electron population is bounded below and above in energy by isotropic cold and hot electrons, respectively [Fu et al., 2014, Page et al., 2021, Frantsuzov et al., 2022].

The number histograms and the spatial distribution of wave normal angles are shown in Figures 2.2(g-i) in a similar format as the panels above. Most whistler waves are quasi-parallel propagating, and the waves tend to be more oblique in the core region: the medians increase from 12° in the boundary to 16° in the core (Panels (h) and (g)), and this is also evident in the spatial profile of both the medians and means in Panel (i). This is likely a result of (1) wave propagation to the core region from the boundaries (whistler wave propagation in the inhomogeneous magnetic field and plasma results in a wave normal angle increase, see [Shklyar et al., 2004, Chen et al., 2013, Gu et al., 2021]) or (2) oblique wave generation within the core by either cyclotron or Landau resonance thanks to the suppression of Landau damping by the large parallel temperature often observed in that region (see discussion of such oblique wave generation by, e.g., [Li et al., 2016]).

Number histograms and spatial distribution of the normalized maximum wave amplitude (B_w/B_0) in our events are shown in Figures 2.3(a-c), in a format similar to Figure 2.2. Here, B_0 is the background magnetic field strength - typically $\sim 5-10s$ nT in HFAs and FBs. The median value for B_w/B_0 in both core and compressional boundaries is larger than 0.01. Thus, the maximum wave amplitude can reach $10s-100s$ of pT. The mean wave amplitude (not shown here) is about 3 times smaller than the maximum value in statistics.

2.3 Wave-Particle Interactions

2.3.1 Resonant Interactions

Once we have established the primary whistler wave properties, our next step is to investigate the interactions between these waves and electrons. When the waves are Doppler-shifted (i.e. electron parallel velocity is modified) such that the electron gyrofrequency can resonate with the wave frequency in the electron rest frame, energy is transferred between waves and electrons. This resonance condition is defined as:

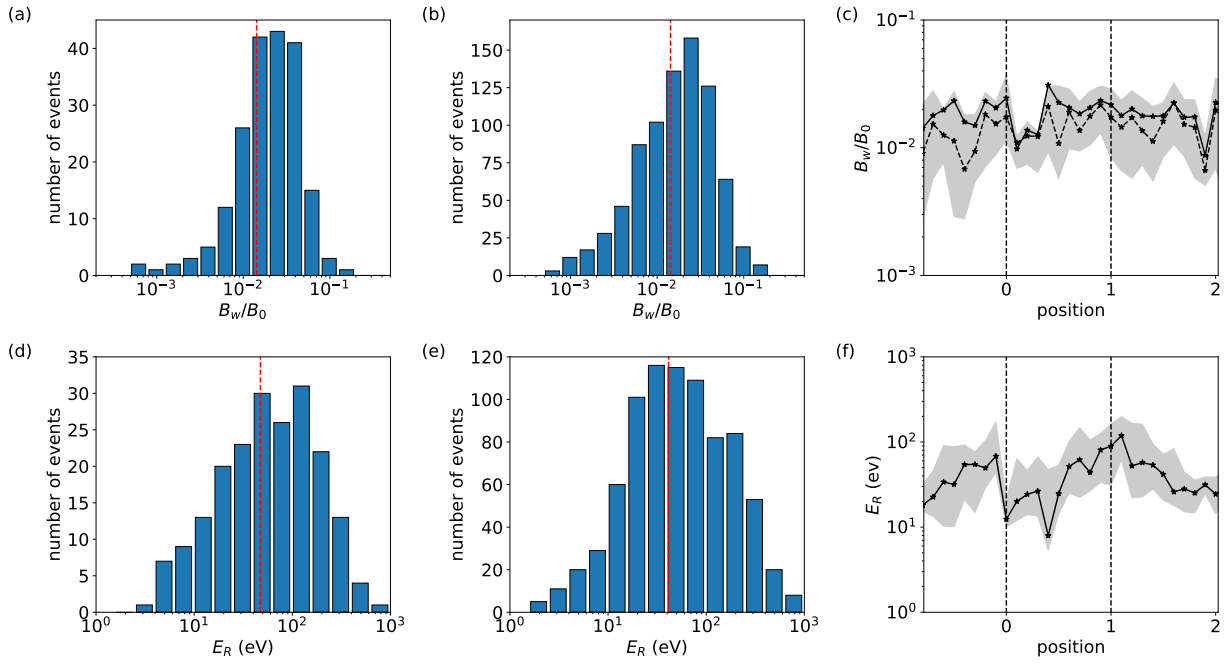

Figure 2.3: Number histograms and spatial distribution of (a-c) maximum wave amplitude, and (g-i) minimum resonance energy for the mean wave frequency. Dashed red lines show the median value.

$$\omega - k_{\parallel} v_{\parallel} = n\Omega_{ce}, \quad n = 0, \pm 1, \pm 2, ... \tag{2.4}$$

where $\omega = 2\pi f$ is the wave angular frequency, $k_{\parallel}$ is the component of the wave vector parallel to the ambient magnetic field and $\Omega_{ce} = 2\pi f_{ce}$ is the angular electron gyrofrequency. Landau resonance occurs at the zeroth order resonance ($n = 0$), which describes when electrons travel along the ambient magnetic field with wave parallel phase speed, allowing for significant and continuous energy exchange in the parallel direction. The case of $n = 1$ describes a first-order cyclotron resonance when the phase velocity of the wave is Doppler-shifted upwards enough to equal $\Omega_{ce}/k_{\parallel}$, which happens for $k_{\parallel} v_{\parallel} < 0$. The electron parallel velocity at first-order cyclotron resonance is $v_r = -(\Omega_{ce} - \omega)/k_{\parallel}$. Higher-order resonance ($|n| > 1$) is less important for field-aligned waves but can become significantly more effective with more oblique waves. For Landau resonance, as the whistler waves were quasi-parallel propagating, the resonance energy was typically below 1 eV. Therefore, we focus on the first-order cyclotron resonance.

Figures 2.3 (d-f) show the distribution of electron parallel resonance energy ($E_R = 1/2 m_e v_r^2$). Whistler waves are mainly resonant with electrons with $10s - 100s$ eV parallel energy. This is the hot solar wind electron halo population, having energies larger than the typical solar wind temperature.

2.3.2 Regimes of Wave-Particle Interaction

Equipped with an understanding of whistler wave characteristics and resonance conditions, we proceed to delve deeper into the resonant interactions between electrons and whistler mode waves. As is known in the radiation belt, there are two regimes of wave-particle interaction, linear and nonlinear regimes, requiring different approaches to study their effects. The desired statistical study of wave properties would ideally distinguish the dominant regime of wave-particle resonant interactions. In this context, we describe the criteria for

distinguishing between these two regimes and examine how whistler waves in the foreshock region are distributed across these interaction domains.

Low amplitude, broad-band waves scatter electrons in the diffusive regime of resonant interactions [Kennel, 1969, Lyons et al., 1972, Veltri and Zimbardo, 1993, Amano et al., 2020], commonly observed in the solar wind [Tong et al., 2019a, Verscharen et al., 2022]. Sufficiently intense, narrow band (coherent) waves may resonate with electrons in the nonlinear regime of resonant interactions [Shklyar and Matsumoto, 2009, Albert et al., 2013, Artemyev et al., 2018a]. Nonlinear resonant interactions include the phase trapping mechanism [O'Neil, 1965, Nunn, 1971], which is quite effective for electron acceleration in Earth's outer radiation belt [Chernikov et al., 1992, Ucer and Shapiro, 2001, Kuramitsu and Krasnoselskikh, 2005]. Once the regime of resonant interactions with electrons can be statistically established for the whistler-mode waves of interest at foreshock transients, their investigation can proceed using the formalism developed (and statistical studies conducted) in a similarly inhomogeneous magnetic field environment, such as Earth's inner magnetosphere [Karpman et al., 1974, Inan and Bell, 1977, Solovev and Shkliar, 1986, Albert, 1993].

The electron resonant interaction with whistler-mode waves is controlled by the wave amplitudes, wave spectral width Δf, and the background field inhomogeneity $\partial B_0/\partial s$. Note that s is the distance along the field, starting from the equator (in our context the equator denotes the location of minimum field magnitude). The same quantity is also used to denote the location of the interaction along the field-line direction. If the wave amplitude is low the waves cannot alter the electron orbit significantly during a single resonant interaction and the interaction remains first-order (linear) and can be described well by zero-order orbit perturbation theory [Kennel and Engelmann, 1966]. If the wave spectral width is too broad relative to the resonance width, nonlinearity from that resonance can also be evaded. These two conditions can be expressed as two criteria for nonlinear interaction. The first assesses the nonlinearity for a pure mode using the inhomogeneity parameter, S, a function of the normalized wave amplitude B_w/B_0 and $\partial B_0/\partial s$. The second criterion for the spectral width

Δf addresses the spectral purity (the monochromatic nature) of the wave.

For highly coherent (approximately monochromatic, or pure mode) waves in an inhomogeneous magnetic field, the nonlinearity criterion for $S \propto (\partial B_0/\partial s)/(B_w/B_0)$ [Omura et al., 2008] is:

$$S = \frac{1}{2}\frac{N^2}{N^2-1}\left(\frac{kv_\perp}{f_{ce}} - \left(3 - \frac{1}{N^2}\right)\frac{v_R}{v_\perp}\right)\cdot\left(\frac{1}{kB_0}\frac{\partial B_0}{\partial s}\right)\cdot\frac{B_0}{B_w}, \tag{2.5}$$

with k being the value of wave vector, $N = kc/\omega$ the wave refractive index, $v_\perp = \sqrt{v^2 - v_R^2}$ the electron transverse velocity, $v_R = 2\pi(f - f_{ce})/k$ the resonant velocity in km/s (k in this equation is in rads/km), and $\partial/\partial s$ the gradient along magnetic field lines. The inhomogeneity of the background magnetic field ($\partial B/\partial s$) is computed using the linear estimation of the gradient method from four-satellite observations (see Chapter 14 of [Paschmann and Schwartz, 2000b]). When $|S| < 1$ the wave is sufficiently strong to locally overcome the mirror force $\sim \partial B_0/\partial s$ and alter the electron trajectory significantly. This is the regime of nonlinear resonant interactions. S depends on the electron energy and pitch angle (linked by the resonance condition). For $\partial B_0/\partial s \neq 0$, S is finite and can be evaluated in two limits: (1) in the local limit, S_{local} evaluated explicitly shows if electrons with a given energy and pitch angle will interact with waves nonlinearly, and (2) in the global limit, S_{global} can be evaluated by projecting the electron pitch angle (α) from the location s of the wave measurements to the location where B_0 reaches its minimum. In the global limit, S_{global} captures how often along their zero-order, adiabatic trajectory ($\sin^2\alpha/B_0 = const$) electrons will interact with the waves nonlinearly.

For each wave event in our database, we obtained the 0.5-second averaged value of the wave properties ($\vec{k}$, $\langle f\rangle$, B_w), electron cyclotron frequency f_{ce}, background field B_0, background inhomogeneity $\partial B/\partial s$, and electron parallel resonant velocity v_R. To compute S, we also need $v_\perp$. Cyclotron resonance happens when the electron parallel velocity is $v_\parallel = v_R$. Therefore, $v_\perp = \sqrt{v^2 - v_R^2} = v\sin\alpha$ is a function of the (total) resonance energy

($E = 1/2 m_e v^2$) and α. (Note that the total energy and α are connected by $\cos\alpha = v_R/v$). We used this to compute S in the local limit, and from it S in the global limit.

We computed S_{local} at different energies using the (local) measurements. Combining all local measurements, we can arrive at the number distribution and the value of S_{local} versus energy and pitch angle in our dataset. Figure 2.4(a) shows the distribution of the number of measurements used for this computation. The black contour shows the number of samples per bin below which lie just 5% of all observations. The region outside this contour denotes the parameter space where the number density of measurements is rather low (interpreted as insignificant) compared to the rest of the parameter space, inside that contour. Figure 2.4(c) shows the fraction of measurements with $|S_{local}| < 1$; it represents the probability distribution for electrons to interact with waves nonlinearly in the local limit. The 5% contour of the number of measurements is transferred here from the counts per bin panel above it. It demarcates the region within which the probability distribution is trustworthy. We see that in the region of $\alpha > 45°$ and $E \in [300, 1000]$ eV the fractions are high: They are $> 30\%$ and can get up to $\sim 60\%$. In this region of (E,α) space where a sufficient number of measurements exist, there is a large enough probability for $|S_{local}|$ to be < 1 (for the observed waves to be sufficiently intense) such that the waves interact with electrons nonlinearly.

The global limit is obtained under the assumption that electrons are bouncing within a local magnetic field trap. In each event, we projected the local electron pitch angle to the location where B_0 reaches its minimum (around the center of the core region), and then obtained S_{global} by mapping S_{local} to a new pitch angle corresponding to that minimum. Such mapping also removes the direct connection between the electron energy and (mapped) pitch-angle through the resonant condition. The number of measurements in energy versus mapped pitch-angle space is shown in Figure 2.4(b) in a format similar to that of Figure 2.4(a), including the contours. The resultant fraction of $|S_{global}| < 1$ is shown in Figure **??**(d), with contours transferred from the panel above it. It shows that $\alpha < 45°$, and > 100 eV electrons will resonant with whistler-mode waves nonlinearly (note measurements outside

of 25% contour are considered not statistically representative).

Overall, Figures 2.4(b,d) demonstrate that in the foreshock transients of our database, quite often the whistler waves are strong enough to cause nonlinear resonant interaction with electrons; the background magnetic field inhomogeneity is too weak to suppress this nonlinear behavior. However, the wave spectral width Δf also influences the resonant interactions. The above considerations assume that the waves are sufficiently monochromatic, i.e., Δf is small enough. The criterion for small Δf can be derived from [Karpman, 1974, Le Queau and Roux, 1987]:

$$\frac{\Delta f}{\langle f \rangle} < \left(\frac{B_w}{B_0} \frac{v f_{pe}}{c f_{ce}} \right)^{1/2} \left(\frac{f/f_{ce}}{1 - f/f_{ce}} \right)^{1/4} \tag{2.6}$$

where v is electron velocity determined by the resonance condition ($v = v_R/\cos\alpha$). If this criterion is not satisfied, the wave spectrum is broadband (random phase approximation is valid) to break nonlinear resonance effects. If the criterion is satisfied, the phase of waves in the wave packet can be coherent and prevent random phase mixing. Similar to the S_{local} treatment, we statistically collected the distribution of RHS/LHS versus energy and pitch angles for each local measurement, where RHS and LHS are the right-hand side and left-hand side terms of Eq.(5). Then we rearranged the data to get the distribution of the wave measurements versus $(|S_{local}|, RHS/LHS)$ (shown in Figure 2.4(e)). The region $|S_{local}| < 1$ and $RHS/LHS > 1$ corresponds to that of nonlinear resonant interactions. The requirement of a narrow wave spectrum halves the number of observed waves resonating with electrons nonlinearly, i.e., $\sim 30\%$ of observed waves have $|S_{local}| < 1$, but only half of these waves have $RHS/LHS > 1$. But even $\sim 15\%$ of waves populating $|S_{local}| < 1$ and $RHS/LHS > 1$ region provides a sufficiently large occurrence rate of nonlinear wave-particle interactions. This occurrence rate is comparable to (or even larger than) that of electron nonlinear resonance with whistler-mode waves in Earth's radiation belts [Zhang et al., 2019] and is much larger than the occurrence rate of electron nonlinear resonance with whistler-mode waves in the solar wind [Tong et al., 2019a].

To identify the possible source of such intense whistler-mode waves interacting with electrons nonlinearly, we examined the electron distribution function (DF) anisotropy by evaluating the transverse-to-parallel phase space density ratio, otherwise referred to as the transverse anisotropy: $DF_\perp/DF_\parallel$. For each local measurement, we computed this quantity at all different energies. We also computed the S_{local} value assuming a fixed, representative value for $\alpha = 50°$ (corresponding to a significant fraction of waves with $|S_{local}| < 1$, based on Figure 2.4(c)). Figure 2.4(f) shows the median of the aforementioned electron transverse anisotropy as a function of normalized energy E/E_R and $|S_{local}|$ value. Near the resonance energy, $E/E_R \in [0.1, 10]$, the electron anisotropy for intense waves (those with $|S_{local}| < 1$) maximizes and reaches ~ 2. Such a high electron anisotropy should result in large whistler-mode wave growth rates and large wave amplitudes. Although the quantity $DF_\perp/DF_\parallel$ cannot uncover an electron heat flux anisotropy (one of the important free energy sources for whistler-mode waves via the heat flux instability [Gary and Feldman, 1977, Tong et al., 2019b]), a large value of this transverse anisotropy can either result in amplification of waves generated by the heat flux instability or it may signify that the anisotropy is itself the primary source for wave generation [Vasko et al., 2020]. Thus, Figure 2.4(f) shows that intense whistler-mode waves amplified (or directly driven) by a large electron transverse anisotropy (up to 2) may resonate with electrons nonlinearly ($|S_{local}| < 1$). However, it is noteworthy that some of the large transverse anisotropies observed at high energies ($E/E_R \sim 10$) may also be generated by electron nonlinear resonant acceleration by whistler-mode waves.

With such a significant population of whistler-mode waves resonating nonlinearly with electrons, we anticipate the electron distributions to exhibit signatures of these interactions. Motivated by the discussion above, we separated the linear and nonlinear wave-particle interactions as follows: (1) linear regime with $|S_{local}| > 1$ or $RHS/LHS < 1$, and (2) nonlinear regime with $|S_{local}| < 1$ and $RHS/LHS > 1$. For each wave measurement, we obtained the concurrently measured electron distribution function $DF(E, \alpha)$. We separated these DF measurements into three categories according to the wave properties: DFs associated

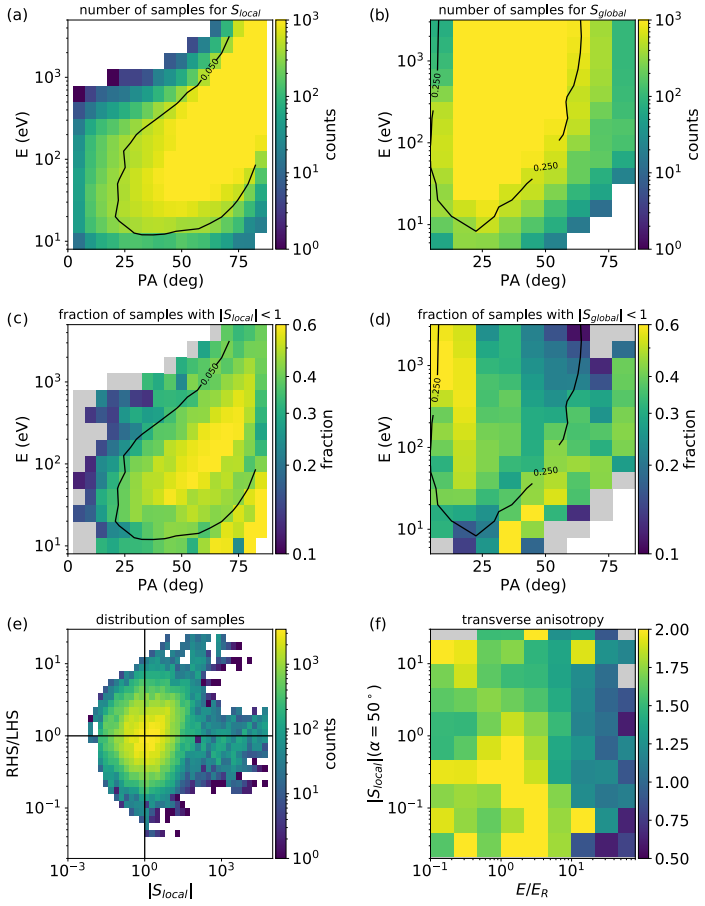

Figure 2.4: Panel (a, b) shows the distribution of samples for S_{local} and $S{+}global$ calculation, respectively. The black contour shows the 95% of total samples. Panel (c) shows the sample fraction of whistler waves resonating with electrons in the nonlinear regime ($|S_{local}| < 1$). Panel (d) repeats panel (c), but for the measurements with pitch-angle adiabatically projected to the minimum of the background magnetic field from the wave observation location (S_{global}). Panel (e) shows the number of wave observations versus ($|S_{local}|, RHS/LHS$), where RHS and LHS refer to the right-hand side and left-hand side of Eq (5), respectively. $|S_{local}| < 1$ and $RHS/LHS > 1$ define the region of nonlinear wave-particle interactions (see text for details). Panel (f) shows the distribution of electron flux anisotropy versus $|S_{local}|$ and energy. The energy is normalized to the resonance energy for the observed waves.

with linear (DF_L) wave-particle interactions, DFs associated with nonlinear (DF_{NL}) interactions, and no-wave DFs (DF_{NW}), those without significant whistler-mode waves observed. All electron distribution functions were normalized to the local plasma density to suppress any effects related to the strong density variations across the foreshock transients. In each transient event, we first calculated the median values of DF_{NL}, DF_L, and DF_{NW}, and their ratios (DF_L/DF_{NW} and DF_{NL}/DF_{NW}). Then we calculated the median values of these ratios. The results are shown in Figure 2.5(a,b); they are plotted against energy (normalized to E_R) and pitch angle. There is a clear phase space density increase around and above the resonance energy and $\alpha \sim 90°$ for DF_L. This increase may be due to a combination of an initial electron anisotropy driving whistler-mode wave generation and electron acceleration by waves. A similar increase in phase space density is also evident for DF_{NL}, except it is much more localized in energy (around E_R) and over a wider α range. If the strong DF_{NL} peak around $\alpha \sim 90°$ is due to the strong initial anisotropy needed for intense wave generation, the DF_{NL} increase at small pitch-angles ($\alpha < 45°$ and $\alpha > 135°$) is most likely due to the effective electron mixing by nonlinear resonance with waves [Vainchtein et al., 2018]. A weak decrease of DF_L/DF_{NW} and DF_{NL}/DF_{NW} at energies well below the resonance energy is unlikely to be related to wave-particle resonant interactions but could be due to preferential wave generation within hot plasma regions where the cold electron density is reduced. The black lines in Figure 2.5(a,b) show the contours of DF_{NW}. Results with $DF_{NW} < 10^{-5}$ are not statistically significant because such a small phase space density may lead to large errors.

To further investigate the difference between the distributions of phase space density associated with weak and intense waves, we plot the probability distributions of $DF_L/DF_{NW} > n^*$ (for weak waves) and $DF_{NL}/DF_{NW} > n^*$ (for intense waves) overall pitch angles, where n^* stands for the value of the ratio. Figures 2.5(c,d) show the percentage of events with $DF_L/DF_{NW} > n^*$ and $DF_{NL}/DF_{NW} > n^*$ at different energies, respectively. There is a clear difference between weak and intense waves. For $DF_L/DF_{NW} > n^*$ around the resonance energy ($E/E_R \approx 1$) the probability distribution is reduced significantly for $n^* > 2$,

i.e. there is nearly negligible probability of observing a phase space density increase by a factor of > 2 in association with weak waves. Conversely, for $DF_{NL}/DF_{NW} > n^*$ around the resonance energy the probability distribution remains large even for $n^* \sim 3$, i.e., there is a significant probability of observing intense waves in association with the resonant phase space density increase by a factor of ~ 3. Moreover, Figure 2.5(d) shows that the probability distribution has a local maximum around the resonance energy. These results are consistent with our assertion that nonlinear resonant interactions contribute significantly to electron acceleration.

2.3.3 Quasi-linear Theory for Wave-Particle Interactions

Although nonlinear interactions can effectively alter electron trajectories and may contribute significantly to electron acceleration, the majority of observed whistler waves interact with electrons in the linear regime. In this subsection, we elucidate the theory of quasi-linear interactions. Detailed discussions on nonlinear interactions is provided in Chapter 3 and Chapter 4.

Resonant interactions with hundreds of eV electrons can lead to diffusion in both the electron's pitch-angle and energy, amplifying or damping waves in the process. Such diffusion smooths the gradients of the electron distribution function along so-called "diffusion curves" [Lyons and Williams, 1984]:

$$(v_{\parallel} - \omega/k_{\parallel})^2 + v_{\perp}^2 = const \tag{2.7}$$

The diffusion curves define a diffusion surface by which the phase space density gradient determines the preferential direction of diffusion. To determine the net energy and pitch-angle diffusion direction, one must analyze the particle diffusion direction to the constant energy curves in the velocity space. Figure 2.6 shows an example of the comparison between the diffusion curves of the whistler waves and the electron distribution contours. Figure

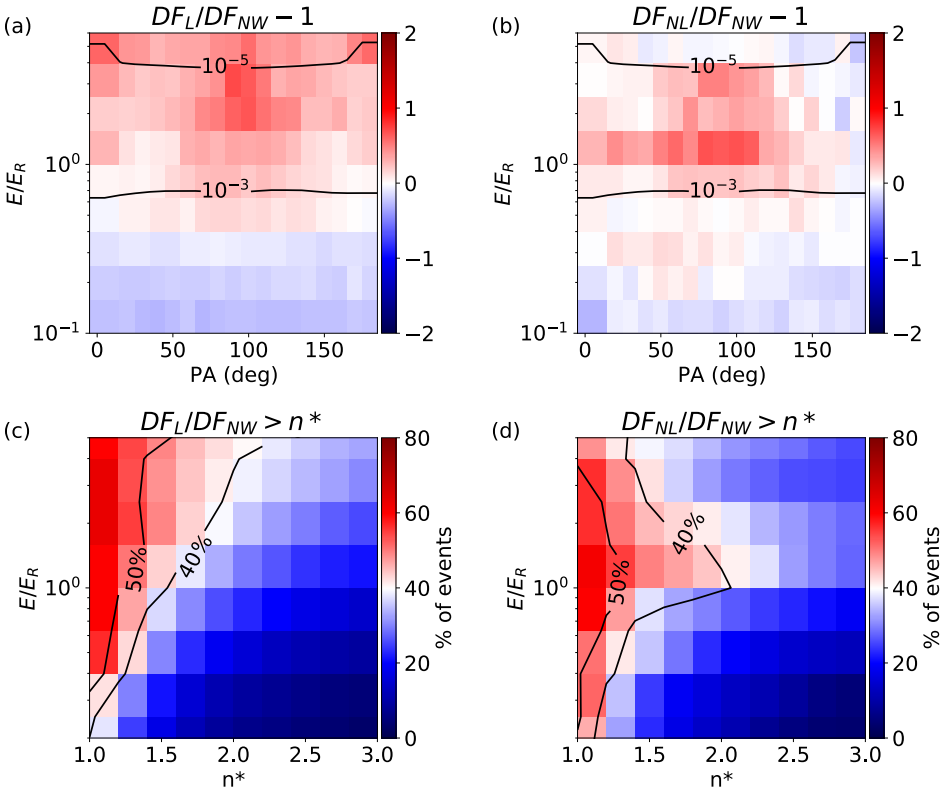

Figure 2.5: Electron distribution functions (DFs) collected during times when waves were observed, normalized to those collected in the absence of waves. Panels (a) and (b) show electron DFs associated with weak (a) and intense (b) wave observations normalized to the background (measured in the absence of waves; subindex NW) electron spectra. Panels (c) and (d) show the probability distributions of $DF_L/DF_{NW} > n^*$ and $DF_L/DF_{NW} > n^*$, respectively. Weak waves correspond to $|S_{local}| > 1$ or $RHS/LHS < 1$ and are marked by subindex L, whereas intense waves correspond to $|S_{local}| < 1$ and $RHS/LHS > 1$ and are marked by subindex NL.

2.6 (a-g) shows a foreshock transient observation from THEMIS-C and the shaded region indicates the time when wave-burst data are available. Figure 2.6 (h) shows the electron velocity distribution in the BV plane (a 2D slice) from 16:26:38 to 16:26:41 UT. During this period, the observed whistler frequency is from $\sim$ 30 to 170 Hz, and the electron minimum resonant energy is around 26–328 eV. For each THEMIS energy channel in this energy range, we calculated a diffusion curve (red curve). To quantify how well they match, we calculated the normalized phase space density (F) gradients along the diffusion curves. The normalized F gradient is calculated by multiplying dF/Fdv by the typical resonance velocity. To facilitate comparison along the diffusion curves, we averaged the F gradients over pitch angles to suppress fluctuations due to measurement uncertainties. In this event, the normalized gradients are $\sim$ 0.04 and the typical resonance velocity is 870 km/s, indicating that dF/F changes by 4% per 870 km/s. This confirms that the diffusion curves match the distribution contours and suggests that the electrons are scattered by the whistler waves.

To further confirm this, we also need to estimate the pitch-angle diffusion coefficients of the whistler waves at various resonant energies. A general expression for the diffusion of particles by wave-particle interactions using quasi-linear theory was derived by [Kennel and Engelmann, 1966, Lyons and Williams, 1984]. The quasi-linear diffusion equation can be written as [Lyons and Williams, 1984]:

$$\frac{\partial f_0}{\partial t} = \frac{1}{p \sin\alpha} \frac{\partial}{\partial \alpha} \sin\alpha \left(D_{\alpha\alpha} \frac{1}{p} \frac{\partial f_0}{\partial \alpha} + D_{\alpha p} \frac{\partial f_0}{\partial p} \right) + \frac{1}{p^2} \frac{\partial}{\partial p} p^2 \left(D_{p\alpha} \frac{1}{p} \frac{\partial f_0}{\partial \alpha} + D_{pp} \frac{\partial f_0}{\partial p} \right) \tag{2.8}$$

where α is the electron pitch-angle, p is momentum, and f_0 is the zero-order spatially uniform electron distribution function. $D_{\alpha\alpha}$, $D_{\alpha p}$, and D_{pp} are the local diffusion coefficients that describe the electron energy/pitch-angle changes per unit time. The expressions for the pitch-angle diffusion coefficients, $D_{\alpha\alpha}$, have been derived by [Lyons, 1974]:

$$D_{\alpha\alpha} = \sum_{n=n_l}^{n=n_h} \int_{X_{min}}^{X_{max}} X dX D_{\alpha\alpha}^{nX} \tag{2.9}$$

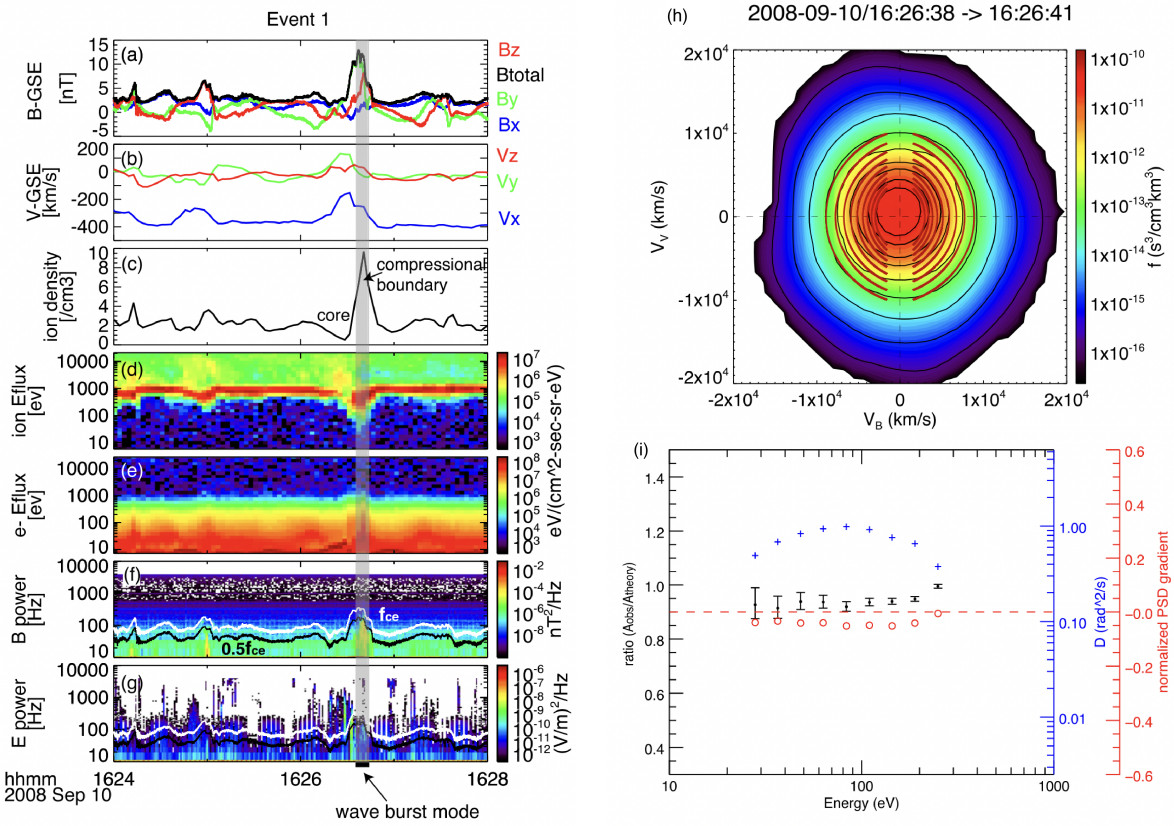

Figure 2.6: THC observations of a foreshock transient (left) and an enlarged plot of the compressional boundary during the wave burst mode (right). Left panel: (a) magnetic components in GSE coordinates (X, Y, Z, and total in blue, green, red, black, respectively); (b) ion bulk velocity in GSE coordinates (X, Y, and Z in blue, green, and red, respectively); (c) total ion density; (d) electron ESA energy spectra; (e) ion ESA energy spectra; (f) power spectra of magnetic field; (g) power spectra of electric field. (h) Electron velocity distribution in the BV plane during the wave burst mode and whistler diffusion curves (red lines) at various resonant energies; (i) normalized F gradients (red circles), anisotropy ratios of observations to theory (black dots), and pitch angle diffusion coefficients of whistler waves (blue plus) at various resonant energies.

$$D_{\alpha\alpha}^{nX} = \sum_i \frac{B^2(\omega_i) g(X) e^2 \omega_i^2}{4\pi(1+X^2)N(\omega)} \left(\frac{-n\Omega_{ce}/\omega - \sin^2\alpha}{\cos\alpha} \right)^2 \left(\frac{|\Phi_{n,k}|^2}{|v_\parallel - \partial\omega/\partial k_\parallel|} \right)_{k_{\parallel,i}} \tag{2.10}$$

where $g(X)$ is the distribution of wave power with wave normal angle ψ ($X = \tan\psi$), $B^2(\omega)$ is the distribution of wave power with frequency, $N(\omega)$ is a normalization factor, and $|\Phi_{n,k}|^2$ depends on the wave refractive index for the particular wave mode and is given by [Glauert and Horne, 2005]. The blue crosses in Figure 2.6 (i) represent the pitch-angle diffusion coefficients estimated through Equation 2.10 using the approximation of quasi-parallel propagating and only including the first-order cyclotron resonance effect. They are around 1.1–1.2 rad^2/s. Because the thickness of the compressional boundary is $\sim 4,000$ km, electrons with energies about 300eV have a speed along the boundary normal as ~ 600 km/s. Thus, electrons need at least a few seconds to transit the compressional boundary, a time sufficient for the diffusion coefficients calculated above to produce significant pitch-angle scattering. This indicates that the observed whistler waves are indeed strong enough to cause electron distributions to follow diffusion surfaces within this transit time.

2.4 Summary

We showed a case study and a statistic study of whistler wave properties in foreshock transients, and we also investigated the regimes of wave-particle interactions and the effects of nonlinear interactions on electron distributions. Specifically, we showed that:

1. Whistler waves exist in 85% of the foreshock transients examined. These waves are most often seen around the edge of the core or the compressional boundary regions of foreshock transients.

2. Whistler waves can effectively scatter electrons. We use a case study to show that the diffusion coefficient can reach 1.1–1.2 rad^2/s, which is high enough to scatter electrons within the transit time scale.

3. The whistler waves in foreshock transients have frequencies around $0.2f_{ce}$, regardless of the abrupt change of the background magnetic field at their location. This indicates that they are generated locally, i.e., they do not propagate to the satellite from a distinctly different location in the transient or its vicinity. On average, the whistler waves are quasi-parallel. However, the waves in the core region tend to be more oblique than the waves in the compressional boundary.

4. Intense whistler waves are frequently observed. Their median amplitude is around $0.01B_0$ ($\sim 10s - 100s$ pT). The resonance energy for electrons is around $10s - 100s$ eV, and 15% of the observed whistler waves are sufficiently intense and narrow-band to resonate with electrons nonlinearly.

5. Events with potential nonlinear wave-particle interactions show a clear increase in phase space density around the resonance energy. This increase is larger than that for observations associated with low-intensity waves. This suggests that nonlinear resonant interactions can contribute significantly to electron acceleration.

Our statistical results on the whistler-mode wave intensity demonstrate that a significant portion of the observed waves interact with electrons nonlinearly. The nonlinear interactions can play an important role in electron acceleration processes in the following way:

First, nonlinear interactions have diffusion rates that are different from (often faster than) those found in classical, linear theory. We have shown that intense waves can significantly modify electron distributions, which indicates that they can alter electron trajectories. This invalidates the approximation of unperturbed trajectories for classical scaling of electron pitch-angle diffusion rates $D \propto \langle B_w \rangle^2$ [Kennel and Engelmann, 1966], and therefore, classical pitch-angle diffusion theory does not apply in such cases. If the waves propagate in short wave packets (containing only a few wave periods each; see, e.g., such wave packets in the bow shock in [Hull et al., 2012, Oka et al., 2017, Oka et al., 2019]), then the main nonlinear effect will be the change of the diffusion rate scaling, $D \propto \langle B_w \rangle^{1/2}$ [Artemyev et al., 2021b]. In

that case, a simple extrapolation of quasi-linear theory scaling, $D \propto \langle B_w \rangle^2$, to high-intensity waves would significantly overestimate the actual diffusion rate. The diffusion rate is an important element of the stochastic shock drift acceleration model [Amano et al., 2020], and therefore the change in the scaling of D may modify the efficiency of the resultant electron acceleration in this model.

Second, intense waves propagating in long wave packets (each containing tens of wave periods) may result in nonlinear resonant acceleration of electrons in an inhomogeneous magnetic field via phase trapping [Shklyar and Matsumoto, 2009, Albert et al., 2013]. To be effective, this acceleration mechanism should be combined with electron periodic motions in magnetic field traps, i.e., electrons should experience multiple resonant interactions. The magnetic field configuration of foreshock transients allows for such a trapping motion [Liu et al., 2019]. However, such trapping can be provided by ultra-low-frequency compressional magnetic field fluctuations [Oka et al., 2019, Lichko and Egedal, 2020] and by the transient-bow shock magnetic field configuration [Liu et al., 2017b, Turner et al., 2018].

Therefore, foreshock transients embedding intense whistler-mode waves (resonating with electrons nonlinearly) may serve as an effective electron accelerator if the interplanetary magnetic field can trap electrons. Further theoretical analysis of nonlinear wave-particle resonances and observational analysis of energetic electron bursts and whistler waves associated with foreshock transients may reveal the efficiency of such nonlinear resonant acceleration. In Chapter 3, we further show the effect of nonlinear wave-particle resonances through test-particle simulations.

CHAPTER 3

Electron Acceleration via Nonlinear Resonant Interactions

3.1 Introduction

Theoretical models suggest that nonlinear resonant interactions can effectively accelerate electrons (especially around the bow shock where the background magnetic field has large gradients [Artemyev et al., 2022a] or large-scale electrostatic fields exist [Kuramitsu and Krasnoselskikh, 2005]), and we have shown in Chapter 2 that whistler-mode waves in the foreshock region can be sufficiently intense to resonate with electrons nonlinearly. This chapter aims to show observational evidence of electron acceleration by intense whistler-mode waves at the strong magnetic field gradients around Earth's bow shock. We demonstrate that nonlinear wave-particle interactions can be sufficiently important to shape the distributions of suprathermal electrons (i.e., those at energies around $50 - 500$eV, much larger than the solar wind electron with temperature of $\sim$ 10eV; see [Wilson et al., 2018]). Mechanisms of whistler wave generation due to electron compressional heating and further formation of such suprathermal electron populations are universal, and thus the study of whistler waves at Earth's bow shock is also applicable to astrophysical shocks [Amano et al., 2022].

To provide multiple resonant interactions with coherent (narrow-band) whistler-mode waves, electrons should bounce within a magnetic field bottle (most of the results for nonlinear electron accelerations by whistler-mode waves were obtained for such magnetically trapped electron motion) [Shklyar and Matsumoto, 2009, Albert et al., 2013, Artemyev

et al., 2018a]. Around the bow shock, such a magnetic bottle can be provided by large-amplitude compressional magnetic field fluctuations [Hull et al., 2012, Lichko and Egedal, 2020] or by foreshock transients [Lin, 2002, Omidi et al., 2009, Turner et al., 2013, Liu et al., 2016]. Foreshock transients, such as foreshock bubbles and hot flow anomalies, have a hot core associated with strong plasma deflections and are surrounded by compressional boundaries with enhanced magnetic field strength and density. Figure 3.1(a) shows the structure of a magnetic bottle formed between a foreshock transient and the bow shock. Particles can be trapped within the region of the transient's core bouncing between the strong fields at the bow shock on the one side and the transient's boundary on the other side [Liu et al., 2017b, Liu et al., 2018]. Such a magnetic bottle allows electrons to interact with whistler waves multiple times. In such an environment, intense whistler waves can provide effective electron acceleration via nonlinear resonant interactions, including the effect of phase trapping. Phase trapping can provide a large energy gain for only a few interactions [Artemyev et al., 2018b], which is quite important for dynamical foreshock transients where electrons may quickly escape from the magnetic bottle (the acceleration region). To study this process, we searched for and identified 16 foreshock transient events with strong whistler waves and a magnetic topology consistent with a magnetic bottle. We also present an example from one of these events, epitomizing the signatures common to all events. We further demonstrate the generality of the conclusions drawn from this event with a statistical analysis of all events and compare model results of wave-particle resonant interactions with observed electron pitch-angle distributions.

3.2 Observations

The dataset used in this chapter is from the Magnetospheric Multiscale (MMS) mission [Burch et al., 2016]. We used magnetic field data from the fluxgate magnetometer (FGM) [Russell et al., 2016] and the search coil magnetometer (SCM) [Le Contel et al., 2016] at a

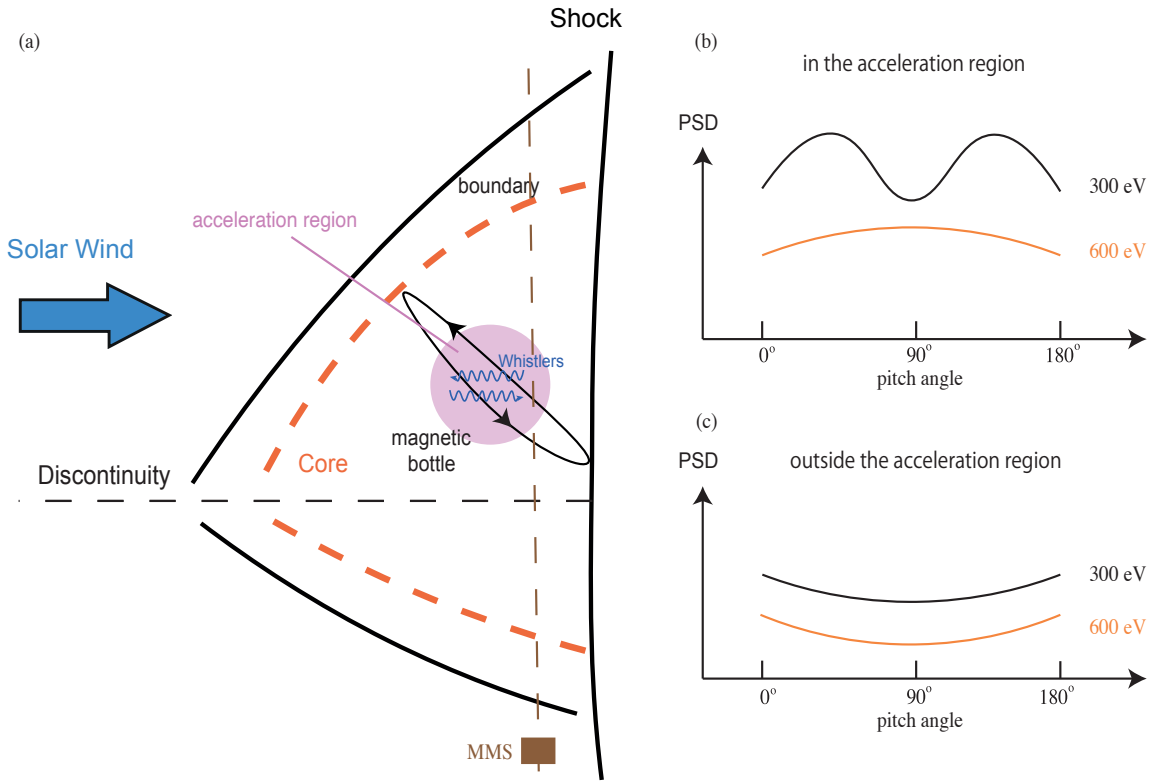

Figure 3.1: (a) The structure of a magnetic bottle inside a foreshock transient: electrons are bouncing between the compressional boundary and bow shock, and resonate with whistler-mode waves. The nonlinear resonant interaction should result in electron acceleration, and we would expect the formation of local maxima of electron fluxes (or phase space density, PSD) at intermediate pitch-angles [Gan et al., 2020b, Peng et al., 2022]. Thus, the acceleration should result in a transition between field-aligned electron phase space density distributions (c) to butterfly distributions (b).

rate of 128 S/s and 8192 S/s, respectively, in burst mode. We used plasma data from the fast plasma investigation (FPI) [Pollock et al., 2016] instrument also in burst mode at a time resolution of 30ms for electrons.

Figure 3.2 shows the observation of a foreshock transient characterized by compressional boundaries with increasing magnetic field strength and density, and a core region with hot electrons and low magnetic field strength. Panel (a) shows three components of the magnetic field in GSE coordinate. The leading and trailing compression boundaries are around 20:26:45 UT and 20:27:05 UT, respectively (see Panel (a) and the vertical lines). Panels (g) and (h) show quasi-parallel whistler waves within the transient.

Figure 3.3 shows the magnetic field (in GSE and flow-aligned coordinates) and electron pitch-angle distributions within the foreshock transient. Note that this transient structure is transported by the solar wind and remains quasi-static during the crossing time (typical time-scales of foreshock transient dynamics are longer than a minute) [Lin, 2002, Gedalin, 2015, An et al., 2020]. Before 20:26:55 UT, the solar wind flow v is mostly along x (see Panel (e) in Figure 3.2) and the magnetic field is almost along the plasma flow direction ($B \parallel v$, see Figure 3.3(b)). Around 20:26:55 UT, the magnitude of $B_{\parallel}$ drops to zero, which means that the spacecraft crossed the magnetic field almost transversely to the magnetic field direction (see Panel (b)). Therefore, around 20:26:55 UT, the spacecraft crossed a discontinuity separating different magnetic field directions. This discontinuity is an essential part of the foreshock transient [Lin, 1997, Omidi et al., 2009, Vu et al., 2022b, Lin et al., 2022] and can be best seen in electron pitch-angle distributions showing very different solar wind electron populations ($10 - 50$eV) before and after 20:26:55 UT (see Panel (d)).

To confirm this result, we consider electron populations across discontinuities found in each foreshock transient of our statistics. We collected 32 foreshock transient events which have clear signatures of the discontinuity in the core region, and analyzed the change of electron fluxes crossed the discontinuity where $B_{\parallel}$ reaches zero (indicated by the vertical line). Figure 3.3 demonstrates that such a strong gradient in the electron distribution is

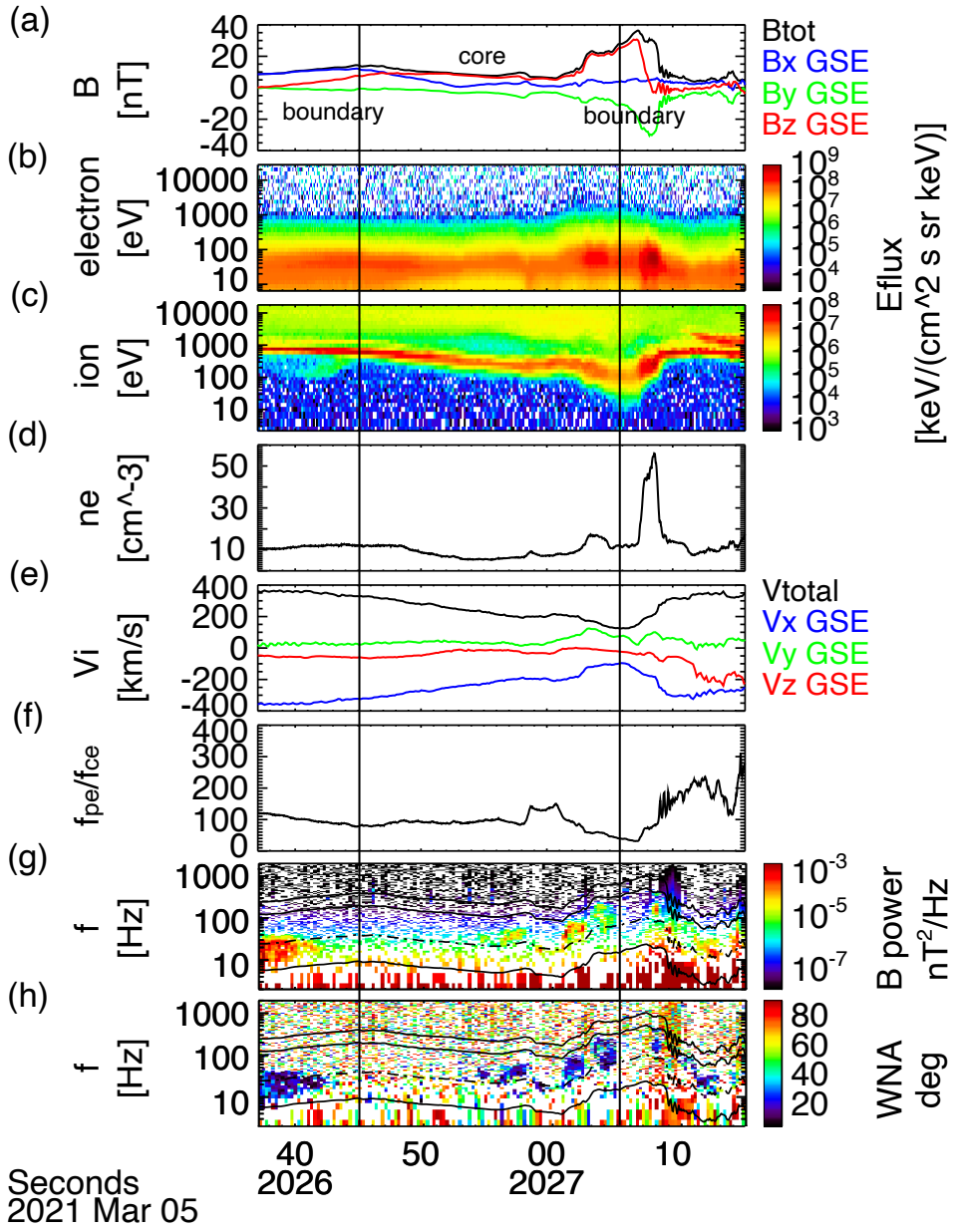

Figure 3.2: (a) Magnetic field, (b,c) Energy flux of electrons and ions, (d) Electron density, (e) Plasma velocity, (f) f_{pe}/f_{ce}, (g) Magnetic field power spectral density, and (h) Wave normal angle. Black lines in Panels (g) and (h) from top to bottom are f_{ce}, $0.5f_{ce}$,$0.1f_{ce}$, and f_{lh}, respectively.

typical for solar wind discontinuities (see also [Artemyev et al., 2019a]).

Thus, we may assume that the electron population is trapped between this discontinuity and the magnetic field maximum at the trailing edge (interval 20:26:55–20:27:08 UT, the orange shaded region in Figure 3.3). Around this B-maximum (20:27:02–20:27:08 UT) there is a strong flux increase of hot electrons (see Panels (d-g)), which is likely due to electron adiabatic heating caused by magnetic field compression. Sub-interval 20:26:55–20:27:00 UT is within the transient core, where the electron population is not affected by magnetic field compression. This sub-interval is characterized by intense whistler-mode wave activity (see Panel (c)) and butterfly pitch-angle distribution of hot electrons ($50 - 250$eV). The latter exhibits peak flux at $\sim 50°$ and $\sim 140°$ pitch-angles. It is unlikely that these peaks are caused by adiabatic electron heating, because betatron acceleration would increase $\sim 90°$ fluxes, whereas Fermi acceleration would increase field-aligned fluxes. Similar butterfly distributions (with much higher electron energies) corresponding to resonance with whistler-mode waves have been observed in Earth's radiation belts [Fennell et al., 2015, Peng et al., 2022]. There, test particle simulations have demonstrated that nonlinear resonant interactions with intense whistler-mode waves may result in such distributions [Gan et al., 2020b, Saito and Miyoshi, 2022]. By analogy, in this chapter we examine the role of a similar mechanism in producing the butterfly distributions shown in Figure 3.3.

3.3 Test Particle Simulations

3.3.1 Wave-Particle Interaction Model

To model electron (mass m_e, charge $-e$) resonant interactions with whistler-mode waves, we adopt the gyro-averaged Hamiltonian system [Artemyev et al., 2022a]:

$$\mathcal{H} = \frac{p_{\parallel}^2}{2m_e} + \mu\Omega\left(s\right) + \sqrt{\frac{2\mu\Omega\left(s\right)}{m_e c^2}}\frac{eB_w}{k}\cos\left(\phi + \psi\right) \tag{3.1}$$

where $(s, p_{\parallel})$ and (ψ, μ) are pairs of conjugate variables: $s, p_{\parallel}$ are the field-aligned co-

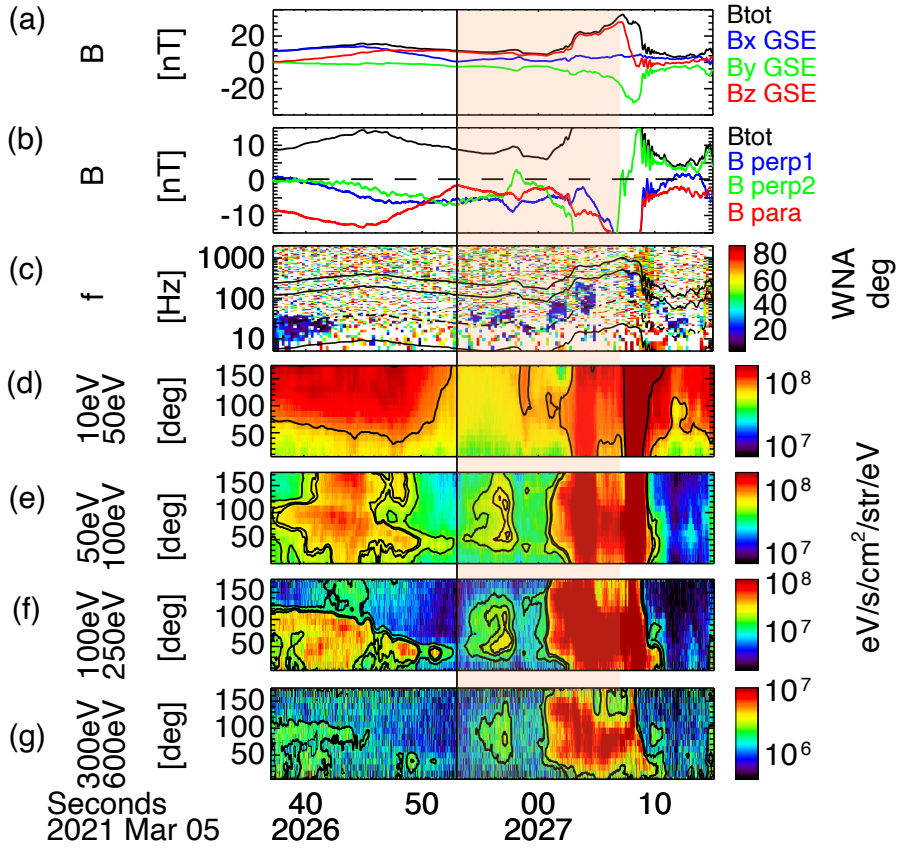

Figure 3.3: (a) Magnetic field in GSE coordinates, (b) Magnetic field in plasma velocity aligned coordinates, (c) Wave normal angle of whistler waves; (d-g) Electron pitch angle distribution at different energies. Black lines show the contour of fluxes.

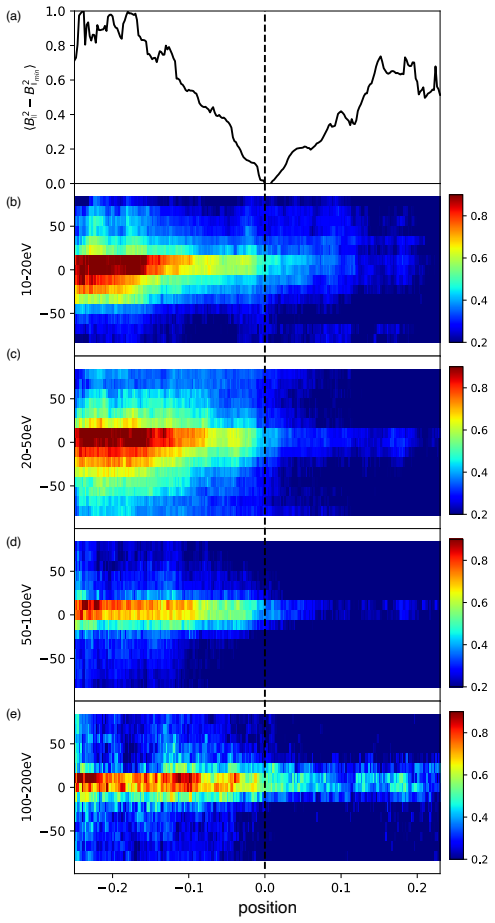

Figure 3.4: Electron fluxes change across the discontinuity within foreshock transients. Panel (a) shows an averaged profile of $B_{\parallel}^2 - B_{\parallel,\min}^2$ (normalized to [0,1]). This profile traces the location of the discontinuity. Panels (b-e) show the epoch analysis of pitch angle distributions: time is normalized to $[-0.25, 0]$ for the side with larger electron fluxes and $[0, 25]$ for the side with smaller electron fluxes, pitch-angle shifted to have $\alpha = 0$ at maximum fluxes for the energy in the range $10 - 200$eV. This figure shows that discontinuity embedded within foreshock transients separates two electron populations with different pitch-angle distributions, and there is no electron transport across the discontinuity: no mixture of two populations that otherwise would result in similar pitch-angle distributions on both sides.

ordinate and momentum, ψ is the electron gyrophase, and μ is the normalized magnetic moment. The background magnetic field configuration of an electron magnetic bottle is assumed to be: $\Omega(s) = \Omega_0 \cdot (1 + (9/2) \cdot f(s/R))$, where $\Omega(s) > 0$ is electron gyrofrequency at position s, $\Omega_{pe,0}$ and Ω_0 are the electron plasma frequency and electron gyrofrequency in the foreshock transient core (the position with minimum magnetic field strength), and $f(s/R) = 2 + \tanh(s/R - 3) - \tanh(s/R + 3)$ with $R \sim 500km \sim 2.5 \cdot 10^3 c/\Omega_{pe,0}$. The spatial scale of the foreshock transient $\sim 10 \cdot R$ is about 5000 km. This magnetic bottle allows electrons to bounce between two magnetic field peaks with $\max \Omega(s)/\Omega_0 = 10$, in agreement with the observed B variation between $\sim$ 4 and $\sim$ 40nT (see Figure 3.2(a)). The corresponding loss-cone angle $\alpha_{LC} = \arcsin(1/\sqrt{10}) \approx 20°$. Particles with pitch-angles below α_{LC} should escape from the bottle and cannot further resonate with waves. Wave phase ϕ is determined by the wave frequency ($\omega = -\partial\phi/\partial t$) and the wavenumber ($k(s) = \partial\phi/\partial s$), where the wavenumber is from the cold plasma dispersion relation $k(s)c = \Omega_{pe}(s) \cdot (\Omega(s)/\omega - 1)^{-1/2}$ [Stix, 1962]. Based on plasma density measurement, we set the constant $\Omega_{pe}(s)/\Omega(s) \approx 100$ (see Figure 3.1(f), subinterval 20:26:55–20:27:00 UT). This parameter essentially controls the energy range for wave-particle resonant interactions, as minimum resonance energy (for field-aligned electrons with $\mu \sim 0$) for the first cyclotron resonance is $\sim m_e c^2 (\Omega_0/kc)^2/2 \sim 250keV \cdot (\Omega_0/\Omega_{pe})^2$. Large $(\Omega_0/\Omega_{pe,0}) \sim 100$ sets the minimum resonance energy to 25eV, whereas electrons with energy above minimum resonance energy can resonate with waves at larger $|s|$ and the resonance energy range is determined by the background magnetic field configuration (i.e., the range of s where bouncing electrons can resonate with waves).

To determine the regime of wave-particle resonant interaction, we shall analyze the properties of observed intense wave packets in our event. Figure 3.5 shows the observation of the whistler-mode wave during 20:26:54–20:27:00 UT, when 50-250eV electrons exhibit butterfly distributions. The whistler-mode waves are quasi-parallel propagating and circularly polarized with a nearly constant frequency around $0.2 f_{ce}$, where $f_{ce} = \Omega/2\pi$ (see Figure 3.5 (a-c)).

Therefore, we may consider a monochromatic wave approximation for the wave-particle resonant interaction model [Demekhov et al., 2006, Omura et al., 2015, Hiraga and Omura, 2020, Artemyev et al., 2023]. Figure 3.5(d) shows the wave packets of the whistler-mode waves: waves are quite intense with the maximum amplitude reaching $0.5-1\%$ of the background magnetic field. Typical wave packets contain $\ell \sim 20$ wave periods. Such wave packets, exhibiting amplitude modulation can be modeled with $B_w \to B_w \cdot \exp\left(-5\cos^2(\phi/2\pi\ell)\right)$ [Zhang et al., 2020]. The nonlinearity of electron resonant interactions with whistler-mode waves can be described by the inhomogeneity parameter, S, which compares two forces acting on electrons: the Lorentz force of the waves and a generalized mirror force due to the background field inhomogeneity (see [Omura et al., 2008] for the details of S parameter): $S \propto (\partial B_0/\partial s)/(B_w/B_0)$, where $\partial B_0/\partial s$ is the background magnetic field gradient obtained using the linear estimation of the gradient method from four-satellite observations [Shi et al., 2023b]. If $|S| < 1$ the wave is strong enough to locally overcome the mirror force $\sim \partial B_0/\partial s$ and alter the electron trajectory significantly, i.e. this is a nonlinear regime of wave-particle interactions. We calculated the S parameter for each wave packet during 20:26:54–20:27:00 UT and the results are shown in Figure 3.5 (e,f). The majority of wave packets can resonate nonlinearly with $200eV$ electrons (Figure 3.5(e)). Figure 3.5(f) shows the fraction of measurements with $|S| < 1$ which represents the probability distribution for electrons to interact with waves nonlinearly. Note that these estimates are provided for local wave and electron characteristics, whereas electron bouncing within the B_0 minimum should result in the widening of the energy/pitch-angle range of resonant (as particularly nonlinear) interactions with waves [Hsieh and Omura, 2017, Vainchtein et al., 2018]. Our analysis indicates that nonlinear effects should be important in this event.

3.3.2 Simulation Results

We numerically integrate the Hamiltonian equations of motion (3.1) for 10^6 electrons initially uniformly distributed in pitch-angle $\in [\alpha_{LC}, 180^\circ - \alpha_{LC}]$ and energy $\in [10, 10^3]$ eV. The total

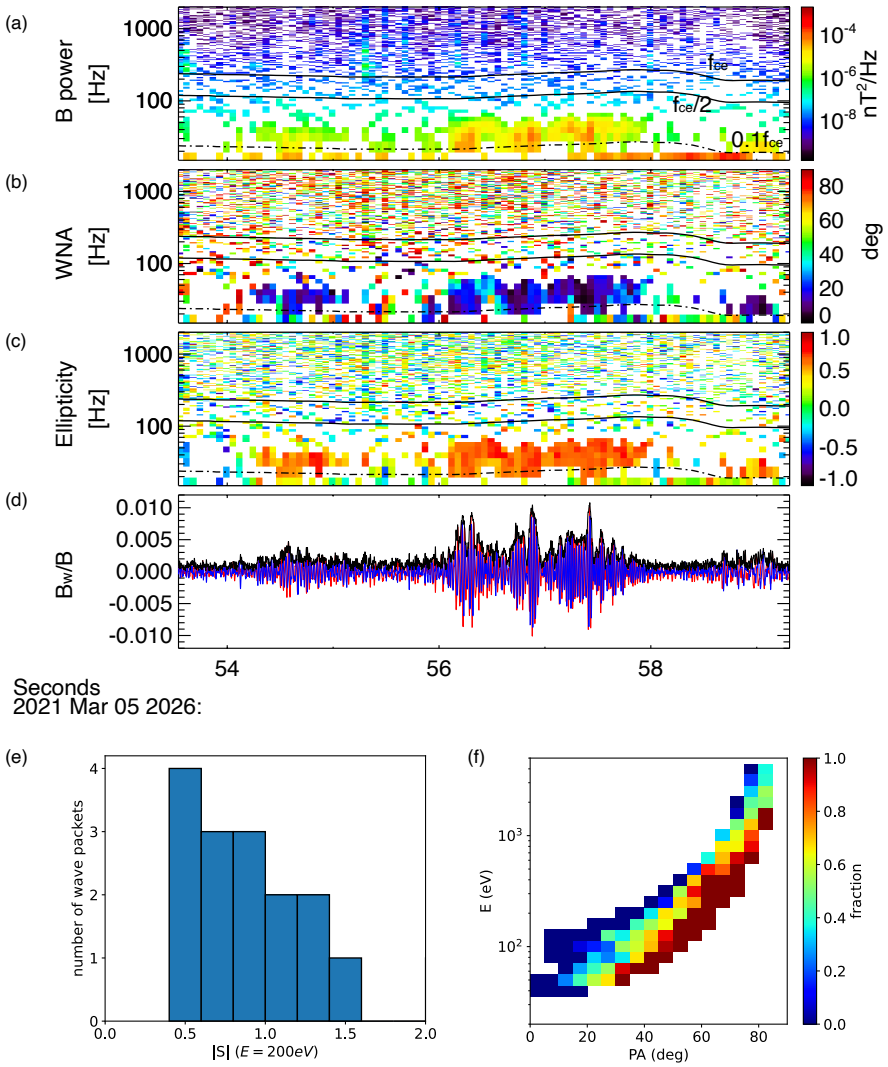

Figure 3.5: Whistler-mode wave power spectrum (a), wave normal angle (b), ellipticity (c), and wave packets in field-aligned coordinates with the wave field normalized to the background field (d). S parameter [Omura et al., 2008] distribution for $200eV$ electrons (e) and probability distribution of $|S| < 1$ (f).

integration time is ~ 15 seconds of real-time (bounce period is ~ 1.5s for $\sim 100eV$ electrons and there are two resonant interactions per bounce period). For each bounce period of each electron, we launch a new wave with a random frequency and random wave amplitude having uniform distribution within $[0.1, 0.4]f_{ce}$ and $[0.0025, 0.01]$ of the background magnetic field. Figure 3.6(top Panels) shows three examples of electron trajectories for different energies and initial pitch-angles: 100eV electrons experience regular phase trappings with energy jumps $\geq$ 5eV, whereas most often electrons are scattered with a random change of energy (diffusive scattering without nonlinear resonant effects) or with energy decrease due to the phase bunching. These three effects (nonlinear phase trapping and phase bunching, and diffusive scattering) are comparable in magnitude for electrons with an initial energy of 300eV, and therefore such electrons mostly diffuse in energy space. However, this diffusion is quite strong, providing energy variations up to $\pm$30eV for 5 seconds of real time.

As we do not know the initial electron distribution function, we show results for three different initial distributions: a uniform pitch-angle distribution $g(E)$; a pitch-angle distribution with a smaller number of particles around the loss-cone $g(E)\sin\alpha$; and a field-aligned pitch-angle distribution $g(E)\cos\alpha$. Function $g(E)$ describes the energy spectrum corresponding to the unperturbed electron population observed around the discontinuity. Figure 3.6(bottom panels) shows that regardless of the initial distribution, after ~ 20 resonant interactions electrons exhibit clear butterfly distributions with a peak around 50° for $[50, 250]$ eV energy range (all distributions are normalized to the integral $\int_{\alpha_{LC}}^{90^\circ} g(E)\sin\alpha d\alpha$). This peak is much less pronounced for $[300, 600]$ eV, in agreement with the energy-localized butterfly distribution in spacecraft observations (see Figure 3.3(d-j)). The observed pitch-angle distributions (likewise normalized) show a similar butterfly distribution for $[50, 250]$ eV electrons, see Figure 3.7(a).

To confirm this comparison with statistical results, we use our dataset of foreshock transients and select intervals with intense whistler-mode waves. Then we use the same format as in Figure 3.6, and plot normalized pitch-angle distributions of electron measurements as-

sociated with whistler-mode waves. Figure 3.7(b) shows that statistical events demonstrate similar butterfly distributions for $50 - 250$ eV electrons as in simulation results.

Note that the enhancement of $[50, 250]$ eV at high pitch angles ($> 75°$; shown by the dashed curve) is produced by low-energy electrons accelerated via multiple phase trappings within a series of wave-packets [Hiraga and Omura, 2020]. The efficiency of such multiple trapping strongly depends on the wave phase decoherence between wave packets [Zhang et al., 2020], and can be well modeled only with detailed statistical analysis of wave phase decoherence. The absence of such a strong $> 75°$ peak in observational data suggests that our model overestimates the multiple-trapping effect, and further investigation of wave decoherence would be needed for the model modification.

3.4 Summary

Intense whistler-mode waves are observed around interplanetary shocks [Wilson et al., 2013, Davis et al., 2021] and Earth's bow shock [Hull et al., 2012, Hull et al., 2020, Page et al., 2021, Shi et al., 2023b]. Resonant interactions between electrons and such intense waves may result in strong pitch-angle scattering [Oka et al., 2017, Oka et al., 2019, Shi et al., 2020], which is important for electron participation in stochastic shock drift acceleration [Amano et al., 2020, Amano et al., 2022]. Moreover, in the presence of ambient magnetic field gradients and shock-related electrostatic fields, whistler-mode waves may directly accelerate solar wind electrons [Kuramitsu and Krasnoselskikh, 2005, Artemyev et al., 2022b]. This important role of whistler-mode waves for suprathermal electron dynamics drives many theoretical investigations of wave-particle resonant interactions around shocks (see the discussions in Ref. [Wilson et al., 2014, Amano et al., 2020]).

We have presented clear evidence that whistler-mode waves can contribute to the solar wind electron acceleration within foreshock transients. Wave amplitudes are sufficiently high to provide nonlinear resonant interactions with electrons, which would speed up this

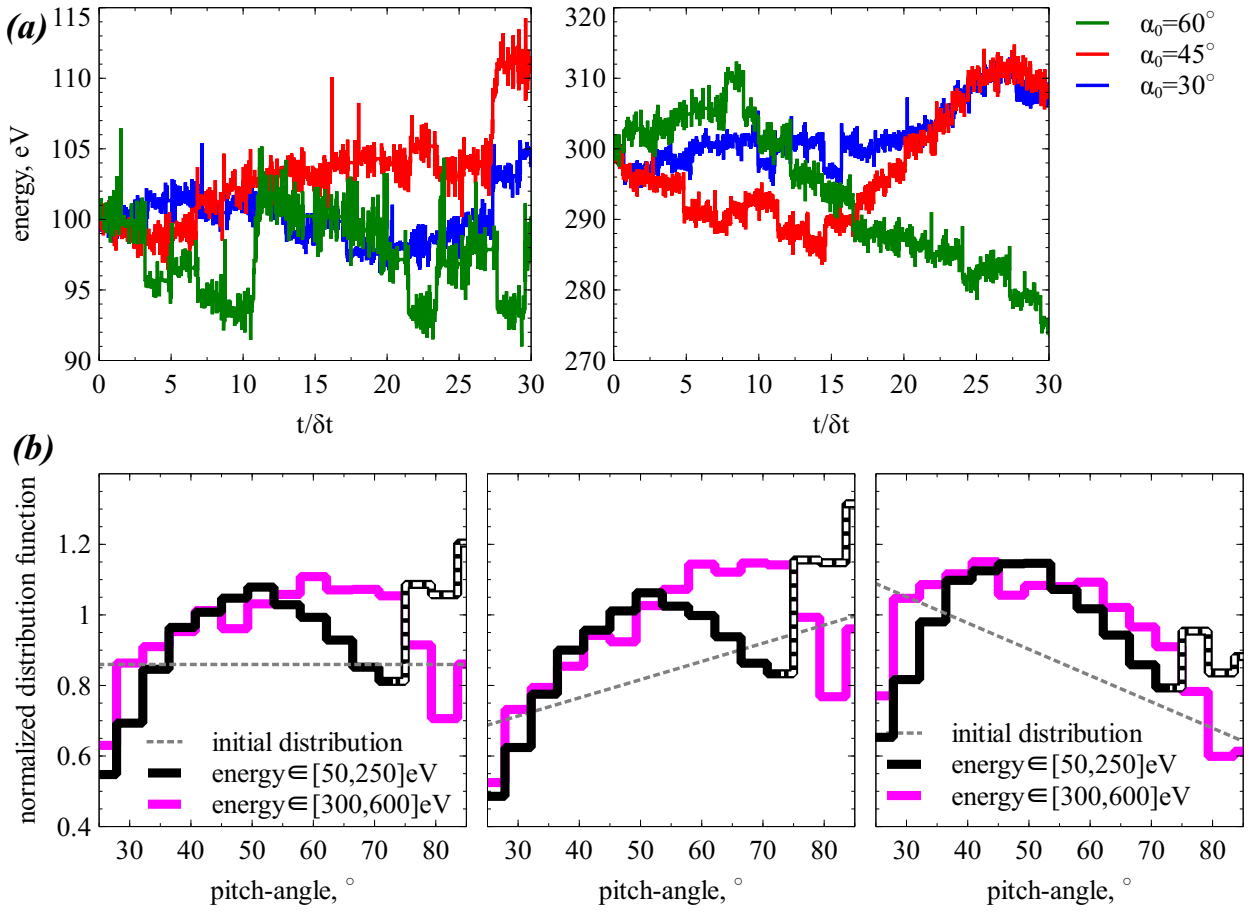

Figure 3.6: Model results for electron resonant interactions with whistler-mode waves. Panels (a) show examples of test particle trajectories for two initial energies and different pitch-angles. Time is normalized to the model time step, $\delta t = R\Omega_{pe}/c\Omega_{ce} \approx 0.15$ seconds. Panels (b) show examples of the evolution of initial pitch-angle distributions after $\sim$ 10 resonant interactions (three initial cases are shown in three panels). Black and magenta colors show different energy ranges (initial pitch-angle distribution is the same for both energy ranges).

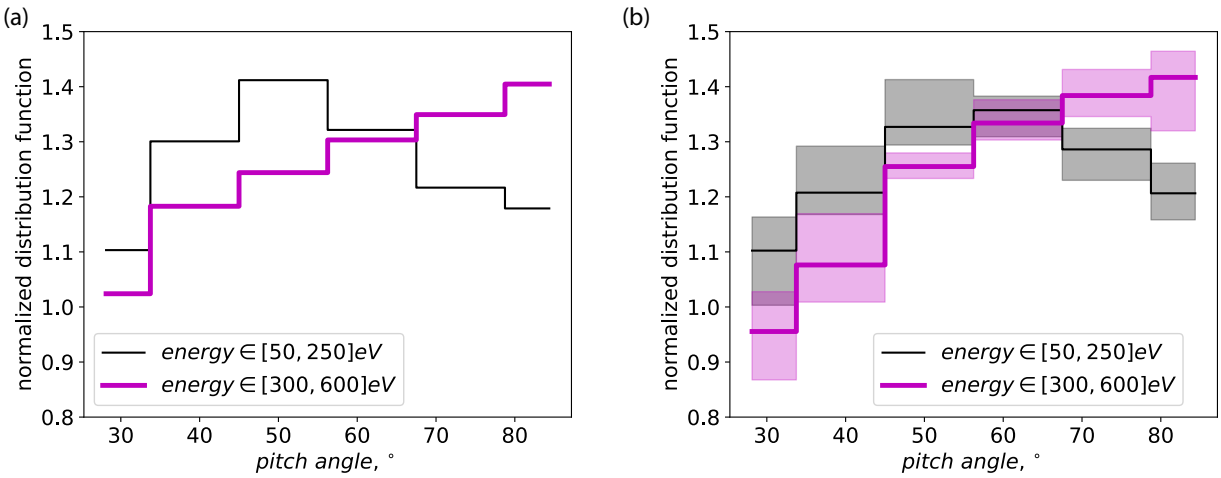

Figure 3.7: Statistical results of electron pitch-angle distributions for intervals with intense whistler-mode waves. Panel (a) shows the normalized pitch-angle distribution during 20:26:55–20:27:00 UT for the event from Figure 1 of the main text. The flux of 50-250eV electrons has a peak around 50° pitch angle, consistent with the model results. Panel (b) shows the normalized pitch-angle distribution for 16 events (different foreshock transients). Solid lines are medium values. The upper and lower boundaries of the shaded region are the 25th and 75th percentile of the normalized flux, respectively.

acceleration. Such nonlinear resonant acceleration and formation of electron butterfly pitch-angle distributions are typical in Earth's inner magnetosphere [Fennell et al., 2015, Gan et al., 2020b, Saito and Miyoshi, 2022, Peng et al., 2022], but this is the first time it has been reported in the foreshock region.

Whistler-mode wave generation around the bow shock is a natural consequence of electron adiabatic heating that creates unstable electron distributions. Whistler-mode waves are nearly always observed inside foreshock transients due to their compressive nature and 15% are intense enough to nonlinearly interact with electrons [Shi et al., 2023b]. Whistler waves transfer energy between the heated population and a small resonantly accelerated electron population [Shklyar, 2011]. Thus, wave generation and resonant wave-particle interactions enable the formation of a suprathermal electron population, which can be further injected into the shock environment where it can undergo further diffusive shock acceleration [Amano et al., 2020]. The upper energy limit of accelerated electrons should be determined by the ambient magnetic field [Omura et al., 2015, Allison and Shprits, 2020]. Similar scaling for solar wind electrons would result in an acceleration from $10 - 100$eV up to ≤ 100keV. Such acceleration, therefore, acting together with adiabatic and diffusive shock acceleration mechanisms, might be commonplace and explain the formation of relativistic electron populations commonly observed around Earth's bow shock [Wilson et al., 2016a, Liu et al., 2019]. This compound acceleration is discussed in more detail in Chapter 5.

CHAPTER 4

Probabilistic Approach and Mapping Technique

4.1 Introduction

Chapter 3 demonstrates that whistler-mode waves can effectively interact with electrons through nonlinear interactions. It also shows that test particle simulations can successfully trace electron dynamics during these interactions. However, these simulations require significant computational resources, especially when modeling a large population of electrons necessary to replicate low-probability effects. Therefore, there is a need to develop theoretical approaches that can reduce computational time. In this chapter, we explore two theoretical approaches for describing wave-particle interactions. These approaches take into account nonlinear resonant interactions, gradients of the background density and magnetic field, and the fine structure of waveforms, typically characterized by short, intense wave-packet trains.

The basic theoretical approach for modeling wave-particle resonant interactions, the quasi-linear theory [Vedenov et al., 1962, Drummond and Pines, 1962], can be used to estimate the electron scattering rates provided by whistler-mode waves [Veltri and Zimbardo, 1993, Amano et al., 2020]. However, the criteria for this theory (low wave intensity, broad wave spectrum; see Ref. [Karpman, 1974, Shapiro and Sagdeev, 1997]) can be violated around the shock, where the observed whistler-mode waves are very intense and sufficiently narrow-band [Hull et al., 2020, Shi et al., 2023b, Artemyev et al., 2022b]. Such waves may resonate with electrons nonlinearly. Presently, models of nonlinear resonant interactions are mostly developed for Earth's inner magnetosphere (see, e.g., Refs. [Shklyar and Mat-

sumoto, 2009, Albert et al., 2013, Hsieh and Omura, 2017, Artemyev et al., 2021c] and references therein) and require significant modifications to be suitable for the plasma and wave characteristics commonly observed around Earth's bow shock. In this chapter we seek to advance such models for planetary shocks, and in particular Earth's bow shock, which is most accessible representative.

Intense whistler-mode waves detected at the bow shock and in the foreshock region are strongly modulated by low-frequency compressional waves [Hull et al., 2012, Hull et al., 2020], i.e. whistler-mode waves propagate in short wave packages. Figure 4.1(left panel) shows the probability distribution of whistler-mode waves in the space of wave amplitude B_w, in nT, and wave-packet size β, in wave periods. Although there are long and intense wave-packets with $B_w > 100$pT and $\beta \geq 20$, the majority of the observed intense waves propagate in short wave-packets, characterized by $\beta < 20$. The number of wave-packets decreases with the wave-packet size as $N \sim \beta^{-1.67}$. Such a strong wave modulation (short packet size) can significantly reduce the efficiency of nonlinear resonant interactions [Tao et al., 2013, Allanson et al., 2020, Allanson et al., 2021], because electrons spend less time in resonant interactions with short wave-packets and cannot gain substantial energy (see simulation results in Refs. [Mourenas et al., 2018, Zhang et al., 2020, An et al., 2022, Gan et al., 2022]).

Figure 4.1(right panel) illustrates how wave-packet size affects the electron nonlinear resonant interactions. In the case of infinitely long wave-packets ($\beta \to \infty$), resonant electrons with the same initial energies and pitch-angles are divided into two populations. The first population consists of a small group (low probability) of phase-trapped electrons that experience a significant energy gain ($\Delta E > 0$). The second population comprises a larger group (high probability) of phase-bunched electrons that undergo a minor energy loss ($\Delta E < 0$). For a finite wave-packet size ($\beta = 50$), the population of phase-trapped electrons increases due to a higher probability of trapping. For comparison, we also show the ΔE-distribution for the quasi-linear scattering regime (small wave intensity) with scaled $\Delta E \to \Delta E/B_w$.

This distribution shows a spread of ΔE within $[-\max\Delta E, \max\Delta E]$, where $\max\Delta E$ is approximately the energy gain of the trapped population. The significant disparity observed in the ΔE-distributions between the quasi-linear and the nonlinear resonant regime, as well as between the different values of β highlights the importance of incorporating realistic wave-packet characteristics into the model of wave-particle resonant interactions around the bow shock.

In the following of this chapter, we first describe a probabilistic approach which enables us to trace the long-term evolution of electron distribution functions. This approach assumes that waves are sufficiently incoherent (wave-packets are short) to reduce the efficiency of nonlinear resonant interactions and hence lead to diffusive particle scatterings. Such a diffusion by intense wave-packets is quite different from quasi-linear diffusion [Shklyar, 2021, Frantsuzov et al., 2023, Gan et al., 2022]. Then we describe how this probabilistic approach can be merged with a mapping technique [Benkadda et al., 1996, Khazanov et al., 2013, Khazanov et al., 2014, Artemyev et al., 2020] to model electron dynamics in systems with a significant effect from nonlinear resonance with long wave-packets.

4.2 Hamiltonian Equations For Resonant Systems

Theoretical models proposed for wave resonant interactions within electrons bouncing along magnetic field lines in the radiation belts [Tao et al., 2008, Artemyev et al., 2017, Lukin et al., 2021] assume multiple, independent resonant interactions described by probability distribution functions (constructed theoretically or derived numerically) of energy and pitch-angle changes during each interaction. Such multiple resonant interactions are possible when particles follow the bounce motion (and periodically attain resonance with the waves) or when they resonate with multiple waves (different wave-packets spatially distributed along particle trajectories). Around Earth's foreshock region, electrons can also undergo such multiple interactions. Figure 4.2 (bottom) depicts the electron dynamics and wave-particle

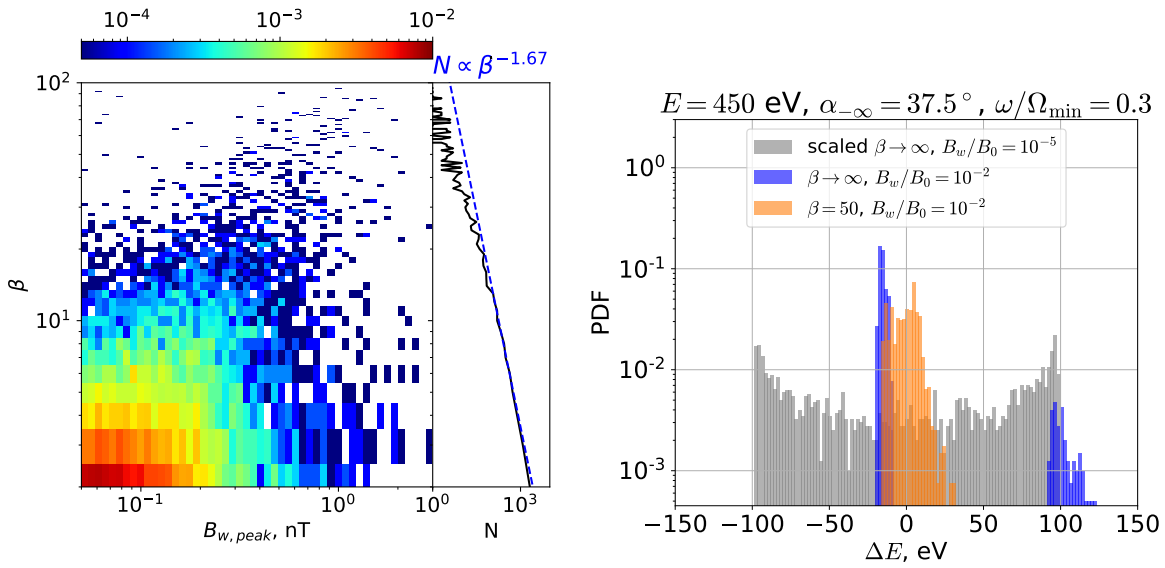

Figure 4.1: The distribution of waves in (B_w, β) space (left). The distribution of waves in (B_w, β) space for the foreshock region (see details of wave statistics in Ref. [Shi et al., 2023b]). We present a 2D probability distribution in the space of peak wave-packet amplitude and the wave-packet size β, which is measured in terms of wave periods. Additionally, we display a 1D distribution for the number of wave-packets at various wave-packet sizes, β, and we fit this distribution with a power law function of the form $N \sim \beta^{-1.67}$. (right) Three examples of probability distributions of energy change ΔE for a single resonant interaction of electrons (having the same initial energy/pitch-angle): (grey) low-intensity wave-packet, (blue) long intense wave-packet, and (orange) short intense wave-packet. The wave magnetic field is normalized to the minimum value of the ambient magnetic field (see details in the text), and for the distribution with $B_w/B_0 = 10^{-5}$, we rescale $\Delta E \to \Delta E \cdot 10^3$ to compare with the other two ΔE-distributions evaluated for $B_w/B_0 = 10^{-2}$.

interaction for a foreshock transient (an example is shown on the left) and for a bow shock (an example is shown on the right). In both environments, the background plasma density varies strongly with the background magnetic field (see Figure 4.2(a,d) and (h,k)), and the f_{pe}/f_{ce} ratio is large (≈ 100) and almost constant. The whistler-mode wave characteristics are also quite similar in these two environments: waves propagate in the form of intense ($\sim 1\%$ of background magnetic field), short wave-packets (see Figure 4.2(g,n)). This allows us to apply our model to both systems, with equal efficacy. For the bow shock region, we are interested in reflected electrons, which can be scattered by whistler-mode waves upstream and turned back to the shock. These electrons should resonate with waves that are generated upstream and propagating downstream. For foreshock transients, electrons may be trapped between the shock of the foreshock transient and the bow shock. In that case, the electrons bounce back and forth, undergoing multiple resonant interactions with waves generated within the core of the foreshock transients.

We employ two models: one for the bow shock and the other for the foreshock region. Both models describe electron (mass m_e, charge $-e$) motion in inhomogeneous magnetic fields with field-aligned whistler mode waves [Artemyev et al., 2022b]:

$$\begin{aligned} H &= \frac{p_\parallel^2}{2m_e} + \mu\Omega_0(s) - e\Phi(s) + U_w(s,\mu)\cos(\phi+\psi) \\ U_w &= \sqrt{\frac{2\mu\Omega_0(s)}{m_e c^2}}\frac{eB_w}{k(s)} \end{aligned} \tag{4.1}$$

where $(s, p_\parallel)$ are conjugate variables of parallel coordinate and momentum, (ψ, μ) are conjugate variables of gyrophase and normalized magnetic moment ($\mu = E\sin^2\alpha/\Omega_0$ where E is the electron energy and α is the electron pitch-angle), $\Omega_0(s) > 0$ is the electron gyrofrequency, $\Phi(s)$ is the electrostatic potential describing the polarization electric fields due to ion-electron decoupling around strong magnetic field gradients [Scudder, 1995, Gedalin, 1996], B_w is the wave amplitude, ϕ is the wave phase that determines the wave frequency $\omega = -\partial\phi/\partial t$ and the local wave number $k(s) = \partial\phi/\partial s$. We use the simplified cold plasma dispersion relation $kc = \Omega_{pe}(s)\cdot(\Omega_0(s)/\omega - 1)^{-1/2}$, see Ref. [Stix, 1962], where $\Omega_{pe}(s)$ is the

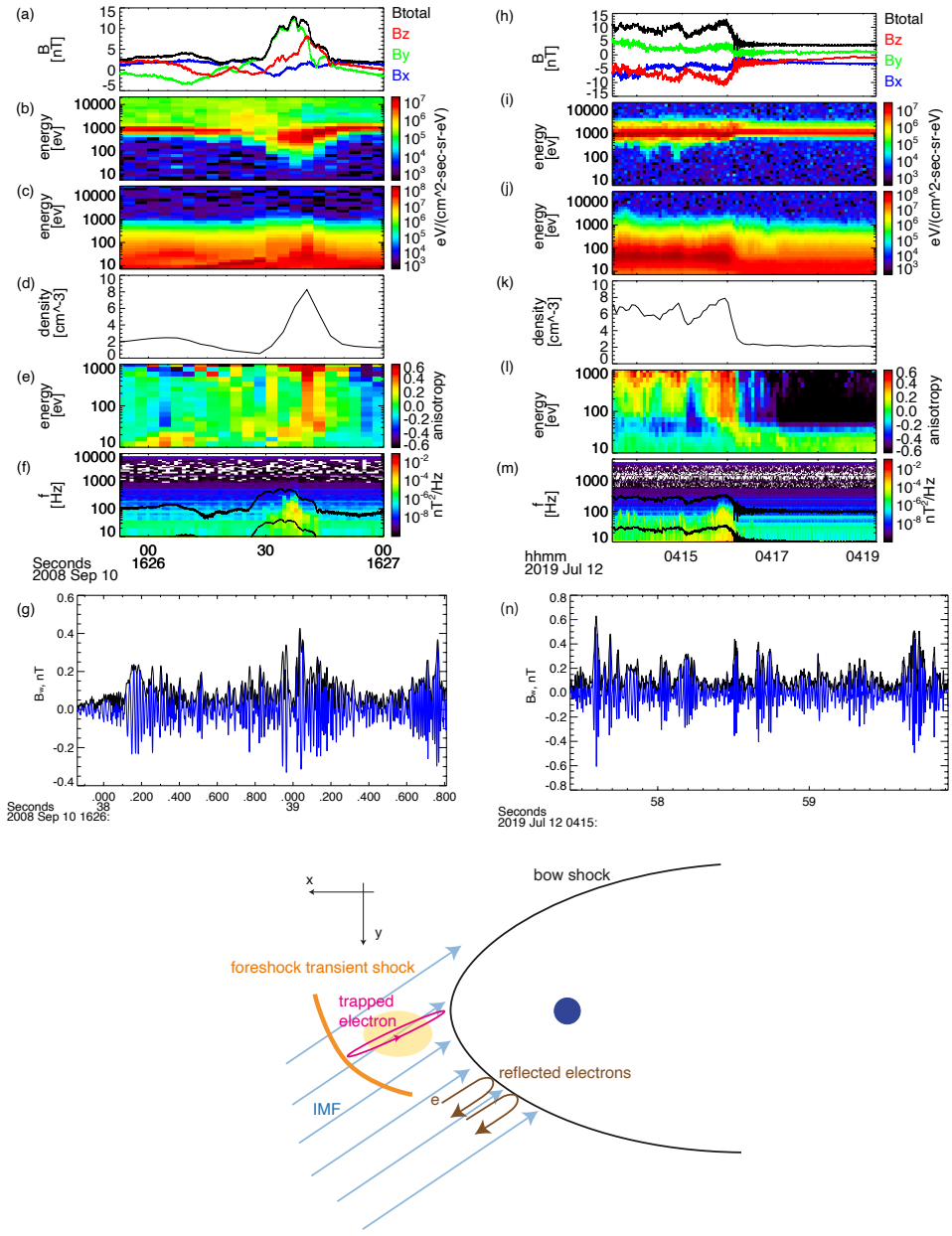

Figure 4.2: Observations of a foreshock transient (left) and the distant bow shock (right) by the THEMIS spacecraft. The bottom panel depicts the electron dynamics (brown: reflection; purple: trapping) and wave-particle resonant interactions (in a yellow-highlighted interaction region) at the bow shock (black) and within the foreshock transient (demarcated by the bow shock and the shock upstream of it in orange).

plasma frequency.

The bow shock is described simply by a magnetic field ramp, $\Omega_0(s) = \Omega_{\min} \cdot (1 + 3b(s))$, a compressional plasma density increase $\Omega_{pe}(s)/\Omega_{pe,\min} \propto \sqrt{\Omega_0(s)/\Omega_{\min}}$, and an electrostatic potential $\Phi(s) = \Phi_0 b(s)$ (see, e.g., Ref. [Gedalin, 1996]). Our choice of parameters is typical for Earth's bow shock: $(\Omega_{pe}/\Omega_0)_{\min} = 100$, $\Phi_0 \in [0, 100]$ eV (see Refs. [Goodrich and Scudder, 1984, Scudder, 1995]). Function $b(s) = (1/2) \cdot (1 + \tanh(s/L))$ varies from 0 to 1 with a spatial scale $L \approx 1000$ km (the typical scale of magnetic field variations at the bow shock, see Ref. [Krasnoselskikh et al., 2013]). This spatial scale determines the large system parameter $\eta = L/d_e \sim 10^4$, with $d_e = c/\Omega_{pe,\min}$ being the electron inertial length, the wavelength scale.

The foreshock magnetic field model corresponds to foreshock transients, localized enhancements of the magnetic field that lead to electron magnetic trapping (see Paper 1 [Shi et al., 2023] and Refs. [Shi et al., 2020, Shi et al., 2023b]). This magnetic field model has a magnetic configuration akin to a magnetic field bottle, $\Omega_0(s) = \Omega_{\min}\sqrt{1 + (s/L)^2}$, a compressional plasma density increase $\Omega_{pe}(s) = 100\Omega_0(s)$, and a large system parameter $\eta = L/d_e \sim 10^4$. We do not include any electrostatic potential mostly because there is no observational study of such potential in foreshock transients.

The large parameter η and small wave amplitude $B_w/B_0 \in [10^{-4}, 10^{-2}]$ (see Refs. [Hull et al., 2012, Hull et al., 2020, Shi et al., 2023b]) make Equation (4.1) a slow-fast (slow s, $p_\parallel$ variables and fast ϕ, ψ phases) one with a small resonant perturbation $\sim U_w$. To demonstrate the main properties of nonlinear resonant interactions in the Hamiltonian system (4.1), we follow the procedure of typical slow-fast resonant system analysis (see Refs. [Neishtadt and Vasiliev, 2006, Neishtadt, 2014, Artemyev et al., 2018a]).

First, we introduce phase $\zeta = \phi + \psi$ as a new conjugate coordinate to a new magnetic moment $\tilde{\mu}$. For this we use a generating function $F(\phi, s; \tilde{\mu}, p; t) = (\phi + \psi)\tilde{\mu} + ps$ with new

coordinate-momentum pairs $(\tilde{s}, p)$ and $(\zeta, \tilde{\mu})$:

$$\begin{aligned} \zeta =& \frac{\partial F}{\partial \tilde{\mu}} = \phi + \psi, \quad \mu = \frac{\partial F}{\partial \psi} = \tilde{\mu}, \\ \tilde{s} =& \frac{\partial F}{\partial p} = s, \quad p_{\parallel} = \frac{\partial F}{\partial s} = p + k\tilde{\mu}. \end{aligned} \tag{4.2}$$

Because $\tilde{\mu} = \mu$ and $\tilde{s} = s$, the tilde sign will be omitted. The new Hamiltonian $\mathcal{H} = H + \partial F/\partial t$ has the form:

$$\mathcal{H} = \frac{(p + k\mu)^2}{2m_e} + \mu(\Omega_0 - \omega) - e\Phi(s) + U_w(s, \mu)\cos\zeta \tag{4.3}$$

This Hamiltonian describes a conservative system because $\partial\mathcal{H}/\partial t = 0$.

The resonance condition in new Hamiltonian variables is

$$\dot{\zeta} = \frac{\partial \mathcal{H}}{\partial \mu} \approx k\frac{(p + k\mu)}{m_e} + \Omega_0 - \omega = 0. \tag{4.4}$$

Equation (4.4) determines the resonant momentum $\mu = \mu_R(s, p)$:

$$\mu_R(s, p) = \frac{m_e}{k^2}\left(\omega - \Omega_0 - k\frac{p}{m_e}\right). \tag{4.5}$$

Expansion of the Hamiltonian near the resonance gives:

$$\begin{aligned} \mathcal{H} \approx& \Lambda(s, p) + \frac{k^2}{2m_e}(\mu - \mu_R)^2 + U_w(s, \mu_R)\cos\zeta, \\ \Lambda(s, p) =& \frac{(p + k\mu_R)^2}{2m_e} + \mu_R(\Omega_0 - \omega) - e\Phi. \end{aligned} \tag{4.6}$$

To introduce the canonical variable $P_\zeta = \mu - \mu_R$, we use the generating function $W(\zeta, s; P_\zeta, \tilde{p}) = (P_\zeta + \mu_R)\zeta + \tilde{p}s$ with new conjugate variables:

$$\begin{aligned} \tilde{\zeta} =& \frac{\partial W}{\partial P_\zeta} = \zeta, \quad \mu = \frac{\partial W}{\partial \zeta} = P_\zeta + \mu_R, \\ \tilde{s} =& \frac{\partial W}{\partial \tilde{p}} = s + \frac{\partial \mu_R}{\partial \tilde{p}}\zeta, \quad p = \frac{\partial W}{\partial \tilde{s}} = \tilde{p} + \frac{\partial \mu_R}{\partial \tilde{s}}\zeta. \end{aligned} \tag{4.7}$$

The first term $\Lambda(s, p)$ in the new Hamiltonian $\tilde{\mathcal{H}}$ will differ from the first term $\Lambda(s, p)$ from the Hamiltonian (4.6), because of the difference between old variables (s, p) and new variables $(\tilde{s}, \tilde{p})$. Because the second term in the expressions for the old variables is small, it allows us

to expand the Λ term in the Hamiltonian. Noticing that $s = \tilde{s} + \{\mu_R, \tilde{s}\}\zeta$, $p = \tilde{p} + \{\mu_R, \tilde{p}\}\zeta$ where $\{\cdot, \cdot\}$ are the Poisson brackets, it can be shown that

$$\Lambda(s, p) = \Lambda(\tilde{s}, \tilde{p}) + \{\mu_R, \Lambda\}\zeta,$$

and the new Hamiltonian can be written as:

$$\tilde{H} \approx \Lambda(\tilde{s}, \tilde{p}) + \frac{k^2}{2m_e} P_\zeta^2 + \{\mu_R, \Lambda\}\zeta + U_w(s, \mu_R)\cos\zeta. \tag{4.8}$$

In this form, the first term $\Lambda(\tilde{s}, \tilde{p})$ describes the slow motion in the $(s, p) \approx (\tilde{s}, \tilde{p})$ plane while the following three are analogous to the nonlinear pendulum Hamiltonian:

$$\mathcal{H}_\zeta = \frac{1}{2M} P_\zeta^2 + \mathrm{A}\zeta + \mathrm{B}\cos\zeta, \tag{4.9}$$

which describes the fast motion near the resonance in the (ζ, P_ζ) plane. Coefficients M, A, B depend on the coordinates in the (s, p) plane:

$$M = \frac{m_e}{k^2}, \quad \mathrm{B} = U_w(s, \mu_R) = \sqrt{\frac{2\mu_R\Omega_0}{m_e c^2}}\frac{eB_w}{k}, \tag{4.10}$$

and

$$\mathrm{A} = -\frac{\partial \ln k}{\partial s}\frac{p_{\parallel,R}^2}{km_e} - \frac{\partial\Omega_0}{\partial s}\frac{p_{\parallel,R} - k\mu_R}{k^2} - \frac{e}{k}\frac{\partial\Phi}{\partial s}, \tag{4.11}$$

where $p_{\parallel,R} = m_e(\omega - \Omega_0)/k$ is the solution of equation $\dot{\phi} + \dot{\psi} = 0$ for the Hamiltonian (4.1) and μ_R is defined through the electron's resonance energy and the coordinate s of the resonance.

The phase portrait of the Hamiltonian $\mathcal{H}_\zeta$ in (ζ, P_ζ) is presented in Figure 4.3(top panel). This portrait contains two types of trajectories: transient trajectories cross the resonance $P_\zeta = 0$ once – electrons moving along such trajectories experience scattering with small energy/pitch-angle change; and phase trapped trajectories which are closed around the resonance $P_\zeta = 0$ – electrons moving along such trajectories stay around the resonance for a long time (see details in Refs. [Omura et al., 1991, Shklyar and Matsumoto, 2009, Artemyev

et al., 2018a]). The trajectory demarcating the phase domains with transient and phase-trapped trajectories is the separatrix. An important system parameter is the area of the region enclosed by the separatrix:

$$\mathcal{S} = 2\sqrt{2M\mathrm{B}} \int_{\zeta_X}^{\zeta_{max}} \sqrt{\cos\zeta_X - \cos\zeta + \frac{\mathrm{A}}{\mathrm{B}}(\zeta_X - \zeta)}\mathrm{d}\zeta, \tag{4.12}$$

where ζ_X is the solution of equations $P_\zeta = 0$, $\dot{P}_\zeta \to 0$. Area $\mathcal{S}$ depends on (s, p) coordinates in the resonance, where $p = p_{\parallel,R} - k\mu_R$. The combination of the conservation law $E - e\Phi - \omega\mu = h = const$ (see Eq. (4.3)) and the resonance condition makes $\mathcal{S}$ a function of energy E only, i.e., $\mathcal{S} = \mathcal{S}(E)$ (see Figure 4.3(bottom) showing three examples of $\mathcal{S}(E)$). This function characterizes the electron energy change during resonant interactions, ΔE, and the probability of electron phase trapping, Π (see Refs. [Shklyar, 1981, Solovev and Shkliar, 1986, Albert, 1993]). Such probability can be defined as the ratio of resonant electrons that experience phase trapping for a single resonant interaction to the total number of resonant electrons [Neishtadt, 1975, Shklyar, 1981].

The initial energy E determines the phase portrait in (ζ, P_ζ) plane but cannot describe electron trajectories in the phase portrait, because they also depend on the $\mathcal{H}_\zeta$ magnitude. The coefficients in $\mathcal{H}_\zeta$ depend on E, whereas phase ζ is a fast oscillating variable. Thus, we may introduce a normalized energy $\mathcal{H}_\zeta$ near the resonance $P_\zeta = 0$, $2\pi\xi = \zeta_R + (\mathrm{B/A})\cos\zeta_R$, and treat ξ as a random variable. An important property of the Hamiltonian (4.9) is that the ξ-distribution is uniform (see numerical tests in Refs. [Itin et al., 2000, Frantsuzov et al., 2023]). Therefore, we can use $\mathcal{S}(E)$ and the random variable ξ to characterize the wave-particle resonant interactions [Artemyev et al., 2018b, Artemyev et al., 2020].

Note that the Hamiltonian $\tilde{H}$ and Eq. (4.9) have been derived for electron pitch-angles that are not too small (i.e., not-too-small μ). However, when dealing with the resonant interaction of whistler-mode waves with nearly field-aligned electrons, a different approach is needed, as discussed in references [Artemyev et al., 2021a, Albert et al., 2021, Albert et al., 2022b]. Electrons with small pitch-angles resonating with intense whistler-mode waves

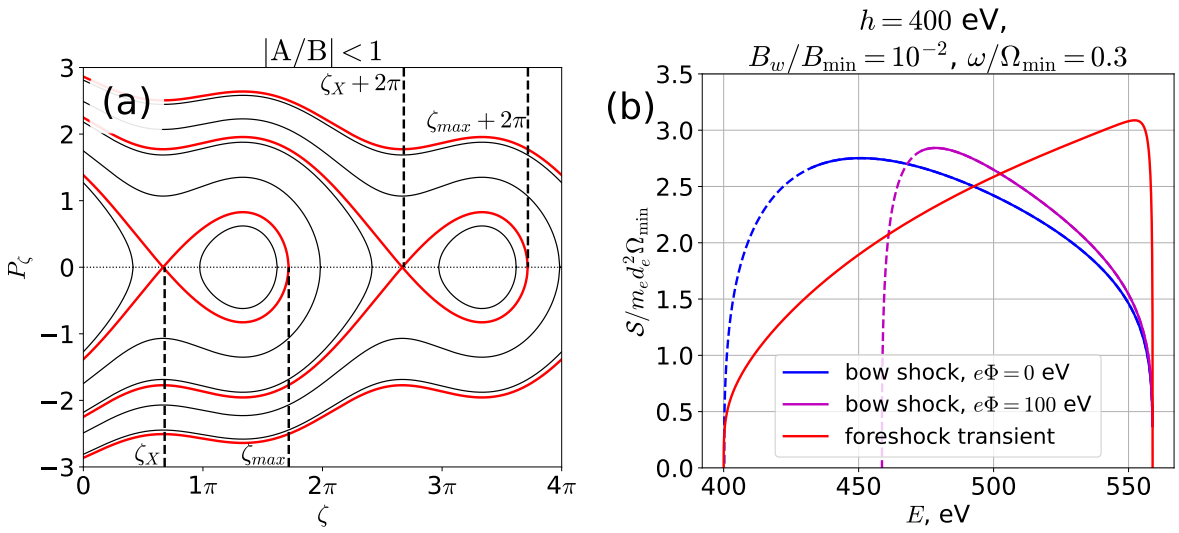

Figure 4.3: (a) A phase portrait of the Hamiltonian (4.9) with $|A/B| < 1$. (b) The separatrix area $\mathcal{S}$ is a function of the initial energy. We plot $\mathcal{S}$ for bow shock and foreshock transient models. For the bow shock model, we trace electrons that move from the upstream region, get reflected from the shock, and then resonate with whistler-mode waves. Dashed lines show the prohibited initial energy range: electrons with such initial energies cannot move away from the shock, because these electrons are not reflected by the shock and go downstream (for a given h value, this corresponds to a certain range of the initial pitch-angle). The maximum resonance energy corresponds to a resonance location (s) at the minimum of the ambient magnetic field.

exhibit a phenomenon known as anomalous trapping, where all particles become phase-trapped and experience an increase in pitch-angle during a single resonant interaction, as described in references [Kitahara and Katoh, 2019, Gan et al., 2020a]. While our model does not reproduce this effect, we simulate it by implementing a scheme for electron losses: particles with pitch-angles below 18° are assumed to escape from the magnetic trap with $\max B / \min B = 10$, which is common for foreshock transients [Shi et al., 2023b]. These escaping particles are then replaced by new solar wind particles with intermediate to high pitch-angles.

Figure 4.4 shows examples of electron trajectories from the numerical integration of the Hamiltonian equations of motion for two systems with different parameters. There are two main effects of nonlinear resonant interactions: phase bunching characterized by energy decrease and phase trapping characterized by large energy increase (see Refs. [Karpman et al., 1975, Trakhtengerts et al., 2003, Albert, 2000, Omura et al., 1991]). We aim to theoretically describe electron distribution dynamics driven by multiple nonlinear resonant interactions. To achieve this, we employ two approaches: probabilistic analysis and mapping techniques.

4.2.1 Probabilistic Approach

To characterize wave-particle resonant interactions, we will use the probability distribution $\mathcal{P}(\Delta E)$ of energy change for a single resonant interaction. For fixed system parameters, this distribution will depend on the initial electron energy E and pitch-angle α_0. The pitch-angle can be substituted by the initial electron magnetic moment $\mu_0 = E \sin^2 \alpha_0 / \Omega_{\min}$ (we set initial conditions at the magnetic field minimum). Equation (4.1) has one integral of motion: $E - \omega\mu = h = const$ (see, e.g., Ref. [Shklyar and Matsumoto, 2009]). This is a constant because there are no electric fields in the reference frame moving with the wave ($t \to t + \omega t$), and the particle energy $\sim h$ in this reference frame is conserved. Therefore, we can use the probability distribution function $\mathcal{P}(\Delta E, E)$ defined in the $(\Delta E, E)$ space for fixed

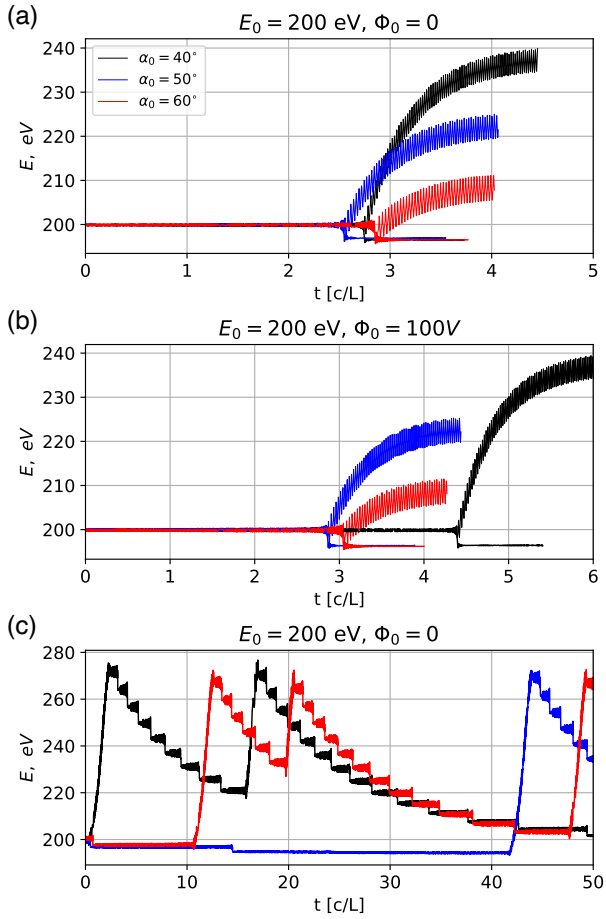

Figure 4.4: Examples of electron energy evolution due to the interactions with the prescribed wave field (energy versus time): for the bow shock model with $\Phi_0 = 0$ (a), for the bow shock with $\Phi_0 = 100$V (b), and for the foreshock transient (c). Each panel shows three trajectories with the same initial energy 200eV and three different initial pitch-angles.

h. For waves with infinitely long wave-packets $\sim \cos(\phi + \psi)$, such probability distribution functions can be derived analytically [Vainchtein et al., 2018, Artemyev et al., 2022c]. In reality, however, waves propagate in the form of wave-packets (see Figure 4.2 and Refs. [Hull et al., 2012, Hull et al., 2020, Shi et al., 2023b]), where $\mathcal{P}$ can only be determined from numerical simulations [Omura et al., 2015, Hsieh and Omura, 2017, Artemyev et al., 2019c]. We introduce the wave field modulation, $\cos(\phi + \psi) \rightarrow f(\phi)\cos(\phi + \psi)$, and numerically evaluate $\mathcal{P}$ for different modulation characteristics. Function $f(\phi)$ describes the wave-packet train, and we use a simple form $f(\phi) = \exp(-5 \cdot \cos^2(\phi/2\pi\beta))$ with β denoting the wave-packet size [Tsai et al., 2022]. An additional model parameter is the wave phase coherence number measured by the number of contiguous coherent wave packets, N_c. This parameter describes how many wave packets within the train have the same initial ϕ, i.e., maintain phase coherence from one packet to the next one. This effect can be modeled by a finite N_c, which will reduce the efficiency of the phase trapping and acceleration. The concept of a wave-packet train assumes that idealized plane wave $\sim \cos(\phi + \psi)$ is separated into an infinite number of wave-packets, $N_c \rightarrow \infty$. The duration of resonant interactions between electrons and plane waves is limited by the inhomogeneity of the background magnetic field. Similarly, the resonant interactions between electrons and an infinite ensemble of coherent wave-packets also have this limitation. However, for wave-packets, there is an additional effect of wave phase decoherence at the edge of packets, and such decoherence can further limit the number of wave-packets that particles can interact with. The system with $N_c \rightarrow \infty$ corresponds to the situation when all wave packets are generated in the same source region by the same particle population and their modulation is attributed to quasi-periodical currents of phase trapped electrons [Omura, 2021, Tao et al., 2020, Nunn et al., 2021]. Thus, there is no variation (destruction) of the wave phase among wave packets. In this case, electrons may be trapped into the next wave packet after escaping from the previous one, and such multi-trapping would result in effective electron acceleration, similar to infinitely long wave-packets [Hiraga and Omura, 2020]. However, different wave-packets are often generated

in different source regions and their phases are not coherent across the entire packet train [Zhang et al., 2020, Mourenas et al., 2022]. To account for the effect of phase decoherence, a finite value parameter N_c is introduced to determine the maximum number of wave-packets that particles can resonate with. This is the upper limit of wave-packets and particles can escape from the resonant interactions even before reaching N_c. Note that this discussion is relevant only to the phase trapping because the phase bunching occurs once per period of particle motion at the resonance and does not depend on N_c.

4.2.2 Mapping Technique

The ξ-averaged characteristics of nonlinear resonant interactions (energy changes due to bunching $\langle \Delta E \rangle_{bunching}$ and trapping $\langle \Delta E \rangle_{trapping}$, and the trapping probability Π) are determined by the profile $\mathcal{S}(E)$ alone [Artemyev et al., 2018b, Artemyev et al., 2020]:

$$\langle \Delta E \rangle_{bunching} = \omega \langle \Delta \mu \rangle_{bunching} = -\frac{\omega}{2\pi} \mathcal{S} \tag{4.13}$$

$$\mathcal{S}\left(E + \langle \Delta E \rangle_{trapping}\right) = \mathcal{S}\left(E\right), \quad \Pi = -\frac{\omega}{2\pi}\frac{d\mathcal{S}}{dE} \tag{4.14}$$

with $E - e\Phi - \omega\mu = h = const$. Therefore, knowing $\mathcal{S}$ (see, e.g., Figure 4.3(bottom)), we may construct a map for energy changes:

$$E_{n+1} = E_n + \begin{cases} \langle \Delta E(E_n) \rangle_{bunching}, & \xi \in \Xi_{bunching}(E_n) \\ \langle \Delta E(E_n) \rangle_{trapping}, & \xi \notin \Xi_{bunching}(E_n) \end{cases} \tag{4.15}$$

where n is the number of resonant interactions (map iteration number), $\Xi_{bunching}(E)$ determines the range of ξ corresponding to bunched particles, and ξ is a random variable that is uniformly distributed over $\xi \in [0, 1]$ (see Refs. [Itin et al., 2000, Frantsuzov et al., 2023]). Although the function $\Xi_{bunching}(E)$ can be quite complicated (see details in, e.g., Ref. [Albert et al., 2022a]), it can be approximated by a simple step-wise function [Artemyev et al., 2020]:

$$E_{n+1} = E_n + \begin{cases} \langle \Delta E \rangle_{bunching}\,, & \xi \in (\Pi(E_n), 1] \\ \langle \Delta E \rangle_{trapping}\,, & \xi \in [0, \Pi(E_n)] \end{cases} \tag{4.16}$$

This map should be supplemented by the equation of pitch-angle changes (α_0 is defined as the pitch angle at the minimum Ω_0): $\alpha_{0,n+1} = \alpha_{0,n} + \Delta\alpha$, with $\Delta\alpha$ determined from $E_{n+1} - e\Phi_R(E_{n+1}, \alpha_{0,n+1}) - \omega\mu(E_{n+1}, \alpha_{0,n+1}) = E_n - e\Phi_R(E_n, \alpha_{0,n}) - \omega\mu(E_n, \alpha_{0,n})$; here, $\Phi_R(E, \alpha_0) = \Phi(s_R(E, \alpha_0))$ is the electrostatic potential when electrons enter or escape from the resonance (which could be treated as equal for bunching and for trapping and could be found from $\mathcal{S}(E_n) = \mathcal{S}(E_{n+1})$). Iteration number n can be substituted by time as $t_{n+1} = t_n + \tau(E_n)$, with $\tau(E_n)$ being the time interval between two resonant interactions (see Ref. [Artemyev et al., 2021c]).

4.3 Long Wave Packets

During a simulation of many electrons interacting with wave-packets of a given frequency, N_c and β, the value of h remains fixed throughout the resonant interaction, and the resultant energy change can be obtained from a probability distribution of ΔE for the fixed h. We can therefore use a ΔE lookup table for the given fixed h of an electron of an initial pitch angle and associated resonance energy. The full range of initial equatorial pitch angles (30° to approximately 80° at the minimum of the magnetic field magnitude) will map to a range of resonance energies around $220 - 280$eV and result in a 2-D probability distribution quantifying the results of the interaction. Figure 4.5 shows probability distributions $\mathcal{P}(\Delta E, E)$ for a fixed h and long wave-packets ($\beta = 100$, $N_c \to \infty$). There is a clear dependence of ΔE-distribution on initial energy, E_0. For small E_0, the distribution of energy changes shows two distinct populations: a small number of electrons with very large $\Delta E > 0$ are electrons accelerated via phase trapping, whereas the main electron population has small $\Delta E < 0$ due to phase bunching. With the increase of the initial energy, E_0, the trapping acceleration becomes less effective and the trapped population moves closer to $\Delta E \sim 0$. This

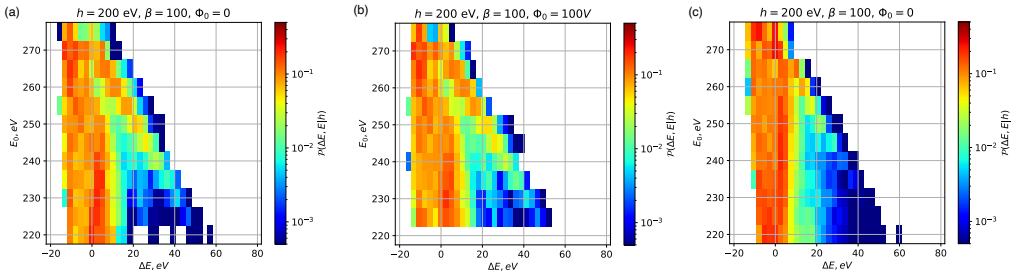

Figure 4.5: Examples of $\mathcal{P}(\Delta E, E_0)$ distributions for the bow shock model with $\Phi_0 = 0$ (a), for the bow shock model with $\Phi_0 = 100$V (b), for the foreshock model (c); in all cases, $N_c \to \infty$ and $\beta = 100$. The main difference between (a) and (b) is that for $\Phi_0 = 100$V many electrons with resonant energies ≤ 225eV cross the bow shock and do not resonate with waves in the upstream region.

is caused by the value of the resonance energy: for fixed h, smaller E_0 means smaller α_0 and larger s for the resonant interactions where electrons will be trapped. As all trapped electrons escape from the resonance at $s \sim 0$, which corresponds to minimum B_0, the duration of electron trapping increases with larger values of s (see Refs. [Shklyar and Matsumoto, 2009, Omura et al., 2015, Artemyev et al., 2015] for a discussion of trapped electron acceleration in an inhomogeneous magnetic field). This leads to longer trapping times and more significant acceleration. Therefore, for long, coherent wave-packets (large β, large N_c) the probability distribution of energy changes, $\mathcal{P}(\Delta E, E)$, depends on two parameters (E, h). To describe electron dynamics, we need to determine the probability distribution in 3D space of $(\Delta E, E_0, h)$. This can be done analytically because ΔE can be determined from analysis of the Hamiltonian equation (4.1) with the wave term included [Vainchtein et al., 2018, Artemyev et al., 2020], and we will provide such a solution using mapping technique.

Figure 4.6 depicts several examples of electron trajectories calculated by direct integration of the Hamiltonian equation (4.1) and by evaluation of the map (4.16). For numerical integration of Hamiltonian equations we use the Runge-Kutta method of 4th order and random initial electron phases, ζ. For mapping evaluation we use uniformly distributed

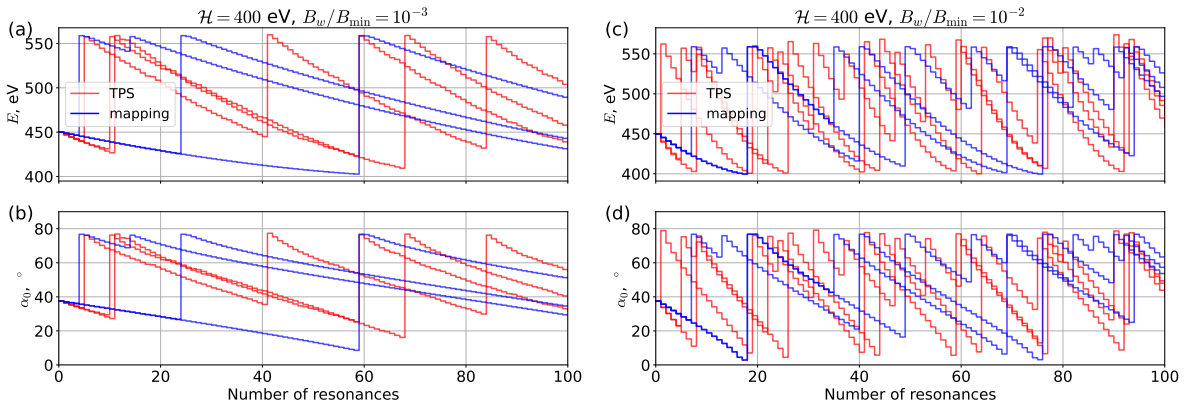

Figure 4.6: Test particle (TP) trajectories obtained by numerical integration approach for two wave amplitudes (panels a,b and c,d respectively), in comparison with trajectories obtained from the mapping technique (4.16) and conservation of $h = E - \omega\mu = const$. The electron energy and pitch-angle at the minimum magnetic field are plotted as a function of the number of resonant interactions, n.

$\xi \in [0, 1]$ and $\langle \Delta E \rangle$ determined by $\mathcal{S}(E)$ profiles. We use the magnetic field model of the foreshock transient to show multiple resonant interactions, and we converted time to the number of resonant interactions n. Although the trajectories of electrons with energy E_n are not identical between the results from the test particle approach and the mapping technique (the difference is due to the random ξ), these two approaches show statistically similar results: electron energy often decreases due to the phase bunching (small negative jumps) and more rarely increases due to the phase trapping (large jumps). Note the energy change in the resonance (due to the phase bunching and phase trapping) depends on the pre-resonance energy, pitch-angle, and this makes each energy change different. The phase trapping and phase bunching can be clearly distinguished. In the case of electrons resonating with field-aligned whistler-mode waves, phase trapping should consistently lead to an increase in energy. (see, e.g., Refs. [Albert et al., 2013, Furuya et al., 2008, Vainchtein et al., 2018]).

4.4 Short Wave Packets

4.4.1 Probabilistic Function of ΔE

Although it is possible to obtain an analytical model for resonant interactions between long wave packets and electrons, such long wave packets are rarely observed. In contrast, the majority of observations are of short wave packets (see Figure 4.1 and Ref. [Shi et al., 2023b]). For these, the efficiency of trapping acceleration varies from one interaction to another, and the role of initial conditions becomes much less important. To illustrate this, we calculate the $\mathcal{P}(\Delta E, E)$ distribution for fixed h and small β, N_c. Figure 4.7 shows that in the short wave-packet limit, the ΔE -distribution is mainly distributed within 20eV of $\Delta E = 0$, with no significant probability of large positive values of ΔE. This implies that the energy gained by trapped electrons decreases(due to the shorter time that electrons spend in the trapping acceleration, see, e.g., Refs [Tao et al., 2013, Zhang et al., 2018b, Mourenas et al., 2018]), while the number of trapped electrons increases (due to large gradient of the wave amplitude at the edge of wave-packet, see, e.g., Ref. [Bortnik et al., 2008, Artemyev et al., 2019c, An et al., 2022]). Such a ΔE-distribution can be characterized by two parameters, $\langle \Delta E \rangle$ and $\langle (\Delta E)^2 \rangle$, i.e., the wave-particle interaction is diffusive. However, this diffusion, $\langle (\Delta E)^2 \rangle \propto B_w^\kappa$ with $\kappa \sim 1$, caused by almost monochromatic intense waves is quite different from the quasi-linear diffusion with $\langle (\Delta E)^2 \rangle \propto B_w^2$ (see the theoretical model for $\langle (\Delta E)^2 \rangle$ in Ref. [Frantsuzov et al., 2023]). In addition to the symmetric distribution of ΔE, short wave-packets also have another important effect. As depicted in Figure 4.7, $\mathcal{P}(\Delta E, E)$ now exhibits weak dependence on E for fixed h. Therefore, instead of a 2D $\mathcal{P}(\Delta E, E)$, we can use a 1D distribution, $\bar{\mathcal{P}}(\Delta E) = \langle \mathcal{P}(\Delta E, E) \rangle_E$, to describe the interaction around the specific resonance energy E, for a fixed h.

Figure 4.7 shows that for systems with short wave packets, we may use a 1D $\bar{\mathcal{P}}(\Delta E)$ distribution. This distribution is equivalent to the cumulative probability distribution $\mathcal{C}(\Delta E) = \int_{-\infty}^{\Delta E} \bar{\mathcal{P}}(x) dx$, which can be used for tracing the electron resonance energy change: given a

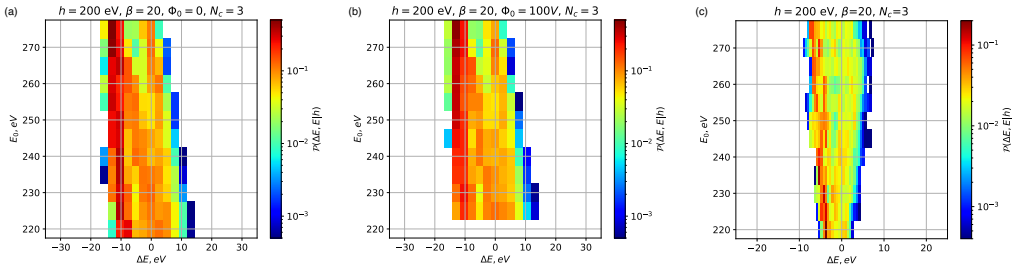

Figure 4.7: Examples of $\mathcal{P}(\Delta E, E)$ distributions for the bow shock model with $\Phi_0 = 0$ (a), for the bow shock model with $\Phi_0 = 100$V (b), for the foreshock model (c); $N_c = 10$ and $\beta = 20$. The main difference between (a) and (b) is that for $\Phi_0 = 100$V a considerable number of electrons with resonant energies ≤ 225eV cross the bow shock and do not resonate with waves in the upstream region.

random number $\xi_n \in [0, 1]$, one can find the corresponding ΔE using $\mathcal{C}(\Delta E) = \xi_n$ distribution. The energy change for each interaction is $E_{n+1} = E_n + \Delta E\,(\xi_n)$, where n is the iteration number (number of resonant interactions). Figure 4.8(a) shows $\mathcal{C}(\Delta E)$ for $\bar{\mathcal{P}}(\Delta E) = \langle \mathcal{P}(\Delta E, E) \rangle_E$ from Figure 4.7(c), whereas Figure 4.8(b) shows several trajectories E_n evaluated with this probabilistic approach. For comparison, we also plot E_n trajectories (Figure 4.8(c)) obtained from the numerical integration of original Hamiltonian equations with the system parameters in the caption of Figure 4.7. Figures 4.8(b,c) demonstrate that this $\mathcal{C}$-based probabilistic approach and the numerical integration approach provide electron trajectories with quite similar elements: rare positive energy jumps due to phase trapping and regular energy drift to smaller values due to phase bunching. Note that for fixed wave frequency the wave-particle resonant interaction occurs with the conservation of $h = E - \mu\omega$ (e.g., Ref. [Shklyar and Matsumoto, 2009]). This conservation law allows tracing of electron pitch-angle for changing energy: $\sin^2 \alpha(s) = (1 - h/E)\Omega(s)/\omega$. This relation shows that electron pitch-angle increases for phase trapping (energy increase) and decreases for phase bunching (energy decrease).

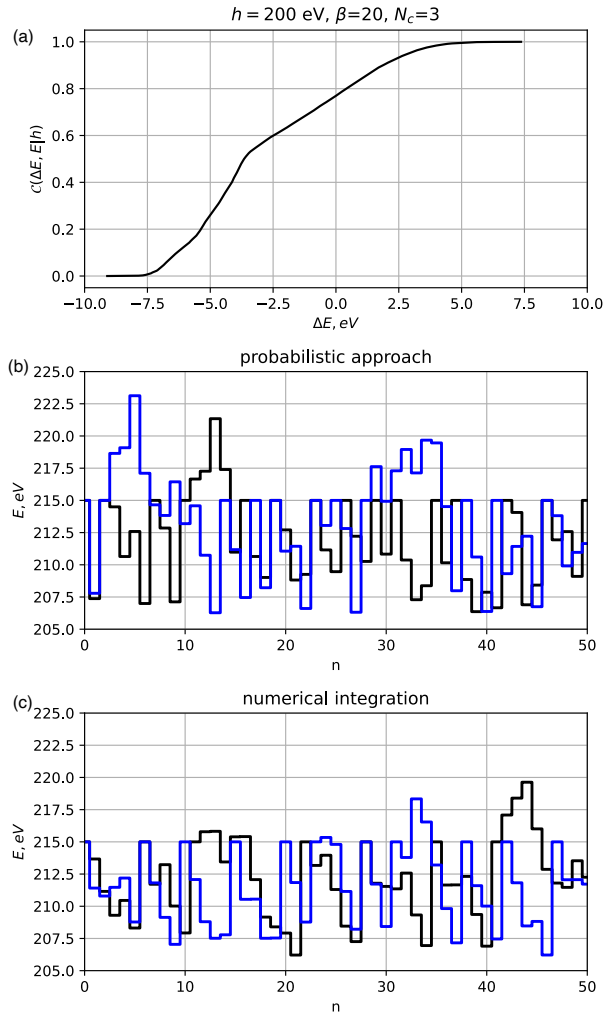

Figure 4.8: Panel (a) shows the cumulative probability distribution function $\mathcal{C}(\Delta E)$ for $\bar{\mathcal{P}}(\Delta E)$ from Figure 4.7(c). Panels (b,c) shows electron energy as a function of the number of resonant interactions n (two interactions per bounce period) for several electron trajectories evaluated with the probabilistic approach (b) and with numerical integration of original Hamiltonian equations (c). The system configuration and parameters are the same as in Figure 4.7(c).

4.4.2 Mapping Technique for Short Wave Packets

Short wave-packets (or as a train of such short packets) can significantly change the properties of nonlinear resonant interactions, i.e., the efficiency of phase trapping [An et al., 2022, Gan et al., 2022, Allanson et al., 2021]. In the first-order cyclotron resonant interaction, electrons move in the opposite direction to the whistler-mode waves, and thus the packet size controls the time-scale of the electron motion in the trapping regime [Tao et al., 2013, Zhang et al., 2018b, Mourenas et al., 2018]. However, the probability of trapping depends on $d\mathcal{S}/dE \propto dB_w/ds$ gradient [Neishtadt, 1975, Neishtadt, 2014], which is very large around the wave-packet edges; this can significantly increase the number of trapped particles [Bortnik et al., 2008, Artemyev et al., 2012, Frantsuzov et al., 2023]. Moreover, for all resonance coordinates (i.e., independent of the background magnetic field and plasma gradients), electrons can interact with the wave-packet edge and thus be trapped. Although all these effects seem to complicate the description of wave-particle nonlinear interactions, they also randomize the interaction process and reduce the importance of specific shapes of the $\mathcal{S}(E)$ profile. For sufficiently short wave-packets, $\mathcal{S}(E)$ can be approximated by $\mathcal{S}/2\pi = \omega^{-1}C \cdot \sqrt{\varepsilon} \cdot [1-(E/\delta E)^2]^{5/4}$, where $\varepsilon = \max B_w/B_0$, δE is the resonance energy range for which $\mathcal{S} \neq 0$, and $C \sim 1$ is a numerical factor of the order of one (see derivations of this approximation in Ref. [Artemyev et al., 2019b] and in Appendix of Ref. [Mourenas et al., 2018]). Note that we have introduced the normalization factor ω^{-1} for the $\mathcal{S}$ function, and thus C has a dimension of energy. Interactions with small wave-packets mean that at each interaction we shall use $\mathcal{S}_n/2\pi = \omega^{-1}C \cdot \sqrt{\varepsilon} \cdot [1-((E-E_n^*)/\delta E)^2]^{5/4}$, with E_n^* determining the location of the wave-packet relative to the electron in resonance. For fixed h, the resonance energy E determines the resonant coordinate s, and thus the relative location of electrons and wave-packets can be modeled by parameter E_n^* in the $\mathcal{S}_n$ equation. If $E_n \notin [E_n^* - \delta E, E_n^* + \delta E]$, the electron in question will not meet the wave-packet in resonance (see derivations of this approximation in Ref. [Artemyev et al., 2021b]).

To model electron resonant interactions with wave-packets, we numerically integrate the

Hamiltonian equations for system (4.1) with $B_w \to B_w f(\phi)$, where $f(\phi) = \exp\left(-5\cos^2(\phi/2\pi\beta)\right)$ is the function modulating the wave field and separating it into wave-packets with the duration of $\sim \beta$ for each packet [Tsai et al., 2022]. There are two scenarios of electron resonant interactions with the wave-packet train (several wave-packets). The first scenario assumes that the entire train has been generated within the same wave source region that does not change significantly during the wave generation, and thus the phase ϕ is coherent along the entire train. In this case, electrons may be retrapped by the next wave-packet after escaping from resonance with the previous wave-packet. This situation is especially common for short wave-packets, i.e., with $\beta < 10$, when the distance between two consecutively moving wave-packets is small. Such multi-trapping electron acceleration is quite effective [Hiraga and Omura, 2020, Foster et al., 2021] and does not principally differ from the electron trapping into an infinitely long wave-packet (except that the trapping probability is higher due to strong wave field gradients at the leading edges of wave-packets). Figure 4.9(a) shows the distribution of the electron energy change, ΔE, due to resonant interactions with phase-coherent wave-packet trains. The spreading of the distribution ($\Delta E > 0$) is because of the randomization of energy gain of the trapped electrons. However, keeping the coherent phase for a long wave-packet train may not be always realistic. Thus, we also use the second scenario assuming that wave-modulation (separation of wave field into the wave-packets) destroys the wave phase coherence, and leads to ϕ jumps between wave-packets (see examples of in Refs. [Santolík et al., 2014, Zhang et al., 2020, Nunn et al., 2021]). Such jumps of ϕ prevent the electrons from being trapped into multiple wave-packets [Zhang et al., 2020]. To model this effect, we introduce a coherence length measured in wave-packet duration, N_c: all electrons will escape from resonance after interaction with N_c packets (some electrons may escape sooner, but no electrons are allowed to stay in resonance longer than this). Figure 4.9(b) shows the distribution of the electron energy change, ΔE, due to resonant interactions with a wave-packet train having $N_c = 2$. Comparison of Panels (a) and (b) demonstrates the effect of wave phase jumps: even for $\beta = 50$, the range of $\Delta E > 0$ due to trapping

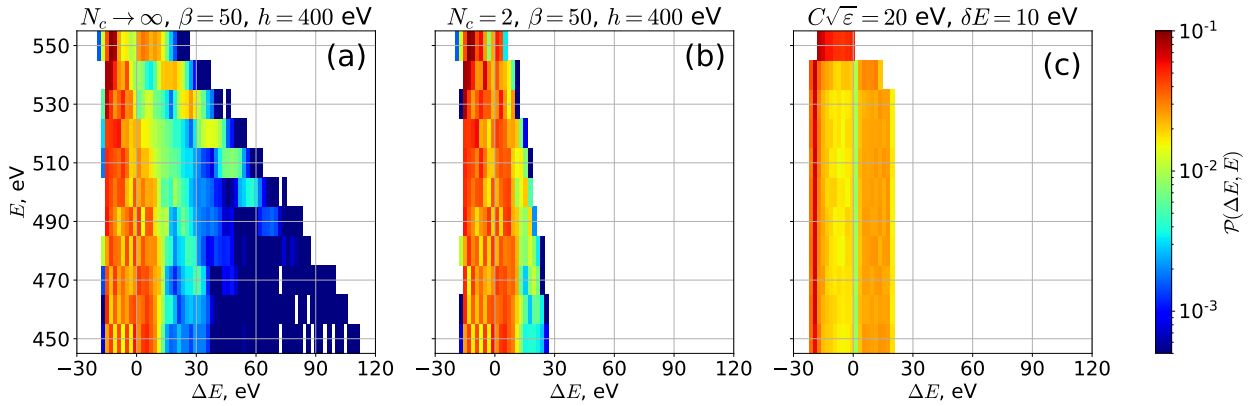

Figure 4.9: ΔE-distributions for a single resonant interaction with (a) the coherent wave-packet train, (b) wave-packet train with $N_c = 2$. Panel (c) shows ΔE-distribution obtained from the mapping technique. Parameters of map $\mathcal{S}/2\pi = \omega^{-1}C \cdot \sqrt{\varepsilon} \cdot [1 - ((E - E_n^*)/\delta E)^2]^{5/4}$ are given on the panel (c), top; see text for details.

significantly shrinks for $N_c = 2$, in comparison with $N_c \to \infty$. Note that we use a long wave packet to better illustrate the effect of a finite N_c.

We compare numerically derived ΔE-distributions with the results obtained from electron trajectories integrated using the mapping technique for different δE parameters. Figure 4.9(c) shows that the mapping with $\mathcal{S}_n/2\pi = \omega^{-1}C \cdot \sqrt{\varepsilon} \cdot [1 - ((E - E_n^*)/\delta E)^2]^{5/4}$ can reproduce the main properties of the numerically obtained ΔE-distributions shown in Figure **??**(b): a significant population of electrons do not meet the wave-packet at resonance (a finite electron population around $\Delta E \sim 0$), whereas energy change for resonant electrons weakly depends on the initial energy. Therefore, we propose utilizing a combination of $\mathcal{S}_n/2\pi = \omega^{-1}C \cdot \sqrt{\varepsilon} \cdot [1 - ((E - E_n^*)/\delta E)^2]^{5/4}$ functions in the mapping technique to accurately replicate any particular ΔE-distribution obtained from the numerical integration of the electron resonant interactions with wave-packet trains.

4.4.3 Synthetic Map

In this subsection, we further construct the mapping function as a sum of $\mathcal{S}(E)$ functions. Such a synthetic map allows us to describe the probability distribution $\mathcal{P}$ in $(\Delta E, E)$ space. We adopt the distribution of wave-packet sizes, β, as derived from observations (see Figure 4.1(a)): $P_\beta = C_0\beta^{-1.67}$ for $\beta \in [2, 100]$ and $C_0 = \left(\int P_\beta(\beta)d\beta\right)^{-1}$. Next, we numerically integrate a large ensemble of electron trajectories, where each electron undergoes resonance with wave-packets that have randomly chosen β values.

To construct such a synthetic map (a sum of many maps with different $\mathcal{S}(E)$), we first determine how $\mathcal{S}(E)$ parameters (i.e., δE, C, E_n^* distributions) control the resulting ΔE-distribution. Figure 4.10(a) depicts a schematic of the role of δE and C in determining the ΔE-distribution characteristics. The magnitude of $\mathcal{S}(E)$ controls the ΔE range of bunching with $\min \Delta E = -\max \omega\mathcal{S}(E)/2\pi$, whereas δE controls the ΔE range of trapping with $\max \Delta E = \delta E$. The maximum relative number of trapped particles, Π, is determined by $\max \Pi/\sqrt{\varepsilon} = (C/\delta E) \cdot (5/2^{1/2}3^{3/4}) \approx 1.551 \cdot (C/\delta E)$. The energy ranges of bunching and trapping ΔE depend on the initial electron energy E (see Figure 4.9). As a result, we set $C = C(E)$ and $\delta E = \delta E(E)$. If such dependencies are weak, $|dC/dE| \ll C/\delta E$ and $d\delta E/dE \ll 1$, they will not significantly change the value of Π.

The distribution of wave-packet positions, E_n^*, determines how often electrons will resonate with waves. If E_n^* is uniformly distributed within $E \pm \delta E$, then each map iteration will have an energy change, i.e., electrons will encounter wave-packets each time when crossing the resonance. This describes a system with dense wave-packet trains, where one packet moves right after another. If E_n^* is uniformly distributed within the entire resonance energy range $[E_-, E_+]$ and $\delta E < E_+ - E_-$, then the probability of the particle energy change (the probability to meet a wave-packet in resonance) is $\delta E/(E_+ - E_-)$. For small $\delta E/(E_+ - E_-)$, the resonant interactions are rare, and this describes a system with well-separated individual wave-packets. Figure 4.10(b) shows ΔE-distributions for three different E_n^* distributions:

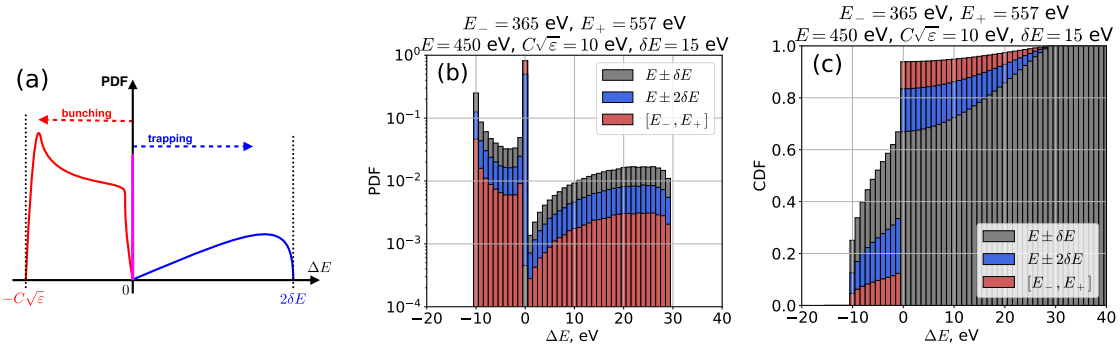

Figure 4.10: The basic principles to construct the synthetic map. The basic principles to construct the synthetic map: (a) a schematic view of δE and C roles in determining the characteristics of ΔE distribution (the resonance energy range is $E \in [E_-, E_+]$ and $\delta E \leq [E_-, E_+]$); (b) three ΔE-distributions for three uniform E_n^* distributions within $E \pm \delta E$ (black), within $[E_-, E_+]$ (red), and within $E \pm 2\delta E$ (blue); (c) cumulative distribution functions for ΔE-distributions from (b).

a smaller probability of resonant interactions means a higher value of probability to have $\Delta E = 0$ (see a peak of $\mathcal{P}$ at $\Delta E = 0$). Furthermore, we evaluate the cumulative distributions for these three probability distributions. Figure 4.10(c) shows that for particles with $E_n^* \in [E_-, E_+]$, they frequently do not encounter waves in resonance, resulting in a high probability of a zero ΔE. However, for electrons with $E_n^* \in [E - \delta E, E + \delta E]$, each resonant interaction causes a change in their energies, leading to a relatively high probability of a significant ΔE.

Figure 4.11(a,b) shows the probability distribution functions $\mathcal{P}(\Delta E, E)$ for a single resonant interaction with randomly chosen β, $N_c = 5$ and $N_c = 10$. For $N_c = 10$, the distribution $\mathcal{P}(\Delta E, E)$ has a slightly higher probability for large $\Delta E > 0$ at low energies ($E \leq 490$eV), but the difference between $N_c = 5$ and $N_c = 10$ is significantly reduced due to a wide β distribution dominated by small β (see Figure 4.1). For $N_c = 5$, the distribution $\mathcal{P}(\Delta E, E)$ is almost independent of E. In the first paper, we have examined the limit of small N_c when the probability distribution function $\mathcal{P}(\Delta E, E)$ can be reduced to 1D $\mathcal{P}(\Delta E)$, without

significant dependence on E.

We fit two $\mathcal{P}(\Delta E, E)$ distributions from Figure 4.11(a,b) by $G(\Delta E, E)$ functions derived from the synthetic map consisting of a sum ($\sum_k \mathcal{S}_k P_{\delta E}(\delta E_k)$) of

$$\mathcal{S}_k/2\pi = \omega^{-1} C_k \cdot \sqrt{\varepsilon} \cdot \left(1 - ((E - E_n^*)/\delta E_k)^2\right)^{5/4}$$

We use $P_{\delta E} \propto (\delta E)^{-1.67}$, which is based on the P_β distribution and the $\delta E \propto \beta$ relation (see schematic in Figure 4.10 and Ref. [Artemyev et al., 2021b]). Figure 4.11(c,d) shows two $G(\Delta E, E)$ distributions constructed with four $\mathcal{S}_k$ functions having different C_k and $E_n^* = E \pm \delta E_k$ (parameters are in the figure caption). These synthetic $G(\Delta E, E)$ distributions reproduce the main details of the numerically obtained $\mathcal{P}(\Delta E, E)$ distributions. Importantly, the fitting procedure for $G(\Delta E, E)$ does not have a unique solution, but should approach the distribution of energy changes ΔE that fully describes the dynamics of electron resonant interactions. Thus, we need to further test whether the constructed $G(\Delta E, E)$ provides a correct long-term evolution of the electron ensemble.

4.5 Verification of Two Methods

4.5.1 Verification of Probabilistic Approach

To verify the probabilistic approach, we use the $\mathcal{C}$ function to evaluate the energy changes of 10^5 trajectories for 20 resonant interactions. We use the initial distribution function $F(E) \sim \exp(-E/50\text{eV})$ to set the initial phase space density $F(E)$ and then trace its evolution in energy. Note that this is a 1D distribution for a fixed h; to trace the dynamics of a 2D (energy, pitch-angle) distribution, numerous h should be used [Vainchtein et al., 2018]. To compare and validate the results obtained from the probabilistic approach, we use 10^4 numerically integrated electron trajectories with the same initial distribution $F(E)$. Figure 4.12 shows $F_m(E)$ for the probabilistic approach and $F_t(E)$ for test particle simulations with different n. Note that although we use iteration numbers instead of time, the same

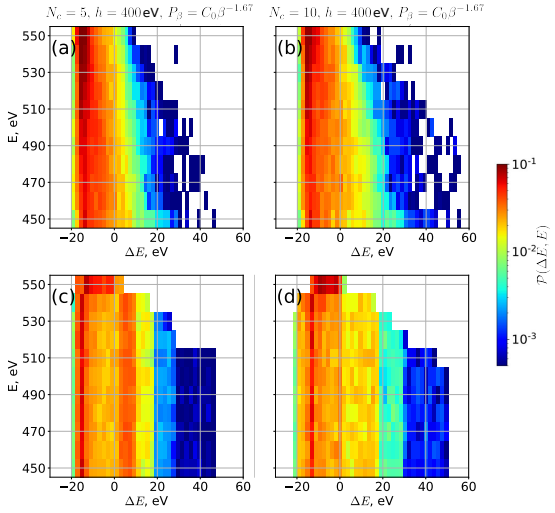

Figure 4.11: Panels (a,b) show two distributions $\mathcal{P}(\Delta E, E)$ for the bow shock magnetic field model and $N_c = 5$(a), $N_c = 10$(b). For each resonant interaction, we use a random value of β determined by the probability distribution function $P_\beta = C_0 \cdot \beta^{-1.67}$ for $\beta \in [2, 100]$ and $C_0 = \left(\int P(\beta) d\beta\right)^{-1}$ and the same wave amplitude $B_w / \min B_0 = 10^{-2}$. Panels (c,d) show two distributions $G(\Delta E, E)$ obtained from the mapping of a sum of $\mathcal{S}_k$ with $P_{\delta E}(\delta E_k) = a_k \cdot (\delta E)^{-1.67}$. For panel (c) $\delta E_k = \{1, 9, 15, 25\}$, $\sqrt{\varepsilon} C_k = \{9, 14, 18, 22\}$, $a_k = \{6.3, 17.7, 5.7, 9.4\}$, and for panel (d) $\delta E_k = \{5, 9, 14, 23\}$, $\sqrt{\varepsilon} C_k = \{17, 15, 22, 19\}$, $a_k = \{0.1, 22.0, 22.0, 22.0\}$.

approach can be used for the time iteration, $t_{n+1} = t_n + \tau(E_n)/2$, with $\tau(E_n)$ being the bounce period of electrons, i.e., $\tau(E_n)/2$ is the time between two resonant interactions. The scattering caused by short wave-packets mostly results in an energy decrease (which also means the pitch-angle decrease), and $F_t(E)$, $F_m(E)$ grow at smaller energies. The electron distribution obtained by test particle simulations evolves very similar to that obtained from the probability approach, i.e., the probability approach works well.

4.5.2 Verification of Mapping Technique

Figure 4.13(a,c) repeats the results from Figure 4.11(a,b) for a single resonant interaction with wave-packets having β distributions of $P_\beta \propto \beta^{-1.67}$. However, in this case, the trajectories are traced in the foreshock transient magnetic field model. For $N_c \to \infty$, the shortness of wave-packets can be compensated by the effect of multiple trapping, and the corresponding probability distribution function $\mathcal{P}(\Delta E, E)$ contains a finite probability of large $\Delta E > 0$ for small E. Despite that the ΔE-distribution depends on E, the synthetic mapping technique reproduces the main features of the 2D distribution $\mathcal{P}(\Delta E, E)$ (compare Figure 4.13(a) and Figure 4.13(b)).

For $N_c = 3$, there is almost no effect of multiple trappings, and the corresponding probability distribution function $\mathcal{P}(\Delta E, E)$ does not contain large $\Delta E > 0$ jumps. Moreover, due to the dominant role of small β in $P_\beta \propto \beta^{-1.67}$ distribution, the energy change ΔE due to resonant interactions only weakly depends on the initial energy E (similar to the bow shock system; compare Figure 4.13(c) and Figure 4.11(a)). Although the synthetic map can describe such a 1D distribution of $\mathcal{P}(\Delta E)$ (compare Figure 4.13(c) and Figure 4.13(d)), we note that a simpler approach for such E-independent systems is the proposed probabilistic approach.

We next verify the suggested approach for constructing synthetic maps in the foreshock transient magnetic field model. This assumes multiple resonant interactions for each electron, and thus includes the long-term dynamics of the electron energy distribution. In the test

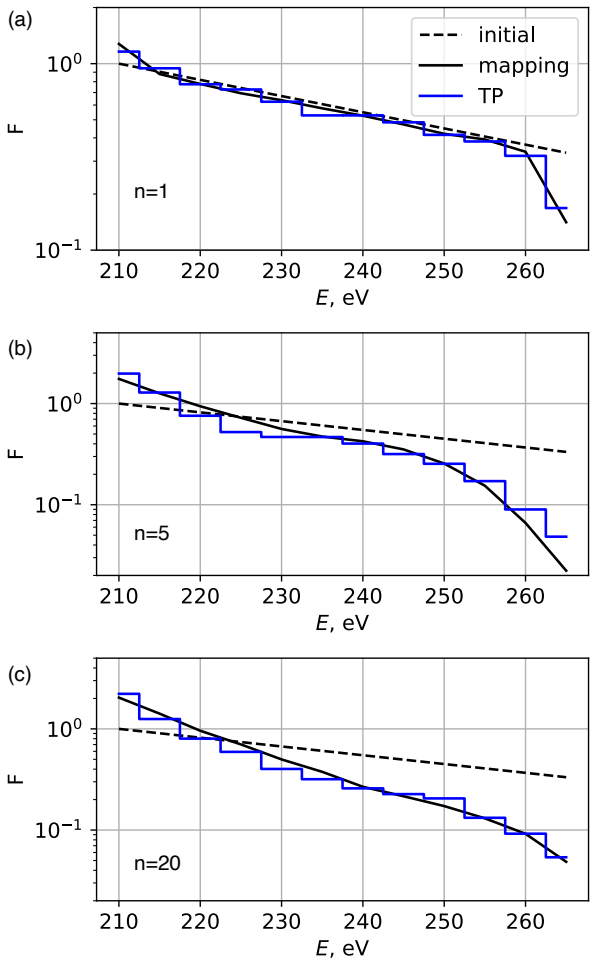

Figure 4.12: Evolution of electron distribution function evaluated by numerical integration of Hamiltonian equations (4.1) and by the probabilistic approach using the cumulative distribution $\mathcal{C}$ of Figure 4.8(a). Three panels show results for $n = 1$(a), $n = 5$(b), and $n = 20$(c); the dashed curve in each panel shows the normalized initial distribution, $F(E) \sim \exp(-E/50\text{eV})$; blue curves show results of test particle simulations, black curves show results of the probabilistic approach.

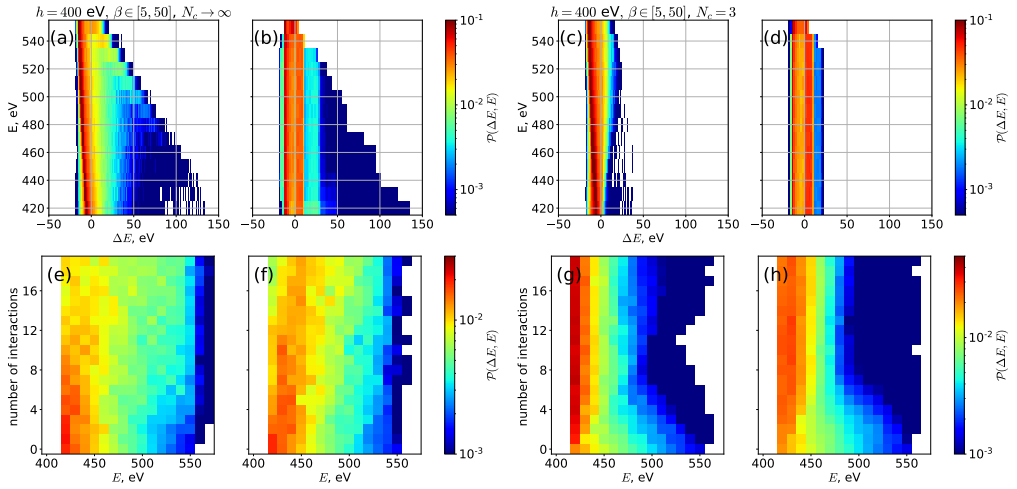

Figure 4.13: Panels (a, b) show the probability distribution function $\mathcal{P}(\Delta E, E)$ for $N_c \to \infty$ and the corresponding synthetic map, starting from the initial distribution of $\sim \exp(-E/50\text{ eV})$; panels (c, d) show the same but for $N_c = 3$. Parameters for (b): $\delta E_k = \{67, 47, 30, 26, 18, 15, 14, 5\}$, $\sqrt{\varepsilon} C_k = \{10, 16, 20, 16, 14, 8, 11, 12\}$, $a_k = \{3.7, 7.8, 2.9, 7.7, 2.5, 6.1, 10.3, 10.7\}$; for (d): $\delta E_k = \{11, 10, 5, 4\}$, $\sqrt{\varepsilon} C_k = \{21, 17, 14, 12\}$, $a_k = \{0.4, 3.1, 4.9, 6.0\}$. Panels (e, f) show the evolution of the energy distribution with $N_c \to \infty$ and the corresponding evolution of distribution with the use of the synthetic map from panel (b); panels (g, h) show the same but for $N_c = 3$ with the synthetic map from panel (d).

particle simulation, we numerically integrate 10^4 electron trajectories with the same h and initial energy distributions with energy falloff $\sim \exp(-E/50eV)$. Trajectories are trapped in the system with an ensemble of wave-packets described by P_β, but for half of the bounce period each electron only resonates with one wave-packet (new wave characteristics for the next half of the bounce period are set when an electron crosses the B_0 minimum). Electrons that undergo phase bunching tend to drift towards smaller energy and pitch angles. This drift may cause them to enter the small pitch-angle range, where the mapping technique should be modified due to the effects of anomalous trapping [Kitahara and Katoh, 2019]. Moreover, such electrons should escape the system because their mirror points are outside of the foreshock transient region (magnetic field magnitude in the mirror points exceeds $\sim 10\times$ of the minimum magnetic field). Thus, we exclude electrons reaching the small pitch-angle boundary, $\alpha_0 \approx 20°$. To keep the same number of particles during the simulation, we substitute each escaping electron with a new one (e.g., trapped into the foreshock transient from the solar wind flow) of identical initial energy as the lost electron. Modeling them this way is equivalent to including a large trapping probability for small energy electrons, to reflect them from the small-energy/small pitch-angle boundary (see Refs. [Kitahara and Katoh, 2019, Albert et al., 2021, Artemyev et al., 2021a] for discussions of this effect for electron scattering by whistler-mode waves in the radiation belts).

Figures 4.13(e,f) and (g,h) compare the results of test particle simulations and the mapping technique using the synthetic maps shown in Figure 4.13(b) and (d), respectively. For a large N_c, we see a significant acceleration of electrons, whereas, for small N_c, electrons mostly drift to small energies. Due to the conservation of $E-\omega\mu$ invariant [Shklyar and Matsumoto, 2009], small energies mean small pitch-angles ($\Delta\alpha \propto \Delta E$, and the energy decrease due to the phase bunching corresponds to the pitch-angle decrease; see Figure 4.6). Therefore, a small-energy electron population in Figure 4.13 is associated with small pitch-angles, i.e. a field-aligned electron population. The drift of electrons to small energies/pitch-angles for small N_c is clearly evident in the results obtained from the test particle simulations (pan-

els (e, g)) as well as in the mapping technique results (panels (f, h)). Thus, the presented comparison validates the proposed mapping technique and synthetic map.

4.6 Summary

In this chapter, we theoretically modeled resonant interactions between solar wind electrons and intense short wave-packets of whistler-mode waves. We proposed and verified a probabilistic approach based on $\mathcal{P}(\Delta E)$ probability distributions and a mapping technique based on the synthetic map to describe electron dynamics. The probabilistic approach can be used to model the long-term dynamics of electron distributions in a system with multiple nonlinear resonant interactions with short wave-packets. The mapping technique is used to describe the rare but effective electron acceleration by long wave-packets. These two approaches can reproduce the main statistical properties of wave-particle interactions while keeping all important information without requiring extensive computational power.

These approaches can be useful for modeling the electron resonant interaction effects in large-scale simulations, where the long-term electron dynamics is dominated by adiabatic heating and transport, whereas wave-particle resonant effects should be responsible for scattering and relaxation of the electron anisotropy. In Chapter 5, we combine the wave characteristics described in the previous chapter and the method shown in this chapter to build a compound model for electron acceleration.

CHAPTER 5

Compound Acceleration of Electrons in Earth Foreshock

5.1 Introduction

In previous chapters, we discussed the characteristics of whistler waves, confirmed the effectiveness of interactions between electrons and whistler-mode waves, and developed theoretical approaches to simulate the long-term behavior of electrons. This chapter combines wave-particle interactions, adiabatic acceleration, and shock drift acceleration into a comprehensive acceleration model using probabilistic methods. This compound model can successfully replicate the observed electron energy spectrum in Earth's foreshock region, enhancing our understanding of the shock acceleration process.

In collisionless space plasmas, shock waves heat and energize charged particles [Jones and Ellison, 1991, Giacalone, 2005, Perri et al., 2022]. Astrophysical shocks are believed to generate some of the most energetic particles in the universe [Koyama et al., 1995, Aharonian et al., 2004, Masters et al., 2013]. A long-lasting mystery in shock acceleration is how to accelerate background thermal particles up to superthermal or even mildly relativistic energies (so-called Fermi's injection problem). In-situ spacecraft measurements at interplanetary shocks [Dresing et al., 2016] and at bow shocks of the inner [Wilson et al., 2016a] and outer planets [Masters et al., 2013] of the heliosphere are the most natural way to test and explore this particle energization. Such measurements are very copious and detailed at Earth's bow shock and its foreshock, the region upstream of Earth's bow shock which contains many

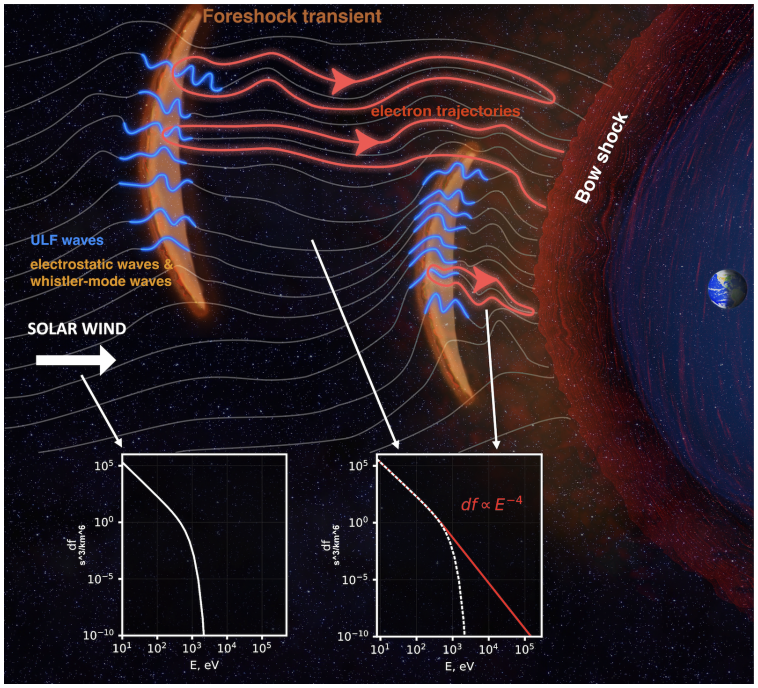

Figure 5.1: Schematic of electron interaction with the bow shock and high-amplitude magnetic field transients in the foreshock region. An electron can traverse or bounce at these strong field regions. Between successive bounces, electrons are energized and scattered in pitch angle by electrostatic waves and whistler-mode waves. Electron shock drift acceleration and adiabatic betatron and Fermi acceleration due to foreshock transient motion toward the bow shock supplement the energization by waves. The original electron phase space density (df) in the solar wind decreases quickly as energy increases above $\sim$ 100eV. After acceleration, the electron phase space density distribution has a power-law tail up to hundreds of keV, as shown in the red line.

solitary, large-scale transient structures [Turner et al., 2013]. This region has been found to host acceleration of electrons by more than four orders of magnitude, from solar wind energies of $\leq$10eV to near-relativistic energies of hundreds of keV [Wilson et al., 2016a, Liu et al., 2019, Amano et al., 2020]. This acceleration is surprising, given the relatively limited scale-size of the foreshock, and has been an outstanding unsolved issue for decades. Investigating the mechanisms responsible for the formation of such energetic electrons upstream of the collisionless shock will provide unique information for models and theories of shock acceleration in various space plasma systems [Amano and Hoshino, 2022].

Classic shock-drift acceleration (SDA) alone is insufficient to accelerate solar wind electrons to hundreds of keV without effective electron trapping around the bow shock [Webb et al., 1983, Treumann, 2009]. Stochastic shock drift acceleration (SSDA) [Amano et al., 2020] overcomes this limitation by assuming pitch-angle (angle between velocity and magnetic field direction) scattering of electrons at turbulent wave field sites on either side of the shock. This allows electrons that bounce between those sites to spend sufficient time near the shock to be shock-drift accelerated to high energies [Amano et al., 2020, Amano and Hoshino, 2022]. SSDA's efficiency depends on the effectiveness of pitch-angle scattering by electron resonant interactions with electromagnetic and electrostatic waves [Katou and Amano, 2019, Vasko et al., 2022].

There is no single wave mode that can pitch-angle scatter electrons efficiently over the wide energy range from 10eV to hundreds of keV. However, multiple wave modes exist in the bow shock and foreshock, such as: electrostatic waves consisting of a mixture of ion-acoustic waves [Balikhin et al., 2005, Vasko et al., 2022], ion and electron phase space holes [Kamaletdinov et al., 2022]; electromagnetic high-frequency whistler-mode waves [Oka et al., 2017, Shi et al., 2023a]; low-frequency whistler-mode (magnetosonic) waves [Krauss-Varban et al., 1994, Wilson et al., 2012, Lalti et al., 2022b]; and ultra-low frequency magnetic field perturbations [Hobara et al., 2007, Wilson, 2016]. Each wave mode can resonate with electrons in a specific (often quite narrow) energy range but acting together these modes

may cover the entire energy range of interest.

When there is a large Sun-Earth component to the magnetic field in the solar wind, occasional discontinuities transported by the latter interact with the foreshock and cause foreshock transients. These are sites of large magnetic field compressions that can adiabatically reflect or locally heat electrons [Liu et al., 2019]. Moreover, these transients often form new shock waves ahead of the bow shock, contributing to the electron SDA upstream of the parent shock [Zhang et al., 2022]. A subset of electrons in the foreshock environment is subject to scattering and acceleration by many or all these processes, as depicted in Figure 5.1, amounting to a compound, aggregate acceleration. Such acceleration is difficult to study except by using appropriate modeling with realistic assumptions, well-guided by observations.

5.2 Observations

5.2.1 Electron Energy Spectrum

Here we show that the combination of electron resonant scattering by different wave modes, electron adiabatic reflection from large-amplitude foreshock transients, and SDA can collectively account for the formation of observed electron fluxes up to and above $\sim$ 200keV, consistent with observations. Towards this goal, we employ observations of Magnetospheric Multiscale (MMS), Time History of Events and Macroscale Interactions during Substorms (THEMIS), theoretical models of wave-particle resonant interaction with electrostatic and whistler-mode waves, and a probabilistic approach which allows for rapid evolution of electron trajectories in prescribed magnetic fields and wave fields. The MMS data are used to derive the statistical properties of the wave-fields with high spatial resolution around transients, whereas the THEMIS data are used to inform us of the typical spatial structure of the foreshock environment.

To justify our main theoretical assumptions and motivate our choice of model parameters

we present in Figure 5.2 MMS observations of foreshock transients, exhibiting significant electron fluxes in the $\sim$ 200keV range. MMS crosses the quasi-perpendicular bow shock around 00:50 UT. The shock has a normal $[0.99, -0.03, 0.10]$ in geocentric solar ecliptic (GSE) coordinates, at an angle $80° \pm 5°$ to the interplanetary magnetic field. The shock-normal velocity is 650km/s. The bow shock crossing is evident as a clear transition from thermalized ion energy spectra and a strong, highly fluctuating magnetic field intensity downstream, to narrow spectra and a weakly fluctuating field upstream. The foreshock region (in the upstream) is replete with energetic ions ($\geq$ 10keV) coincident with transient magnetic field enhancements. These are typical observations of foreshock transients [Turner et al., 2013, Omidi et al., 2010]. We zoom into one of them, at $\approx$02:15UT: there is a classic transient configuration with two magnetic field boundaries (peaks at 02:15 and 02:16UT in Panel (c)) and core region characterized by weak and fluctuating magnetic field, reflected ions, and strongly scattered solar wind beam (Panel (d)). We focus on the energetic electrons filling the core region (Panel (e)) up to 200keV. The electron phase space density energy-spectrum (Panel (i)) shows a power law $\sim E^{-4}$ tail between $E \sim 1$ keV and 200 keV, in good agreement with previously reported energetic electron events at foreshock transients by THEMIS [Wilson et al., 2016a, Liu et al., 2019]. To gain such high energies the solar wind electrons must be able to interact multiple times with the bow shock. Therefore, there should be some mechanisms providing solar wind electron trapping between the bow shock and its foreshock transients.

5.2.2 Spatial Scale of the Electron Acceleration Region

To estimate the spatial scale of the foreshock region filled by the transient structures and hosting electron acceleration we use the statistics of observations by THEMIS that comprises five (2008-2009) and three (2010-2023) satellites [Angelopoulos, 2008]. We focus on the 2010-2023 period, when THEMIS A, D, and E can near-simultaneously traverse the dayside region, maintaining a spatial separation ranging from hundreds to thousands of km (several

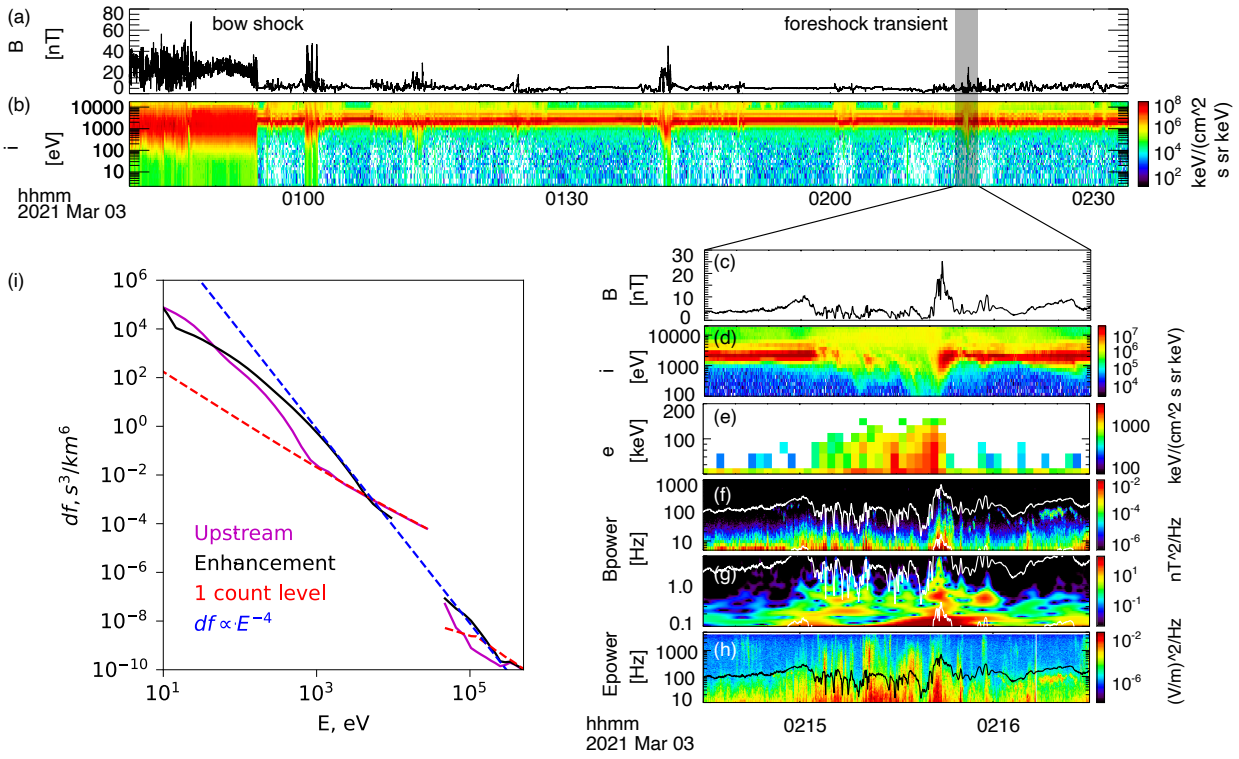

Figure 5.2: Observations of flux enhancement of tens to hundreds of keV electrons at a foreshock transient. Between 00:30 and 02:30 UT, MMS crossed Earth's bow shock and foreshock, where multiple foreshock transients were detected. Panels (a) and (b) show magnetic field strength and ion energy spectra, respectively. Panels (c-h) zoom into a subset of the above interval during a foreshock transient event. From top to bottom these panels show: (c) the magnetic field strength, (d) the ion energy spectrum, (e) the electron energy spectrum for $50 - 200$ keV electrons indicating the presence of relativistic electrons up to 150keV, (f, g) magnetic field power spectra for high and low frequencies, respectively, (h) the high-frequency electric field power spectrum. Panel (i) illustrates the observed electron phase space density (df) at the upstream region outside transients (magenta lines) and at the foreshock transient of panels (c-h) (blue lines). Reliable measurements are limited to data above the 1 count level (dashed red line). Notably, the electron df during the enhancement adheres to a power-law behavior, with df proportional to E^{-4} (dashed blue line).

Earth radii). We use the routinely (always) available magnetic field and plasma moment data provided by the THEMIS fluxgate magnetometer (FGM) [Auster et al., 2008] and ion electrostatic analyzers (iESA) [McFadden et al., 2008], respectively. We assemble a database of events when one of the THEMIS spacecraft crosses the bow shock, and another one observes the foreshock transient, similar to the example in Figure 5.3 (a-f). Using such events we estimate the distance between the upstream foreshock transient structures and the bow shock. This distance serves as the spatial scale of the electron acceleration region in our model, where electrons bounce between the bow shock and the boundary of foreshock transients. To compile statistics, we utilize the THEMIS dataset from 2010-2023, select events akin to the one described above, and impose the constraint that the distance between the two satellites in the GSE-Y direction should be less than 2.5 Earth radii, since we are mostly interested in the spatial scale along solar wind flow. The distribution of the spatial scales in the database is depicted in Figure 5.3(g). Most of the foreshock transients are observed within 4 Earth radii ($\sim$ 25000km) upstream of Earth's bow shock, in agreement with previously published estimates [Chu et al., 2017b]. This spatial scale is used in our model of electron dynamics.

5.3 Model

Trapping can be accomplished by adiabatic reflection or electron pitch-angle scattering as follows: First, the foreshock region is filled with transients with large magnetic field fluctuations [Hobara et al., 2007, Zhang et al., 2022]. The compressional nature of these fluctuations may allow them to adiabatically reflect electrons, trapping them between the bow shock and the ensemble of transients within the foreshock. Second, the foreshock magnetic boundaries host intense electrostatic turbulence [Balikhin et al., 2005, Kamaletdinov et al., 2022, Vasko et al., 2022] (Figure 5.2 (h)), high-frequency whistler mode waves [Oka et al., 2017, Shi et al., 2023a] (Figure 5.2 (f)) , and low-frequency magnetosonic waves [Krauss-Varban et al.,

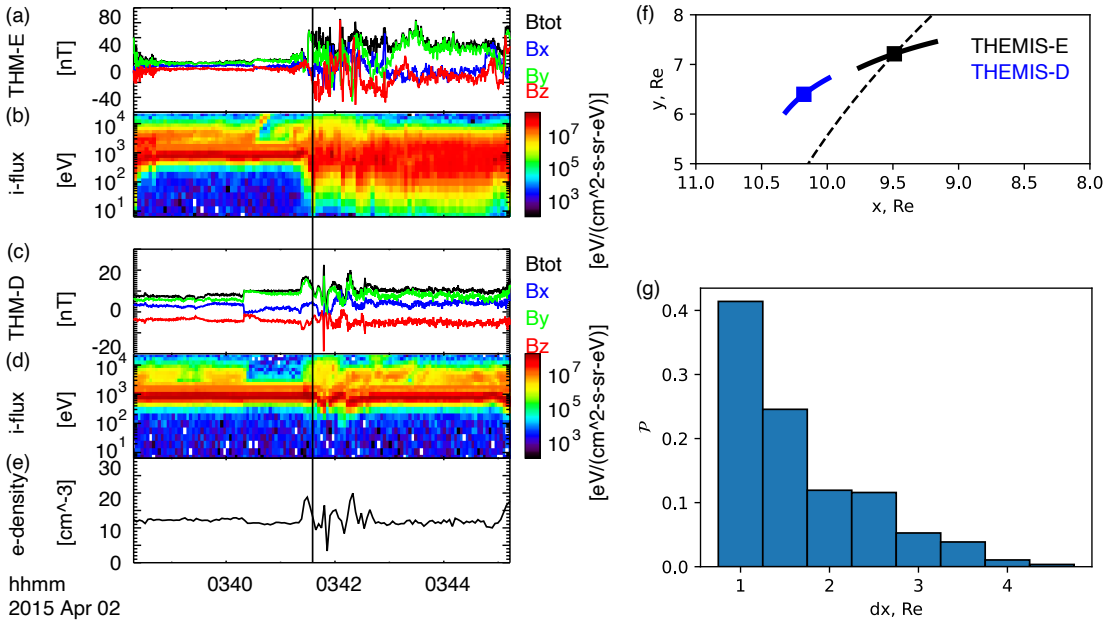

Figure 5.3: Typical multi-satellite observation of a foreshock transient's plasma environment detected by THEMIS. (a-b) THEMIS-E crossing of the bow shock, denoted by the vertical black line. (c-e) concurrent THEMIS-D (nearby THEMIS-E) observation of the foreshock transient, identified by its magnetic field enhancement and electron density perturbation in the upstream region; (f) locations of THEMIS-D and THEMIS-E in the GSE coordinate system, with the dashed black line indicating the position of the bow shock. We have found approximately 100 similar events, involving one THEMIS satellite crossing the bow shock and another being in the upstream region observing foreshock transient perturbations; (g) statistical distribution of the distances between the bow shock and transient structure, offering insights into the spatial scales of the foreshock acceleration region.

1994, Wilson et al., 2012, Lalti et al., 2022b] (Figure 5.2 (g)). These wave modes provide effective pitch-angle scattering for electrons covering a wide energy range. Figure 5.4(a-c) shows typical waveforms of these wave-modes. The efficiency (rate) of electron pitch-angle scattering by these waves is given by the pitch-angle diffusion rate ($D_{\alpha\alpha}$, in rads$^2/s$). The mechanics for calculating the diffusion rates for these waves are well-established [Kennel and Petschek, 1966, Summers, 2005, Kamaletdinov et al., 2022] for a homogeneous or weakly inhomogeneous magnetic field. However, the foreshock region is also filled with large amplitude magnetic field fluctuations which provide strong inhomogeneity. Thus, we averaged the standard rates of pitch-angle diffusion over an ensemble of observed magnetic field fluctuations, using THEMIS statistics (see Methods) to establish the spatial scales of these fluctuations. Figures 5.4(d-f) show such averaged rates: electrostatic turbulence (EST) mostly scatters $<$ 1keV electrons of large and intermediate pitch-angles, high-frequency whistler mode waves (WW) mostly scatter $<$ 10keV electrons with the resonance energy increasing with pitch-angle, and magnetosonic waves (MSW) mostly scatter $>$ 10keV field-aligned electrons. Figure 5.5 confirms that the three wave modes cover five orders of magnitude in energy, from the solar wind electron energy $\sim$ 10eV to near the maximum observed energy of energetic electrons $\sim$ 100keV.

The acceleration mechanism includes electron SDA at the bow shock, and Fermi and betatron electron acceleration upstream of it, due to the foreshock transient motion [Liu et al., 2017b]. Note that although high-frequency whistler mode waves also contribute to electron acceleration in our model [Shi et al., 2023a], the main role of all three wave modes and compressional fluctuations is to trap electrons near the bow shock, allowing them to experience multiple SDA and adiabatic (Fermi and betatron) acceleration.

5.3.1 Electron Resonant Scattering by Waves

Our model of electron resonant scattering due to the wave-particle interactions in the foreshock region includes electrostatic turbulence, high-frequency whistler-mode waves between

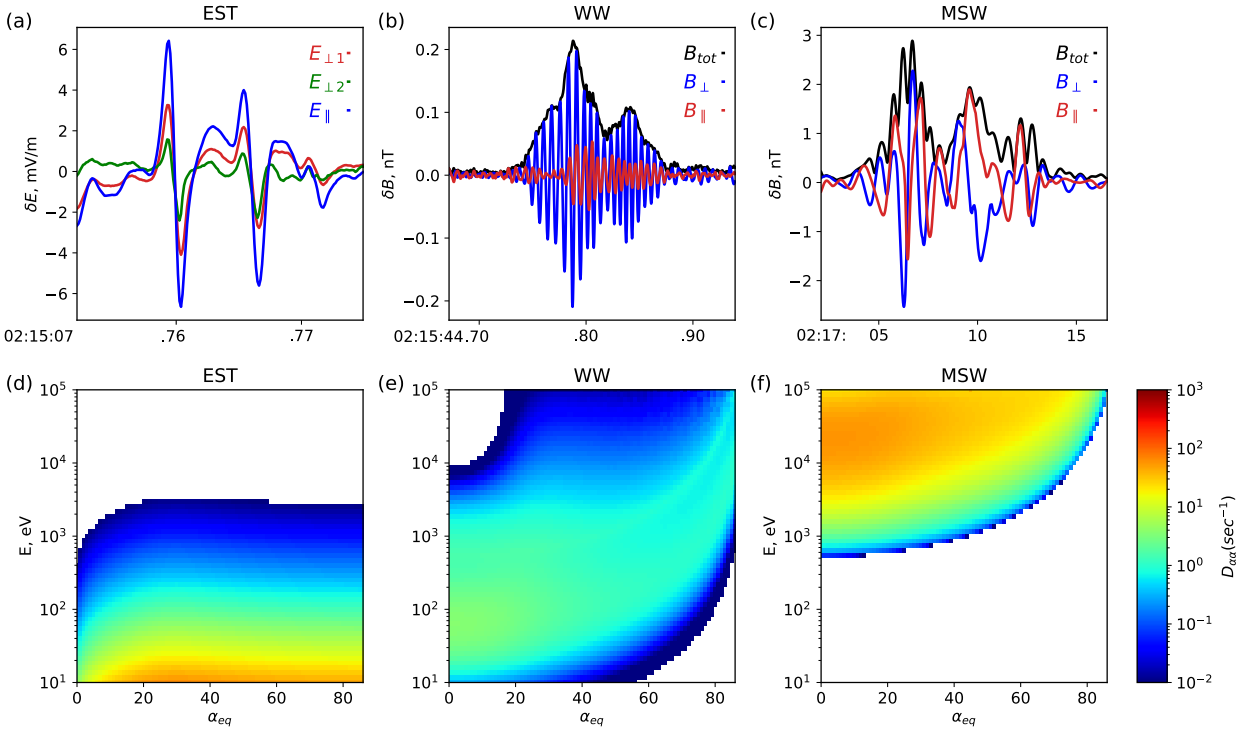

Figure 5.4: Representative waveforms of three types of wave modes typically observed around the compressional boundary of foreshock transients, selected from times of the example shown in Figure 5.2, along with pitch-angle scattering rates associated with typical wave power for such wave modes. (a) Large-amplitude electrostatic (EST) waves seen in electric field measurements (δE); (b) High-frequency whistler-mode (WW) wavepacket, with predominant magnetic field perturbations in the perpendicular direction, suggesting propagation along the background magnetic field; (c) Wavepackets the magnetic field for magnetosonic (MSW) waves. Observation times (UT) are listed in the horizontal axis. Panels (d-f) depict diffusion coefficients for the three types of waves averaged over background magnetic field conditions representative of the large-scale magnetic field perturbation.

the lower-hybrid f_{lh} and the electron cyclotron f_{ce} frequencies, and low-frequency whistler-mode magnetosonic waves, a continuation of whistler-mode below f_{lh}. For each of these modes, we use the theoretical model of quasi-linear scattering rate (pitch-angle diffusion coefficient), $D_{\alpha\alpha}$. Intense electrostatic turbulence around Earth's bow shock consists of different nonlinear waves and packets of intense ion acoustic waves [Vasko et al., 2022, Kamaletdinov et al., 2022]. The scattering rate for such turbulence has been derived and verified in [Vasko et al., 2018a, Vasko et al., 2022]:

$$
\begin{aligned}
D_{\alpha\alpha} &= \int \frac{D^{(\mathrm{X})}_{\alpha\alpha}\mathcal{P}\left(\mathrm{X}\right)\ell\left(\mathrm{X}\right)d\mathrm{X}}{\int \ell\left(\mathrm{X}'\right)\mathcal{P}\left(\mathrm{X}'\right)d\mathrm{X}'}, \quad \mathrm{X}=\left(v_\phi,\ell,\theta,\mathcal{E}_w\right) \\
D^{(\mathrm{X})}_{\alpha\alpha} &= \frac{\mathcal{E}_w^2\Omega_e^2}{4\sqrt{2\pi}N_eE\Omega_{pe}}\frac{\left(\ell/\lambda_D\right)^3}{\sin^2\alpha}\frac{\left(v_\phi\cos\alpha-v\cos\theta\right)^2}{\left|v_\phi-v\cos\alpha\cos\theta\right|^3}\sum_{n=1}^{n=\infty}n^2J_n^2\left(\rho_n\right)e^{-\xi_n} \qquad (5.1) \\
\xi_n &= \frac{n^2\Omega_e^2\left(\ell/\lambda_D\right)^2}{\Omega_{pe}^2\left(v_\phi-v\cos\alpha\cos\theta\right)^2}, \quad \rho_n=\frac{nv\sin\alpha\sin\theta}{v_\phi-v\cos\alpha\cos\theta} \qquad (5.2)
\end{aligned}
$$

where ℓ is the spatial scale of nonlinear waves, λ_D is the Debye length evaluated with the background electron density N_e and temperature, v_ϕ and θ are the phase speed and normal angle (relative to the background magnetic field) of nonlinear waves, $\mathcal{E}_w$ is the wave electric field amplitude, Ω_{ce} and Ω_{pe} are the ambient electron gyrofrequency and plasma frequency, respectively, n is the number of cyclotron resonance, $J_n(\rho_n)$ is the Bessel function, v is the velocity of electrons with the energy E. The first integral is the averaging of the diffusion rate $D^{(\mathrm{X})}_{\alpha\alpha}$ over the probability distribution $\mathcal{P}$ of wave characteristics X (see details of $\mathcal{P}(\mathrm{X})$ in [Vasko et al., 2022]).

The diffusion rate for the whistler-mode waves has been derived [Kennel and Petschek, 1966], and we use the approximation for field-aligned waves resonating with relativistic electrons (this relativistic correction becomes important for $\sim$ 100keV energies) [Summers, 2005]:

$$
\begin{aligned}
D_{\alpha\alpha} &= \frac{\int D_{\alpha\alpha}^{(\mathrm{X})} \mathcal{P}\left(\mathrm{X}\right) d\mathrm{X}}{\int \mathcal{P}\left(\mathrm{X}\right) d\mathrm{X}}, \quad \mathrm{X} = (\omega, \mathcal{B}_w) \\
D_{\alpha\alpha}^{(\mathrm{X})} &= \frac{\pi \mathcal{B}_w^2 \Omega_{ce}}{2B_0^2\gamma^2} \frac{(v - v_\phi \cos\alpha)}{|v\cos\alpha - v_g|} \left|\frac{v_g}{v}\right| F\left(\omega\right)
\end{aligned}
\tag{5.3}
$$

where ω is the wave frequency, γ is the relativistic factor, $\mathcal{B}_w/B_0$ is the ratio of wave magnetic field amplitude and the background field, $v_g = \partial\omega/\partial k$ is the wave group velocity derived from the cold plasma dispersion relation [Stix, 1962], and $F(\omega)$ stands for the power spectrum of the waves. The normalization in the first line provides $\int_{\omega_-}^{\omega_+} F(\omega) d\omega = 1$, where $\omega_\pm$ denote the lower and upper limits of the frequency range, respectively. Notably, magnetosonic waves and high-frequency whistler-mode waves represent the same wave mode (whistler-mode) but with different frequencies: for magnetosonic waves, the frequency range extends from the proton cyclotron frequency to the low-hybrid frequency, whereas for high-frequency whistler-mode waves the frequency range spans from the low-hybrid frequency to the electron cyclotron frequency. The diffusion coefficient for both types of waves can be estimated using Equation 5.3. We conducted separate fittings for the power spectrum, $F(\omega)$, of magnetosonic waves and whistler-mode waves, as illustrated in Figure 5.5(a).

Each type of wave has a specific resonance energy range: electrostatic waves predominantly interact with electrons below 100eV, high-frequency whistler-mode waves primarily influence electrons in the range of 10eV to 1 keV, and magnetosonic waves exert substantial effects on electrons with energies exceeding 1keV. Figure 5.5(b) shows the combined diffusion coefficient of electrostatic waves, high-frequency whistler waves, and magnetosonic waves. The diffusion coefficients are evaluated for the $B_0 = B_{core}$, where B_{core} is the magnetic field magnitude is the core foreshock. However, the foreshock transient region exhibits high amplitude variations of the magnetic field, as depicted in Figure 5.5(c) (where $\mathcal{P}$ represents the probability distribution of background field fluctuations relative to B_{core}). Under such intense magnetic field fluctuations, the wave-particle resonance conditions can strongly vary,

widening the energy range of electrons scattered by each of the three wave modes [Voshchepynets et al., 2015]. To account for this effect, we calculated the diffusion coefficient averaged over the background magnetic field fluctuations.

$$\langle D_{\alpha\alpha}(\alpha, E)\rangle = \frac{\int_0^{B_{max}} D_{\alpha\alpha}(\alpha, E, B_0)\mathcal{P}(B_0)dB_0}{\int_0^{B_{max}} \mathcal{P}(B_0)dB_0} \tag{5.4}$$

Such averaged diffusion coefficient $\langle D_{\alpha\alpha}\rangle$ for the three types of waves is shown in Figure 5.4 of the main text, while the combined result is presented in Figure 5.5(d). The inclusion of background magnetic field fluctuations leads to broader energy, pitch-angle range of finite $\langle D_{\alpha\alpha}\rangle$. The combined effect of these three wave modes, enhanced by background magnetic field fluctuations, facilitates the scattering of electrons across a broad energy spectrum - from 10eV to 100keV, encompassing all pitch angles. This overlap provides a continuous path in energy from 10s of eV to 10s of keV for electrons to be scattered by these waves. The most intense of these compressional fluctuations, the foreshock transient boundaries, contribute as well by adiabatically reflecting electrons thus increasing the probability of electron trapping.

5.3.2 Numerical Simulation

To reproduce the observed electron spectrum, we simulate electron dynamics affected by a combination of electron scattering and acceleration. We start the simulation with the solar wind electron distribution (grey color) where most of the electrons have energies below 100eV (although there is a finite population up to 1keV), and aim to resolve the question of electron acceleration up to $100 - 200$keV (see Figure 5.6). When we include only SDA and adiabatic reflection from the compressional magnetic field fluctuations of foreshock transients, most electrons escape the foreshock region after ~ 7 reflections from the shock, and the maximum acceleration does not exceed $1-3$ keV (magenta curve). If EST scattering is added, electrons may experience up to ~ 12 reflections from the shock and gain $3 - 5$keV (red curve). The inclusion of electron WW scattering and acceleration increases the number of electron reflec-

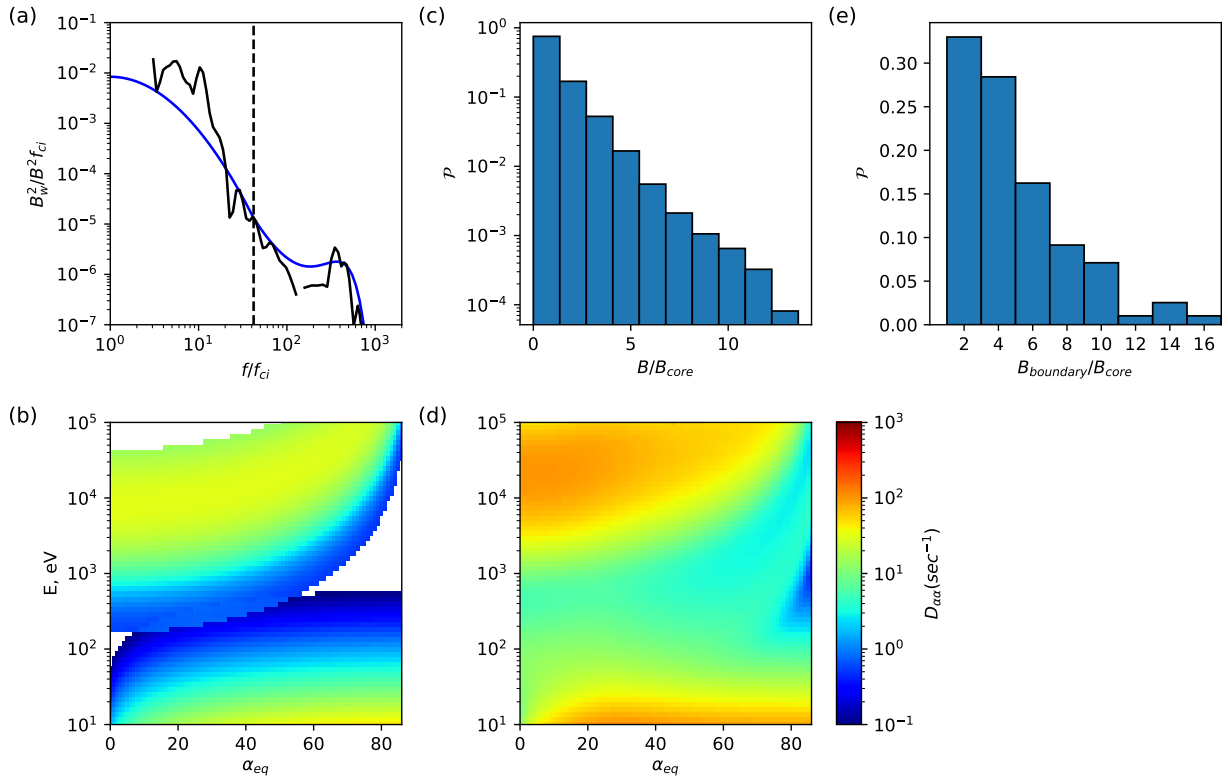

Figure 5.5: Derivation of simulation parameters for waves. (a) observed magnetic field power spectrum of magnetosonic waves and high-frequency whistler-mode waves (black lines) and a fit to the observations (blue line); (b) combined diffusion coefficient for the three types of waves calculated at the minimum magnetic field (inside the core); (c) distribution of magnetic field perturbations within foreshock transient structures; (d) combined diffusion coefficient averaged over the background magnetic field perturbations; (e) distribution of the ratio $B_{boundary}/B_{core}$.

tions from the shock further, up to ~ 24, with the electron energy gain reaching $5-7$keV (green curve). Scattering of more than a few keV electrons requires the inclusion of MSW scattering, which increases the number of electron reflections from the bow shock to ~ 40, whereas the electron energy gain reaches $10-20$keV (blue curve). Therefore, a combination of SDA, adiabatic reflection from the foreshock transients, and resonant scattering by three different wave modes can provide acceleration of <100eV solar wind electrons to ~ 20keV. The next effect to be included is the Fermi and betatron adiabatic acceleration. The leading edge of the foreshock transient often forms its shock wave propagating upstream ahead of the bow shock with a velocity comparable to that of the bow shock. Electrons trapped between two shocks moving toward each other (bow shock and transient shock) experience Fermi acceleration [Hietala et al., 2012]. As the foreshock transient moves (collapses) onto the bow shock, its magnetic field is compressed, increasing by a factor of ~ 3 (see [Liu et al., 2019]). This effect should provide electron betatron heating [Liu et al., 2019]. Figure 5.6 shows that when both Fermi and betatron adiabatic (AD) acceleration are also included in the simulation, the electron spectrum reaches ~ 200keV and attains a power law falloff $\sim E^{-4}$ (black curve). The variability of the model output spectrum due to uncertainties in the bow shock speed determination is depicted by the blue-shaded region.

The numerical simulation of electron dynamics, scattering, and acceleration is based on the probabilistic approach [Tao et al., 2008, Shi et al., 2023], which is similar to the Monter-Carlo approach usually applied to astrophysical shock waves [Kirk and Schneider, 1987, Bykov et al., 2017]. An elementary model time-step of electron dynamics is the bounce period between the bow shock and the foreshock transient. If the electron pitch-angle is sufficiently small to cross the bow shock or the foreshock transient boundary, it is considered to be lost and a new electron with the solar wind energy substitutes this lost electron in the simulation. The bow shock magnetic field has a spatial gradient increasing it ~ 4 times from the core field and we do not change the shock configuration for the entire simulation, whereas for each electron interaction with the foreshock transient boundary we generate the transient

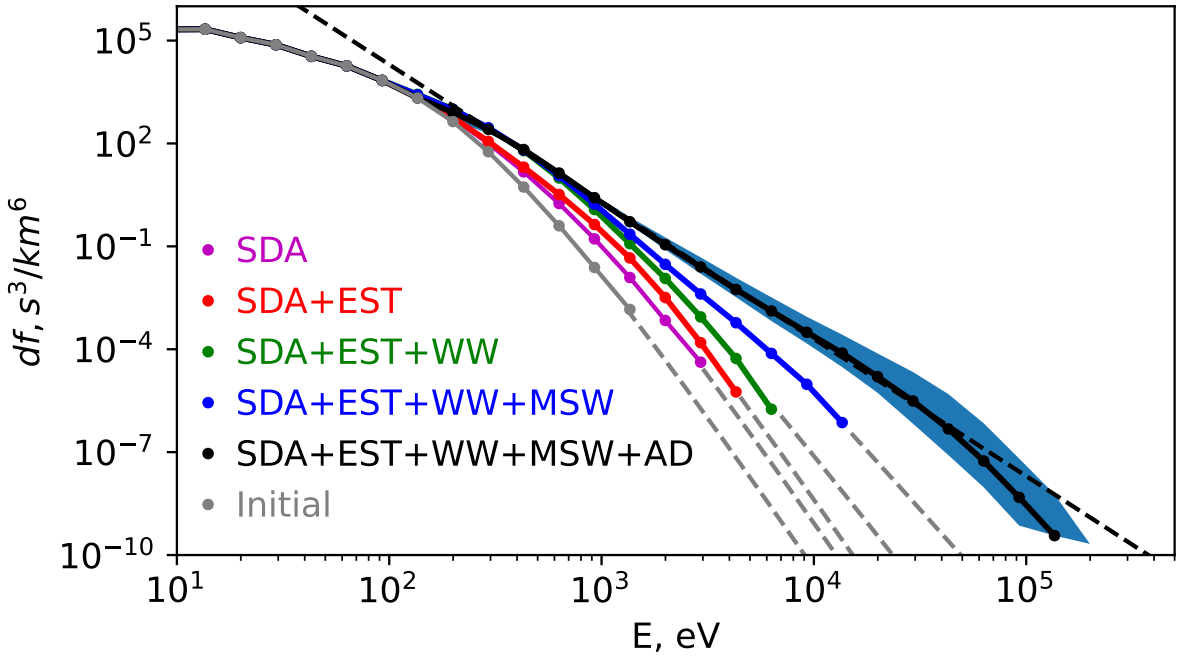

Figure 5.6: Results of our modeling of the compound electron acceleration process, successively incorporating various effects considered in this chapter. Formation of the observed E^{-4} energy spectrum necessitates the inclusion of all the effects considered in this study. Gray solid line: initial electron distribution; Magenta line: model results considering only the adiabatic reflection by ultra-low-frequency magnetic field fluctuations and SDA acceleration at the bow shock; Red, green, and blue lines: progressive addition of pitch-angle scattering by EST, WW and MSW waves, respectively; Black line: adding the adiabatic Fermi and betatron acceleration to all the other effects. Only when all the effects discussed are compounded does the result adhere to $df \propto E^{-4}$, consistent with observations. The blue-shaded region indicates the variability in the results when different adiabatic parameters are chosen (e.g., the shock normal speed is varied in the range of $800 - 1200$km/s). The dashed gray lines fit the high energy portion of the spectra, shown for clarity.

boundary magnetic field $B_{boudnary}/B_{core}$ from the distribution function of $B_{boudnary}/B_{core}$ obtained in MMS statistics (see Figure 5.5(e)). We assume there can be three transient structures during a time interval in the foreshock [Chu et al., 2017b], so electrons have three chances to be reflected by the transient boundary (see discussion below). Although the number of particles is conserved within the simulation, we also assume that the core of solar wind electron distribution remains unchanged (as there is an almost infinite source of for this core), and in Figure 5.6 we add a small population of solar wind electrons with < 100eV energy to all spectra to make them the same for < 100eV energy range.

Within one bounce period, each electron has the opportunity to experience the combined effects of shock drift acceleration (SDA), pitch-angle scattering induced by electrostatic turbulence, high-frequency whistler waves, and magnetosonic waves. Additionally, electron energy can be changed by wave-particle resonant interactions with high-frequency whistler-mode waves, Fermi acceleration due to reflection from the moving boundary of the foreshock transient, and betatron acceleration resulting from the increase in the core magnetic field due to plasma compression by the moving foreshock transient [Liu et al., 2019, Liu et al., 2017b]. The equations describing electron energy E and pitch-angle α recalculation within one bounce period (between n and $n+1$ bounces) are:

$$
\begin{aligned}
&\alpha_{n+1/2} = \alpha_n + \sum_{i=EST,WW,MSW} W_i \sqrt{\langle D_{\alpha\alpha}(E_n, \alpha_n)\rangle_i} \\
&E_{\parallel,n+1/2} = E_{\parallel,n} + \Delta E_{\parallel,WW}(E_n, \alpha_n + 1/2) \\
&E_{\perp,n+1/2} = E_{\perp,n} + \Delta E_{\perp,WW}(E_n, \alpha_n + 1/2) \\
&E_{\parallel,n+1} = E_{\parallel,n+1/2} + \Delta E_{\text{Fermi}}(E_{\parallel,n+1/2}) + \Delta E_{\text{SDA}}(E_{\parallel,n+1/2}) \\
&E_{\perp,n+1} = E_{\perp,n+1/2} + \Delta E_{\text{Beta}}(E_{\perp,n+1/2}) \\
&\alpha_{n+1} = \arctan(E_{\perp,n+1}/E_{\parallel,n+1})
\end{aligned}
\tag{5.5}
$$

where $W_i = \mathcal{N} \cdot dt$, and $\mathcal{N}(0,1)$ is a random number from the normal Gaussian probability distribution with a zero mean value and unity dispersion [Tao et al., 2008], $dt = \int_L ds/v_\parallel$ represents the time-scale electrons spend around the foreshock transient boundary (where

all wave modes are hosted), with L denoting the spatial scale of this boundary. The energy change caused by resonant interactions between high-frequency whistler-mode waves and electrons (ΔE_{WW}) is calculated based on the conservation law $E(1-\omega/\Omega_e \sin\alpha^2) = const.$ Fermi acceleration and SDA change the parallel velocity (energy) component, given by $\Delta E_{\parallel,\mathrm{Fermi}} = 2m_e v_f^2$, where the bow shock and foreshock transient boundary speed, v_f, is distributed by normal Gaussian probability distribution with a mean value of 1000 km/s and a standard deviation of 400 km/s, which correspond to the shock speed $\sim$ 100km/s (see [Kruparova et al., 2019]) and shock normal angle above 85° (see [Lalti et al., 2022a]). Betatron acceleration changes the perpendicular component as $\Delta E_{\perp,\mathrm{beta}} = E_{\perp,n}\left((B+\delta B)/B - 1\right)$, where δB is the core magnetic field increment for dt time-scale (we consider $\sum \delta B/B = 3$ for the entire simulation period).

Most of the system parameters for numerical simulations of electron dynamics, scattering, and acceleration are selected according to spacecraft statistical observations. However, the role of a free model parameter, the number of simultaneously existing foreshock transients, requires additional verification. The number of such transients determines the probability of electron adiabatic reflection in the foreshock and thus should affect the electron acceleration efficiency. Figure 5.7(a) shows that with other system parameters fixed, the increase/decrease of the number of foreshock transients ($n = 3 \pm 1$) results in a variation of phase space density of $>$ 10keV electrons and maximum energies within $\in [75, 300]$keV. Therefore, this free parameter has significant control over the final accelerated electron spectrum. For the event of Figure 5.2 the selected number of transients ($n = 3$) is consistent with the observations (in Figure 5.2 (a,b), MMS observed three transient structures in the foreshock region), and provides the best fit to the observed electron spectrum.

Solar wind electron acceleration from $10-100$eV energies to $\sim$ 200keV requires $\sim 50-100$ of scatterings and reflections from the foreshock transients, and each such reflection is a probabilistic process. Therefore, the simulation should contain a sufficient number of test particles to provide good statistics of low-probability multiple reflections, corresponding to

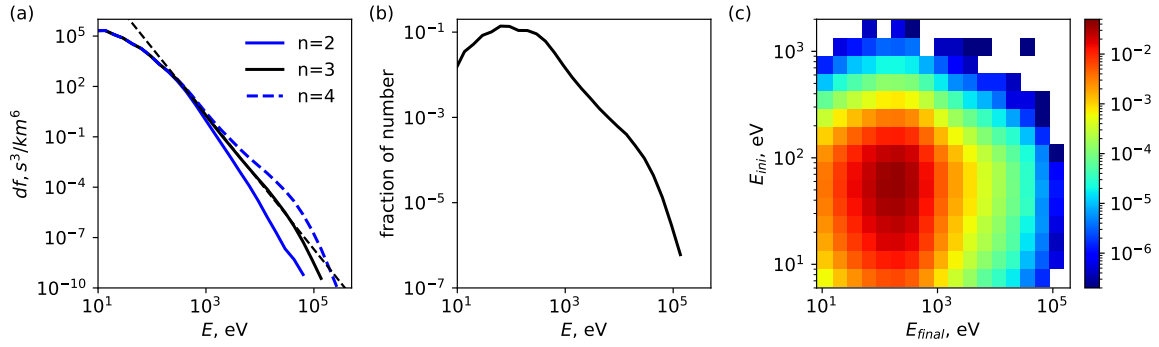

Figure 5.7: Investigation of the role of multiple foreshock transient crossings in the electron energization. (a) effect of the number of foreshock transients (n_t) on electron spectrum: as n_t increases, electrons can be accelerated to higher energies; (b) normalized number density distribution of the final result of a simulation with 5×10^7 electrons; (c) probability distribution in the (initial energy, final energy) space, demonstrating that the main source of the accelerated particles is the core of the solar wind (< 100 eV).

the most accelerated electron population. Figure 5.7(b) shows that number of electrons reaching $\sim$ 200keV is about $\times 10^{-6}$ smaller than the number of core electron population $\sim 10 - 100$eV. In our simulation setup, we consider 5×10^7 test particles to describe well the tail of the electron energy spectrum. Note this tail with $\sim$ 200keV energies is mostly formed by the core solar wind distribution, $[10, 100]$ eV. Although the probability of > 100eV to be trapped and further accelerated to higher energies is expected to be higher than for < 100eV electrons, Figure 5.7(c) shows that this hot solar wind population has too low fluxes to contribute to the 100keV population, i.e. in the solar wind spectrum the number of particles decreases with the energy increase much faster than the probability to be trapped and accelerated in the foreshock increases with the energy.

5.4 Summary

The good agreement of the model results of Figure 5.6 with observations in Figure 5.2(i) validates the proposed scenario of solar wind electron acceleration in the foreshock to $100 - 200$keV. Such acceleration transforms a small subset of the initial $<$ 1keV solar wind electron distribution (comprising a core population below 100eV and an exponential energy tail) into a power law distribution with an E^{-4} falloff, a power law in the 1-200keV energy range. Importantly, efficient electron acceleration from solar wind energies, $\sim 10 - 100$eV, up to near-relativistic energies, $\sim$ 200keV, cannot be otherwise explained by a single mechanism of electron scattering. Rather, multiple wave modes, adiabatic reflections, and adiabatic Fermi and betatron acceleration compound the energy gain arising from shock drift acceleration, allowing electrons of progressively higher energies to continue to be scattered upstream and have the opportunity to be further accelerated.

The proposed compound acceleration mechanism successfully reproduces the electron acceleration by a factor of $10,000$ within the compact region of the foreshock and thus provides a quantitative solution to the problem of collisionless shock acceleration that has remained unresolved for decades. This mechanism reveals the key role played by multiple wave modes (ES, EE, MSW) in trapping electrons (via pitch-angle scattering) within the foreshock region and providing stable conditions for electron energization. The same plasma kinetics (wave-particle resonant interactions) may resolve electron acceleration at other heliospheric [Masters et al., 2013] and astrophysical [Koyama et al., 1995, Aharonian et al., 2004] shock regimes with appropriate parameter scaling. Therefore, the proposed and verified acceleration mechanism is expected to change our understanding of particle acceleration at shocks physics and may be important in particle acceleration and the generation of cosmic rays at other astrophysical settings shocks throughout the cosmos.

CHAPTER 6

Summary and Future Work

6.1 Research Summary

For decades we have observed ultra high energy cosmic rays which are believed to be generated around astrophysical shock waves. However, all theories assumed a pre-existing pool of suprathermal particles that undergo acceleration to ultrahigh energies. The source of these suprathermal particles – called the "injection problem" – remains an outstanding problem even though it is the most crucial part of the energization process. This thesis focuses on how the electrons are accelerated in planetary foreshocks and provides a solution that is readily available at all astrophysical shocks and may explain numerous outstanding problems in solar and astrophysics.

Spacecraft frequently observe relativistic electron populations within the foreshock region, characterized by energy levels surpassing those of solar wind electrons by four orders of magnitudes or more. However, mechanisms for such strong acceleration remain elusive. Although there are many well-developed theories for particle acceleration around the bow shock, such as shock drift acceleration, stochastic shock drift acceleration, and betatron and Fermi heating, these mechanisms cannot fully resolve the observed high-energy electron energy spectra.

Electromagnetic waves in the foreshock region have been reported decades ago, yet their role in electron acceleration within the foreshock regions has remained largely unexplored. One of the most important wave modes, the whistler-mode waves, is an important wave mode

known for their capacity to effectively scatter and accelerate electrons in the inner magnetosphere. While the theoretical framework for studying interactions between whistler-mode waves and electrons has been well established in the radiation belt region, the foreshock presents different plasma conditions and electron energy ranges. Consequently, the specific effects of resonant interactions with whistler-mode waves in the foreshock need to be investigated individually. Despite the distinct plasma parameters characterizing the foreshock, the observational and theoretical techniques developed for the inner magnetosphere offer valuable guidance for studying wave-particle interactions in the foreshock. By leveraging this existing knowledge and adapting it to the unique conditions of the foreshock, we can advance our understanding of electron acceleration processes in this region. Through statistical analysis of in-situ observations near Earth's bow shock gathered from the THEMIS and MMS datasets and theoretical approaches to model wave-particle interactions, we built a compound acceleration model. This model represents a significant advancement as it successfully replicates the near-relativistic electron energy spectra observed in the vicinity of Earth for the first time.

We first conducted a case study and a statistical analysis of high-frequency whistler waves (with frequencies above the low-hybrid frequency) in the foreshock region. We explored their spatial distribution, wave properties, and regime of resonant interactions. Through statistical analysis in Chapter 2, we demonstrated that whistler waves are frequently present near foreshock transient structures with a high occurrence rate, and we also obtained typical wave properties such as wave frequency, frequency bandwidth, wave normal angle, and wave amplitude. We found that the electron resonance energy range is around $10s$ eV to a few hundred eV. Additionally, a subset of these waves displayed large amplitudes, reaching up to one percent of the background magnetic field. The interaction between waves and electrons in the foreshock region has two regimes: (quasi-)linear and nonlinear. These regimes necessitate different theoretical frameworks and exhibit different effects on electron scattering and acceleration. The resonant regimes depend on the wave intensities, background

field gradients, and wave coherency. Quasi-linear interactions occur when wave amplitudes are relatively small, and the waves are broadband. Conversely, nonlinear interactions can markedly influence electron trajectories and occur when waves are sufficiently intense and highly coherent. Our analysis indicates that the majority of observed waves in the foreshock satisfy the conditions for quasi-linear interactions. We conducted a case study to assess the efficiency of pitch-angle scattering using the quasi-linear approximation, and revealed that whistler waves in foreshock transients can effectively scatter electrons within short time intervals. While quasi-linear interactions dominate, a portion of the waves can interact with electrons nonlinearly, with pronounced effects on electron dynamics.

In Chapter 3 and Chapter 4, we further investigated the nonlinear effects observed in the foreshock region. Through a combination of case studies and test-particle simulations, we provided observational evidence demonstrating that nonlinear interactions can accelerate electrons and reproduce the characteristic butterfly electron distribution. Our case study demonstrated that nonlinear interactions can efficiently accelerate and scatter electrons within the foreshock. Furthermore, we introduced two theoretical approaches: the probabilistic approach and the mapping technique. These methods allow us to theoretically trace electron dynamics without relying on test-particle simulations, thereby offering significant computational advantages. In developing these theoretical approaches, we carefully considered realistic wave packet sizes obtained from observations, as the size of wave packets can influence nonlinear interactions.

In Chapter 5, we synthesized our understanding of whistler-mode waves with the theoretical framework to solve the electron acceleration problem. Using observations of electrons with energies up to 200 keV and a data-constrained model, we reproduced the observed power-law electron spectrum, $\sim E^{-4}$, and demonstrated that the acceleration by more than 4 orders of magnitude is a compound process including a complex, multi-step interaction between more commonly known mechanisms (adiabatic acceleration and shock drift acceleration) and resonant scattering by several plasma wave modes. The proposed model of

electron acceleration addresses the decades-long issue of the generation of energetic (and relativistic) electrons at planetary plasma shocks.

In summary, this thesis focuses on the electron acceleration in foreshock regions problem and, for the first time, successfully reproduces the observed acceleration by a factor of 10^4, from 10eV up to several hundred keV. The proposed acceleration mechanism is compound acceleration by a combination of mechanisms, which have never before been considered in aggregate. These results may deepen our understanding of particle acceleration in shock physics and be important in particle acceleration and the generation of cosmic rays at other astrophysical settings shocks throughout the cosmos.

6.2 Future Work

In future study, we plan to substantially expand our model to incorporate effects such as wave obliquity and self-consistent wave-particle dynamics when waves that facilitate the acceleration of electron populations are generated by suprathermal populations associated with the same foreshock transients.

6.2.1 Role of ultra-low-frequency fluctuations in electron Heating: Magnetic Pumping and Whistler-Mode Waves

Self-consistent wave generation and electron acceleration can occur in various magnetic field configurations; however, configurations involving compressional electron heating are particularly promising for research. In these configurations, energy from large-scale plasma dynamics is converted into electron anisotropy, which subsequently facilitates the generation of whistler-mode waves and further accelerates electrons. A typical example of such configurations near Earth's bow shock involves compressional ultra-low-frequency waves that drive the so-called pumping mechanism for self-consistent electron acceleration.

The magnetic pumping process involves electron adiabatic (compressional) heating due

to ultra-low-frequency waves, along with simultaneous scattering by high-frequency fluctuations. Specifically, when the electron energy undergoes adiabatic (reversible) changes due to magnetic field fluctuations and is coupled with electron pitch-angle scattering from high-frequency waves (turbulence), this scattering disrupts the reversibility and promotes electron heating [Lichko et al., 2017, Egedal et al., 2018]. The theory of magnetic pumping and its validation using observational data from shock waves and high-frequency wave models are discussed in various studies [Lichko and Egedal, 2020, Egedal and Lichko, 2021, Egedal et al., 2021, Montag and Howes, 2022]. Similarly, the electron heating mechanism involving adiabatic modulation and scattering by high-frequency waves has been explored for the intracluster medium [Kunz et al., 2011, Ley et al., 2023] and planetary magnetospheres [Borovsky et al., 2017].

An important, but yet underexplored aspect of magnetic pumping is the origin of high-frequency waves responsible for electron scattering. There are multiple electrostatic wave modes around Earth's bow shock [Vasko et al., 2022, Kamaletdinov et al., 2022, Wang et al., 2020, Lalti et al., 2023] that effectively scatter solar wind electrons [Vasko et al., 2018b, Gedalin, 2020, Kamaletdinov et al., 2022]. However, the most important wave mode for magnetic pumping is the electromagnetic high-frequency whistler-mode wave which can be generated by the adiabatically modulated electron population [Huang et al., 2018, Yao et al., 2021, Jiang et al., 2022]. The magnetic pumping can be self-consistently supported by the whistler-mode wave generation and the electron scattering by these waves. Figure 6.1 illustrates this scenario using an example from THEMIS [Angelopoulos, 2008] observations around Earth's bow shock. Ultra-low-frequency magnetic field fluctuations (top panels) create local magnetic field dips with the trapped hot electrons and strong whistler-mode wave activities (bottom panel). The compressional dynamics of such magnetic field fluctuations periodically heat and cool the trapped electrons [Yao et al., 2021, Jiang et al., 2022], whereas whistler-mode waves may scatter electrons in the pitch-angle space and provide redistribution of the electron energy between the cross-field and field-aligned directions. [Lichko et al., 2017,

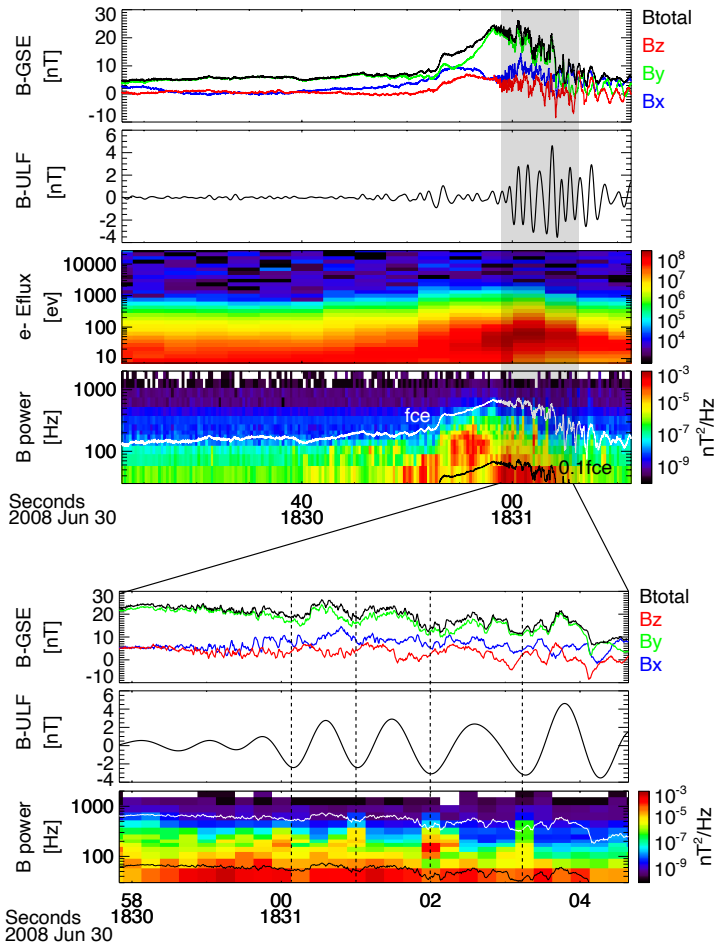

Figure 6.1: An overview of THEMIS (Angelopoulos 2008) observations of ultralow-frequency magnetic field fluctuations upstream of Earth's bow shock.

Lichko and Egedal, 2020] have shown that such a combination of adiabatic (reversible) energy variation and pitch-angle scattering should result in electron heating and the formation of a suprathermal electron population. In future study we may incorporate such a magnetic pumping mechanism into our model of electron acceleration in the foreshock. This will allow us to include the electron pitch-angle scattering and heating provided by self-consistently generated whistler-mode waves. Such self-consistent elements of electron dynamics are the perspective direction for improving the simulations of electron foreshock acceleration.

6.2.2 Oblique Whistler Waves

In the thesis, we mainly focus on whistler-mode waves propagating quasi-parallel to the background magnetic field (with an angle ψ between the wavevector k and the magnetic field B around zero). The natural and potentially important generalization of this assumption is to consider wave obliquity. Although observational data suggest that most high-frequency whistler waves exhibit weak obliqueness, a portion of the waves are observed to be oblique. As depicted in Figure 2.2, the wave normal angle distribution for high-frequency whistler waves peaks around $\psi = 10°$, with a portion of the waves having wave normal angles exceeding 30°. The obliquity of whistler-mode waves has been extensively studied in the inner magnetosphere, revealing their significant impact on electron scattering, acceleration, and precipitation into the atmosphere [Artemyev et al., 2016]. When waves propagate parallel to the magnetic field, only cyclotron resonance ($n = 1$ in Equation 2.4) occurs. However, oblique wave propagation introduces Landau resonance ($n = 0$) and higher-order resonances [Albert, 2017]. Consequently, the diffusion coefficient for oblique waves encompasses a wider range of pitch angles and energy levels compared to that of parallel propagating waves. Oblique chorus waves have been shown in the magnetosphere to significantly increase diffusion rates at high energy [Gan et al., 2022, Lorentzen et al., 2001] and can also effectively scatter electrons up to several hundreds of keV [Lorentzen et al., 2001, Mourenas et al., 2012]. Furthermore, if we incorporate background field fluctuations as discussed in Chapter 5, we may even further broaden the energy range and pitch angle range of resonant interactions.

In a future proposed work, we will calculate the diffusion coefficient for the oblique whistler waves, and further incorporate this effect in the model described in Chapter 5 to study their effects on the electron acceleration process.

REFERENCES

[Aharonian et al., 2004] Aharonian, F. A., Akhperjanian, A. G., Aye, K. M., Bazer-Bachi, A. R., Beilicke, M., Benbow, W., Berge, D., Berghaus, P., Bernlöhr, K., Bolz, O., Boisson, C., Borgmeier, C., Breitling, F., Brown, A. M., Bussons Gordo, J., Chadwick, P. M., Chitnis, V. R., Chounet, L. M., Cornils, R., Costamante, L., Degrange, B., Djannati-Ataï, A., Drury, L. O., Ergin, T., Espigat, P., Feinstein, F., Fleury, P., Fontaine, G., Funk, S., Gallant, Y. A., Giebels, B., Gillessen, S., Goret, P., Guy, J., Hadjichristidis, C., Hauser, M., Heinzelmann, G., Henri, G., Hermann, G., Hinton, J. A., Hofmann, W., Holleran, M., Horns, D., de Jager, O. C., Jung, I., Khélifi, B., Komin, N., Konopelko, A., Latham, I. J., Le Gallou, R., Lemoine, M., Lemière, A., Leroy, N., Lohse, T., Marcowith, A., Masterson, C., McComb, T. J. L., de Naurois, M., Nolan, S. J., Noutsos, A., Orford, K. J., Osborne, J. L., Ouchrif, M., Panter, M., Pelletier, G., Pita, S., Pohl, M., Pühlhofer, G., Punch, M., Raubenheimer, B. C., Raue, M., Raux, J., Rayner, S. M., Redondo, I., Reimer, A., Reimer, O., Ripken, J., Rivoal, M., Rob, L., Rolland, L., Rowell, G., Sahakian, V., Saugé, L., Schlenker, S., Schlickeiser, R., Schuster, C., Schwanke, U., Siewert, M., Sol, H., Steenkamp, R., Stegmann, C., Tavernet, J. P., Théoret, C. G., Tluczykont, M., van der Walt, D. J., Vasileiadis, G., Vincent, P., Visser, B., Völk, H. J., and Wagner, S. J. (2004). High-energy particle acceleration in the shell of a supernova remnant. *Nature*, 432(7013):75–77.

[Albert, 1993] Albert, J. M. (1993). Cyclotron resonance in an inhomogeneous magnetic field. *Physics of Fluids B*, 5:2744–2750.

[Albert, 2000] Albert, J. M. (2000). Gyroresonant interactions of radiation belt particles with a monochromatic electromagnetic wave. *J. Geophys. Res.*, 105:21191.

[Albert, 2017] Albert, J. M. (2017). Quasi-linear diffusion coefficients for highly oblique whistler mode waves. *J. Geophys. Res.*, 122:5339–5354.

[Albert et al., 2022a] Albert, J. M., Artemyev, A., Li, W., Gan, L., and Ma, Q. (2022a). Analytical results for phase bunching in the pendulum model of wave-particle interactions. *Frontiers in Astronomy and Space Sciences*, 9:971358.

[Albert et al., 2022b] Albert, J. M., Artemyev, A., Li, W., Gan, L., and Ma, Q. (2022b). Equations of Motion Near Cyclotron Resonance. *Frontiers in Astronomy and Space Sciences*, 9:910224.

[Albert et al., 2021] Albert, J. M., Artemyev, A. V., Li, W., Gan, L., and Ma, Q. (2021). Models of resonant wave-particle interactions. *Journal of Geophysical Research: Space Physics*, 126(6):e2021JA029216.

[Albert et al., 2013] Albert, J. M., Tao, X., and Bortnik, J. (2013). Aspects of Nonlinear Wave-Particle Interactions. In Summers, D., Mann, I. U., Baker, D. N., and Schulz, M.,

editors, *Dynamics of the Earth's Radiation Belts and Inner Magnetosphere*, American Geophysical Union.

[Allanson et al., 2021] Allanson, O., Watt, C. E. J., Allison, H. J., and Ratcliffe, H. (2021). Electron Diffusion and Advection During Nonlinear Interactions With Whistler Mode Waves. *Journal of Geophysical Research (Space Physics)*, 126(5):e28793.

[Allanson et al., 2020] Allanson, O., Watt, C. E. J., Ratcliffe, H., Allison, H. J., Meredith, N. P., Bentley, S. N., Ross, J. P. J., and Glauert, S. A. (2020). Particle-in-Cell Experiments Examine Electron Diffusion by Whistler-Mode Waves: 2. Quasi-Linear and Nonlinear Dynamics. *Journal of Geophysical Research (Space Physics)*, 125(7):e27949.

[Allison and Shprits, 2020] Allison, H. J. and Shprits, Y. Y. (2020). Local heating of radiation belt electrons to ultra-relativistic energies. *Nature Communications*, 11:4533.

[Amano and Hoshino, 2022] Amano, T. and Hoshino, M. (2022). Theory of Electron Injection at Oblique Shock of Finite Thickness. *Astrophys. J.* , 927(1):132.

[Amano et al., 2020] Amano, T., Katou, T., Kitamura, N., Oka, M., Matsumoto, Y., Hoshino, M., Saito, Y., Yokota, S., Giles, B. L., Paterson, W. R., Russell, C. T., Le Contel, O., Ergun, R. E., Lindqvist, P. A., Turner, D. L., Fennell, J. F., and Blake, J. B. (2020). Observational Evidence for Stochastic Shock Drift Acceleration of Electrons at the Earth's Bow Shock. *Phys. Rev. Lett.*, 124(6):065101.

[Amano et al., 2022] Amano, T., Matsumoto, Y., Bohdan, A., Kobzar, O., Matsukiyo, S., Oka, M., Niemiec, J., Pohl, M., and Hoshino, M. (2022). Nonthermal electron acceleration at collisionless quasi-perpendicular shocks. *Reviews of Modern Plasma Physics*, 6(1):29.

[An et al., 2020] An, X., Liu, T. Z., Bortnik, J., Osmane, A., and Angelopoulos, V. (2020). Formation of Foreshock Transients and Associated Secondary Shocks. *Astrophys. J.* , 901(1):73.

[An et al., 2022] An, Z., Wu, Y., and Tao, X. (2022). Electron Dynamics in a Chorus Wave Field Generated From Particle-In-Cell Simulations. *Geophys. Res. Lett.*, 49(3):e97778.

[Angelopoulos, 2008] Angelopoulos, V. (2008). The THEMIS Mission. *Space Sci. Rev.*, 141:5–34.

[Angelopoulos et al., 2008] Angelopoulos, V., McFadden, J. P., Larson, D., Carlson, C. W., Mende, S. B., Frey, H., Phan, T., Sibeck, D. G., Glassmeier, K., Auster, U., Donovan, E., Mann, I. R., Rae, I. J., Russell, C. T., Runov, A., Zhou, X., and Kepko, L. (2008). Tail Reconnection Triggering Substorm Onset. *Science*, 321:931–935.

[Archer et al., 2015] Archer, M. O., Turner, D. L., Eastwood, J. P., Schwartz, S. J., and Horbury, T. S. (2015). Global impacts of a Foreshock Bubble: Magnetosheath, magnetopause and ground-based observations. *Plan. Sp. Sci.*, 106:56–66.

[Artemyev et al., 2016] Artemyev, A. V., Agapitov, O., Mourenas, D., Krasnoselskikh, V., Shastun, V., and Mozer, F. (2016). Oblique Whistler-Mode Waves in the Earth's Inner Magnetosphere: Energy Distribution, Origins, and Role in Radiation Belt Dynamics. *Space Sci. Rev.*, 200(1-4):261–355.

[Artemyev et al., 2023] Artemyev, A. V., Albert, J. M., Neishtadt, A. I., and Mourenas, D. (2023). The effect of wave frequency drift on the electron nonlinear resonant interaction with whistler-mode waves. *Physics of Plasmas*, 30(1):012901.

[Artemyev et al., 2019a] Artemyev, A. V., Angelopoulos, V., Vasko, I.-Y., Runov, A., Avanov, L. A., Giles, B. L., Russell, C. T., and Strangeway, R. J. (2019a). On the kinetic nature of solar wind discontinuiti. *Geophys. Res. Lett.*, 46:1185–1194.

[Artemyev et al., 2012] Artemyev, A. V., Krasnoselskikh, V., Agapitov, O., Mourenas, D., and Rolland, G. (2012). Non-diffusive resonant acceleration of electrons in the radiation belts. *Physics of Plasmas*, 19:122901.

[Artemyev et al., 2021a] Artemyev, A. V., Neishtadt, A. I., Albert, J. M., Gan, L., Li, W., and Ma, Q. (2021a). Theoretical model of the nonlinear resonant interaction of whistler-mode waves and field-aligned electrons. *Physics of Plasmas*, 28(5):052902.

[Artemyev et al., 2018a] Artemyev, A. V., Neishtadt, A. I., Vainchtein, D. L., Vasiliev, A. A., Vasko, I. Y., and Zelenyi, L. M. (2018a). Trapping (capture) into resonance and scattering on resonance: Summary of results for space plasma systems. *Communications in Nonlinear Science and Numerical Simulations*, 65:111–160.

[Artemyev et al., 2019b] Artemyev, A. V., Neishtadt, A. I., and Vasiliev, A. A. (2019b). Kinetic equation for nonlinear wave-particle interaction: Solution properties and asymptotic dynamics. *Physica D Nonlinear Phenomena*, 393:1–8.

[Artemyev et al., 2020] Artemyev, A. V., Neishtadt, A. I., and Vasiliev, A. A. (2020). Mapping for nonlinear electron interaction with whistler-mode waves. *Physics of Plasmas*, 27(4):042902.

[Artemyev et al., 2017] Artemyev, A. V., Neishtadt, A. I., Vasiliev, A. A., and Mourenas, D. (2017). Probabilistic approach to nonlinear wave-particle resonant interaction. *Phys. Rev. E* , 95(2):023204.

[Artemyev et al., 2018b] Artemyev, A. V., Neishtadt, A. I., Vasiliev, A. A., and Mourenas, D. (2018b). Long-term evolution of electron distribution function due to nonlinear resonant interaction with whistler mode waves. *Journal of Plasma Physics*, 84:905840206.

[Artemyev et al., 2021b] Artemyev, A. V., Neishtadt, A. I., Vasiliev, A. A., and Mourenas, D. (2021b). Transitional regime of electron resonant interaction with whistler-mode waves in inhomogeneous space plasma. *Phys. Rev. E* , 104(5):055203.

[Artemyev et al., 2021c] Artemyev, A. V., Neishtadt, A. I., Vasiliev, A. A., Zhang, X.-J., Mourenas, D., and Vainchtein, D. (2021c). Long-term dynamics driven by resonant wave-particle interactions: from Hamiltonian resonance theory to phase space mapping. *Journal of Plasma Physics*, 87(2):835870201.

[Artemyev et al., 2022a] Artemyev, A. V., Shi, X., Liu, T. Z., Zhang, X. J., Vasko, I., and Angelopoulos, V. (2022a). Electron Resonant Interaction With Whistler Waves Around Foreshock Transients and the Bow Shock Behind the Terminator. *Journal of Geophysical Research (Space Physics)*, 127(2):e29820.

[Artemyev et al., 2022b] Artemyev, A. V., Shi, X., Liu, T. Z., Zhang, X. J., Vasko, I., and Angelopoulos, V. (2022b). Electron Resonant Interaction With Whistler Waves Around Foreshock Transients and the Bow Shock Behind the Terminator. *Journal of Geophysical Research (Space Physics)*, 127(2):e29820.

[Artemyev et al., 2015] Artemyev, A. V., Vasiliev, A. A., Mourenas, D., Neishtadt, A. I., Agapitov, O. V., and Krasnoselskikh, V. (2015). Probability of relativistic electron trapping by parallel and oblique whistler-mode waves in Earth's radiation belts. *Physics of Plasmas*, 22(11):112903.

[Artemyev et al., 2019c] Artemyev, A. V., Vasiliev, A. A., and Neishtadt, A. I. (2019c). Charged particle nonlinear resonance with localized electrostatic wave-packets. *Communications in Nonlinear Science and Numerical Simulations*, 72:392–406.

[Artemyev et al., 2022c] Artemyev, A. V., Zhang, X. J., Zou, Y., Mourenas, D., Angelopoulos, V., Vainchtein, D., Tsai, E., and Wilkins, C. (2022c). On the Nature of Intense Sub-Relativistic Electron Precipitation. *Journal of Geophysical Research (Space Physics)*, 127(6):e30571.

[Auster et al., 2008] Auster, H. U., Glassmeier, K. H., Magnes, W., Aydogar, O., Baumjohann, W., Constantinescu, D., Fischer, D., Fornacon, K. H., Georgescu, E., Harvey, P., Hillenmaier, O., Kroth, R., Ludlam, M., Narita, Y., Nakamura, R., Okrafka, K., Plaschke, F., Richter, I., Schwarzl, H., Stoll, B., Valavanoglou, A., and Wiedemann, M. (2008). The THEMIS Fluxgate Magnetometer. *Space Sci. Rev.*, 141:235–264.

[Balikhin et al., 2005] Balikhin, M., Walker, S., Treumann, R., Alleyne, H., Krasnoselskikh, V., Gedalin, M., Andre, M., Dunlop, M., and Fazakerley, A. (2005). Ion sound wave packets at the quasiperpendicular shock front. *Geophys. Res. Lett.*, 32(24):L24106.

[Ball and Melrose, 2001] Ball, L. and Melrose, D. B. (2001). Shock Drift Acceleration of Electrons. , 18(4):361–373.

[Balogh and Treumann, 2013] Balogh, A. and Treumann, R. A. (2013). Physics of Collisionless Shocks: Space Plasma Shock Waves. 12.

[Benkadda et al., 1996] Benkadda, S., Sen, A., and Shklyar, D. R. (1996). Chaotic dynamics of charged particles in the field of two monochromatic waves in a magnetized plasma. *Chaos*, 6(3):451–460.

[Blandford and Eichler, 1987] Blandford, R. and Eichler, D. (1987). Particle acceleration at astrophysical shocks: A theory of cosmic ray origin. , 154(1):1–75.

[Blandford and Ostriker, 1978] Blandford, R. D. and Ostriker, J. P. (1978). Particle acceleration by astrophysical shocks. *Astrophys. J. Lett.*, 221:L29–L32.

[Bonnell et al., 2008] Bonnell, J. W., Mozer, F. S., Delory, G. T., Hull, A. J., Ergun, R. E., Cully, C. M., Angelopoulos, V., and Harvey, P. R. (2008). The Electric Field Instrument (EFI) for THEMIS. *Space Sci. Rev.*, 141:303–341.

[Borovsky et al., 2017] Borovsky, J. E., Horne, R. B., and Meredith, N. P. (2017). The Contribution of Compressional Magnetic Pumping to the Energization of the Earth's Outer Electron Radiation Belt During High-Speed Stream-Driven Storms. *Journal of Geophysical Research (Space Physics)*, 122(12):12,072–12,089.

[Bortnik and Thorne, 2007] Bortnik, J. and Thorne, R. M. (2007). The dual role of ELF/VLF chorus waves in the acceleration and precipitation of radiation belt electrons. *Journal of Atmospheric and Solar-Terrestrial Physics*, 69:378–386.

[Bortnik et al., 2008] Bortnik, J., Thorne, R. M., and Inan, U. S. (2008). Nonlinear interaction of energetic electrons with large amplitude chorus. *Geophys. Res. Lett.*, 35:21102.

[Bortnik et al., 2015] Bortnik, J., Thorne, R. M., Ni, B., and Li, J. (2015). Analytical approximation of transit time scattering due to magnetosonic waves. *Geophys. Res. Lett.*, 42:1318–1325.

[Burch et al., 2016] Burch, J. L., Moore, T. E., Torbert, R. B., and Giles, B. L. (2016). Magnetospheric Multiscale Overview and Science Objectives. *Space Sci. Rev.*, 199:5–21.

[Burtis and Helliwell, 1969] Burtis, W. J. and Helliwell, R. A. (1969). Banded chorusA new type of VLF radiation observed in the magnetosphere by OGO 1 and OGO 3. *J. Geophys. Res.*, 74:3002.

[Bykov et al., 2017] Bykov, A. M., Ellison, D. C., and Osipov, S. M. (2017). Nonlinear Monte Carlo model of superdiffusive shock acceleration with magnetic field amplification. *Phys. Rev. E* , 95(3):033207.

[Chaston et al., 2012] Chaston, C. C., Bonnell, J. W., Clausen, L., and Angelopoulos, V. (2012). Energy transport by kinetic-scale electromagnetic waves in fast plasma sheet flows. *J. Geophys. Res.*, 117:9202.

[Chen et al., 2013] Chen, L., Thorne, R. M., Li, W., and Bortnik, J. (2013). Modeling the wave normal distribution of chorus waves. *J. Geophys. Res.*, 118:1074–1088.

[Chernikov et al., 1992] Chernikov, A. A., Schmidt, G., and Neishtadt, A. I. (1992). Unlimited particle acceleration by waves in a magnetic field. *Physical Review Letters*, 68:1507–1510.

[Chu et al., 2017a] Chu, C., Zhang, H., Sibeck, D., Otto, A., Zong, Q., Omidi, N., McFadden, J. P., Fruehauff, D., and Angelopoulos, V. (2017a). THEMIS satellite observations of hot flow anomalies at Earth's bow shock. *Annales Geophysicae*, 35(3):443–451.

[Chu et al., 2017b] Chu, C., Zhang, H., Sibeck, D., Otto, A., Zong, Q., Omidi, N., McFadden, J. P., Fruehauff, D., and Angelopoulos, V. (2017b). THEMIS satellite observations of hot flow anomalies at Earth's bow shock. *Annales Geophysicae*, 35(3):443–451.

[Collinson et al., 2015] Collinson, G., Halekas, J., Grebowsky, J., Connerney, J., Mitchell, D., Espley, J., DiBraccio, G., Mazelle, C., Sauvaud, J.-A., Fedorov, A., and Jakosky, B. (2015). A hot flow anomaly at Mars. *Geophys. Res. Lett.*, 42(21):9121–9127.

[Cornwall et al., 1970] Cornwall, J. M., Coroniti, F. V., and Thorne, R. M. (1970). Turbulent loss of ring current protons. *J. Geophys. Res.*, 75:4699.

[Davis et al., 2021] Davis, L. A., Cattell, C. A., Wilson, L. B., I., Cohen, Z. A., Breneman, A. W., and Hanson, E. L. M. (2021). ARTEMIS Observations of Plasma Waves in Laminar and Perturbed Interplanetary Shocks. *Astrophys. J.* , 913(2):144.

[Demekhov et al., 2006] Demekhov, A. G., Trakhtengerts, V. Y., Rycroft, M. J., and Nunn, D. (2006). Electron acceleration in the magnetosphere by whistler-mode waves of varying frequency. *Geomagnetism and Aeronomy*, 46:711–716.

[Dresing et al., 2016] Dresing, N., Theesen, S., Klassen, A., and Heber, B. (2016). Efficiency of particle acceleration at interplanetary shocks: Statistical study of STEREO observations. *Astronomy and Astrophysics*, 588:A17.

[Drummond and Pines, 1962] Drummond, W. E. and Pines, D. (1962). Nonlinear stability of plasma oscillations. *Nuclear Fusion Suppl.*, 3:1049–1058.

[Eastwood et al., 2005] Eastwood, J. P., Lucek, E. A., Mazelle, C., Meziane, K., Narita, Y., Pickett, J., and Treumann, R. A. (2005). The Foreshock. *Space Sci. Rev.*, 118(1-4):41–94.

[Egedal et al., 2018] Egedal, J., Le, A., Daughton, W., Wetherton, B., Cassak, P. A., Burch, J. L., Lavraud, B., Dorelli, J., Gershman, D. J., and Avanov, L. A. (2018). Spacecraft Observations of Oblique Electron Beams Breaking the Frozen-In Law During Asymmetric Reconnection. *Phys. Rev. Lett.*, 120(5):055101.

[Egedal and Lichko, 2021] Egedal, J. and Lichko, E. (2021). The fast transit-time limit of magnetic pumping with trapped electrons. *Journal of Plasma Physics*, 87(6):905870610.

[Egedal et al., 2021] Egedal, J., Schroeder, J., and Lichko, E. (2021). Parallel velocity mixing yielding enhanced electron heating during magnetic pumping. *Journal of Plasma Physics*, 87(2):905870116.

[Erickson and Wolf, 1980] Erickson, G. M. and Wolf, R. A. (1980). Is steady convection possible in the earth's magnetotail. *Geophys. Res. Lett.*, 7:897–900.

[Fennell et al., 2015] Fennell, J. F., Claudepierre, S. G., Blake, J. B., O'Brien, T. P., Clemmons, J. H., Baker, D. N., Spence, H. E., and Reeves, G. D. (2015). Van Allen Probes show that the inner radiation zone contains no MeV electrons: ECT/MagEIS data. *Geophys. Res. Lett.*, 42(5):1283–1289.

[Fiuza et al., 2020] Fiuza, F., Swadling, G. F., Grassi, A., Rinderknecht, H. G., Higginson, D. P., Ryutov, D. D., Bruulsema, C., Drake, R. P., Funk, S., Glenzer, S., Gregori, G., Li, C. K., Pollock, B. B., Remington, B. A., Ross, J. S., Rozmus, W., Sakawa, Y., Spitkovsky, A., Wilks, S., and Park, H. S. (2020). Electron acceleration in laboratory-produced turbulent collisionless shocks. *Nature Physics*, 16(9):916–920.

[Foster et al., 2021] Foster, J. C., Erickson, P. J., and Omura, Y. (2021). Subpacket structure in strong VLF chorus rising tones: characteristics and consequences for relativistic electron acceleration. *Earth, Planets and Space*, 73(1):140.

[Frantsuzov et al., 2022] Frantsuzov, V. A., Artemyev, A. V., Shustov, P. I., and Zhang, X. J. (2022). Marginal stability of whistler-mode waves in plasma with multiple electron populations. *Physics of Plasmas*, 29(5):052901.

[Frantsuzov et al., 2023] Frantsuzov, V. A., Artemyev, A. V., Zhang, X.-J., Allanson, O., Shustov, P. I., and Petrukovich, A. A. (2023). Diffusive scattering of energetic electrons by intense whistler-mode waves in an inhomogeneous plasma. *Journal of Plasma Physics*, 89(1):905890101.

[Fu et al., 2014] Fu, X., Cowee, M. M., Friedel, R. H., Funsten, H. O., Gary, S. P., Hospodarsky, G. B., Kletzing, C., Kurth, W., Larsen, B. A., Liu, K., MacDonald, E. A., Min, K., Reeves, G. D., Skoug, R. M., and Winske, D. (2014). Whistler anisotropy instabilities as the source of banded chorus: Van Allen Probes observations and particle-in-cell simulations. *Journal of Geophysical Research (Space Physics)*, 119:8288–8298.

[Furuya et al., 2008] Furuya, N., Omura, Y., and Summers, D. (2008). Relativistic turning acceleration of radiation belt electrons by whistler mode chorus. *J. Geophys. Res.*, 113:4224.

[Gan et al., 2020a] Gan, L., Li, W., Ma, Q., Albert, J. M., Artemyev, A. V., and Bortnik, J. (2020a). Nonlinear Interactions Between Radiation Belt Electrons and Chorus Waves: Dependence on Wave Amplitude Modulation. *Geophys. Res. Lett.*, 47(4):e85987.

[Gan et al., 2020b] Gan, L., Li, W., Ma, Q., Artemyev, A. V., and Albert, J. M. (2020b). Unraveling the Formation Mechanism for the Bursts of Electron Butterfly Distributions: Test Particle and Quasilinear Simulations. *Geophys. Res. Lett.*, 47(21):e90749.

[Gan et al., 2022] Gan, L., Li, W., Ma, Q., Artemyev, A. V., and Albert, J. M. (2022). Dependence of Nonlinear Effects on Whistler-Mode Wave Bandwidth and Amplitude: A Perspective From Diffusion Coefficients. *Journal of Geophysical Research (Space Physics)*, 127(5):e30063.

[Gary, 2005] Gary, S. P. (2005). *Theory of Space Plasma Microinstabilities, Cambridge Atmospheric and Space*. Cambridge University Press.

[Gary and Feldman, 1977] Gary, S. P. and Feldman, W. C. (1977). Solar wind heat flux regulation by the whistler instability. *J. Geophys. Res.*, 82(7):1087.

[Gedalin, 1996] Gedalin, M. (1996). Ion reflection at the shock front revisited. *J. Geophys. Res.*, 101:4871–4878.

[Gedalin, 2015] Gedalin, M. (2015). Collisionless relaxation of non-gyrotropic downstream ion distributions: dependence on shock parameters. *Journal of Plasma Physics*, 81(6):905810603.

[Gedalin, 2020] Gedalin, M. (2020). Large-scale versus Small-scale Fields in the Shock Front: Effect on the Particle Motion. *Astrophys. J.* , 895(1):59.

[Giacalone, 2005] Giacalone, J. (2005). Particle Acceleration at Shocks Moving through an Irregular Magnetic Field. *Astrophys. J.* , 624(2):765–772.

[Glauert and Horne, 2005] Glauert, S. A. and Horne, R. B. (2005). Calculation of pitch angle and energy diffusion coefficients with the PADIE code. *J. Geophys. Res.*, 110:4206.

[Goodrich and Scudder, 1984] Goodrich, C. C. and Scudder, J. D. (1984). The adiabatic energy change of plasma electrons and the frame dependence of the cross-shock potential at collisionless magnetosonic shock waves. *J. Geophys. Res.*, 89(A8):6654–6662.

[Gu et al., 2021] Gu, W., Chen, L., Xia, Z., and Horne, R. B. (2021). Direct Evidence Reveals Transmitter Signal Propagation in the Magnetosphere. *Geophys. Res. Lett.*, 48(15):e93987.

[Gurnett and Bhattacharjee, 2005] Gurnett, D. A. and Bhattacharjee, A. (2005). *Introduction to Plasma Physics*.

[Hietala et al., 2012] Hietala, H., Sandroos, A., and Vainio, R. (2012). Particle Acceleration in Shock-Shock Interaction: Model to Data Comparison. *Astrophys. J. Lett.*, 751(1):L14.

[Hiraga and Omura, 2020] Hiraga, R. and Omura, Y. (2020). Acceleration mechanism of radiation belt electrons through interaction with multi-subpacket chorus waves. *Earth, Planets, and Space*, 72(1):21.

[Hobara et al., 2007] Hobara, Y., Walker, S. N., Balikhin, M., Pokhotelov, O. A., Dunlop, M., Nilsson, H., and RèMe, H. (2007). Characteristics of terrestrial foreshock ULF waves: Cluster observations. *Journal of Geophysical Research (Space Physics)*, 112(A7):A07202.

[Hoppe and Russell, 1980] Hoppe, M. and Russell, C. T. (1980). Whistler mode wave packets in the earth's foreshock region. *Nature*, 287:417–420.

[Horne and Thorne, 1998] Horne, R. B. and Thorne, R. M. (1998). Potential waves for relativistic electron scattering and stochastic acceleration during magnetic storms. *Geophys. Res. Lett.*, 25:3011–3014.

[Hsieh and Omura, 2017] Hsieh, Y.-K. and Omura, Y. (2017). Nonlinear dynamics of electrons interacting with oblique whistler mode chorus in the magnetosphere. *J. Geophys. Res.*, 122:675–694.

[Huang et al., 2018] Huang, S. Y., Sahraoui, F., Yuan, Z. G., Le Contel, O., Breuillard, H., He, J. S., Zhao, J. S., Fu, H. S., Zhou, M., Deng, X. H., Wang, X. Y., Du, J. W., Yu, X. D., Wang, D. D., Pollock, C. J., Torbert, R. B., and Burch, J. L. (2018). Observations of Whistler Waves Correlated with Electron-scale Coherent Structures in the Magnetosheath Turbulent Plasma. *Astrophys. J.* , 861(1):29.

[Hull et al., 2020] Hull, A. J., Muschietti, L., Le Contel, O., Dorelli, J. C., and Lindqvist, P. A. (2020). MMS Observations of Intense Whistler Waves Within Earth's Supercritical Bow Shock: Source Mechanism and Impact on Shock Structure and Plasma Transport. *Journal of Geophysical Research (Space Physics)*, 125(7):e27290.

[Hull et al., 2012] Hull, A. J., Muschietti, L., Oka, M., Larson, D. E., Mozer, F. S., Chaston, C. C., Bonnell, J. W., and Hospodarsky, G. B. (2012). Multiscale whistler waves within Earth's perpendicular bow shock. *J. Geophys. Res.*, 117:12104.

[Inan and Bell, 1977] Inan, U. S. and Bell, T. F. (1977). The plasmapause as a VLF wave guide. *J. Geophys. Res.*, 82:2819–2827.

[Itin et al., 2000] Itin, A. P., Neishtadt, A. I., and Vasiliev, A. A. (2000). Captures into resonance and scattering on resonance in dynamics of a charged relativistic particle in magnetic field and electrostatic wave. *Physica D: Nonlinear Phenomena*, 141:281–296.

[Jiang et al., 2022] Jiang, W., Verscharen, D., Li, H., Wang, C., and Klein, K. G. (2022). Whistler Waves as a Signature of Converging Magnetic Holes in Space Plasmas. *Astrophys. J.* , 935(2):169.

[Jones and Ellison, 1991] Jones, F. C. and Ellison, D. C. (1991). The plasma physics of shock acceleration. *Space Sci. Rev.*, 58(1):259–346.

[Jordanova et al., 2012] Jordanova, V. K., Welling, D. T., Zaharia, S. G., Chen, L., and Thorne, R. M. (2012). Modeling ring current ion and electron dynamics and plasma instabilities during a high-speed stream driven storm. *J. Geophys. Res.*, 117:A00L08.

[Kamaletdinov et al., 2022] Kamaletdinov, S. R., Vasko, I. Y., Wang, R., Artemyev, A. V., Yushkov, E. V., and Mozer, F. S. (2022). Slow electron holes in the Earth's bow shock. *Physics of Plasmas*, 29(9):092303.

[Karpman, 1974] Karpman, V. I. (1974). Nonlinear Effects in the ELF Waves Propagating along the Magnetic Field in the Magnetosphere. *Space Sci. Rev.*, 16:361–388.

[Karpman et al., 1975] Karpman, V. I., Istomin, I. N., and Shkliar, D. R. (1975). Effects of nonlinear interaction of monochromatic waves with resonant particles in the inhomogeneous plasma. *Physica Scripta*, 11:278–284.

[Karpman et al., 1974] Karpman, V. I., Istomin, J. N., and Shklyar, D. R. (1974). Nonlinear theory of a quasi-monochromatic whistler mode packet in inhomogeneous plasma. *Plasma Physics*, 16:685–703.

[Katou and Amano, 2019] Katou, T. and Amano, T. (2019). Theory of Stochastic Shock Drift Acceleration for Electrons in the Shock Transition Region. *Astrophys. J.* , 874(2):119.

[Kennel, 1966] Kennel, C. F. (1966). Low-Frequency Whistler Mode. *Physics of Fluids*, 9:2190–2202.

[Kennel, 1969] Kennel, C. F. (1969). Consequences of a magnetospheric plasma. *Reviews of Geophysics and Space Physics*, 7:379–419.

[Kennel and Engelmann, 1966] Kennel, C. F. and Engelmann, F. (1966). Velocity Space Diffusion from Weak Plasma Turbulence in a Magnetic Field. *Physics of Fluids*, 9:2377–2388.

[Kennel and Petschek, 1966] Kennel, C. F. and Petschek, H. E. (1966). Limit on Stably Trapped Particle Fluxes. *J. Geophys. Res.*, 71:1–28.

[Khazanov et al., 2013] Khazanov, G. V., Tel'nikhin, A. A., and Kronberg, T. K. (2013). Radiation belt electron dynamics driven by large-amplitude whistlers. *Journal of Geophysical Research (Space Physics)*, 118(10):6397–6404.

[Khazanov et al., 2014] Khazanov, G. V., Tel'nikhin, A. A., and Kronberg, T. K. (2014). Stochastic electron motion driven by space plasma waves. *Nonlinear Processes in Geophysics*, 21(1):61–85.

[Kirk and Schneider, 1987] Kirk, J. G. and Schneider, P. (1987). Particle Acceleration at Shocks: A Monte Carlo Method. *Astrophys. J.* , 322:256.

[Kitahara and Katoh, 2019] Kitahara, M. and Katoh, Y. (2019). Anomalous Trapping of Low Pitch Angle Electrons by Coherent Whistler Mode Waves. *J. Geophys. Res.*, 124(7):5568–5583.

[Kivelson and Pu, 1984] Kivelson, M. G. and Pu, Z. Y. (1984). The Kelvin-Helmholtz instability on the magnetopause. *Plan. Sp. Sci.*, 32(11):1335–1341.

[Kletzing et al., 2013] Kletzing, C. A., Kurth, W. S., Acuna, M., MacDowall, R. J., Torbert, R. B., Averkamp, T., Bodet, D., Bounds, S. R., Chutter, M., Connerney, J., Crawford, D., Dolan, J. S., Dvorsky, R., Hospodarsky, G. B., Howard, J., Jordanova, V., Johnson, R. A., Kirchner, D. L., Mokrzycki, B., Needell, G., Odom, J., Mark, D., Pfaff, R., Phillips, J. R., Piker, C. W., Remington, S. L., Rowland, D., Santolik, O., Schnurr, R., Sheppard, D., Smith, C. W., Thorne, R. M., and Tyler, J. (2013). The Electric and Magnetic Field Instrument Suite and Integrated Science (EMFISIS) on RBSP. *Space Sci. Rev.*, 179:127–181.

[Koons and Roeder, 1990] Koons, H. C. and Roeder, J. L. (1990). A survey of equatorial magnetospheric wave activity between 5 and 8 R(E). *Plan. Sp. Sci.*, 38:1335–1341.

[Koyama et al., 1995] Koyama, K., Petre, R., Gotthelf, E. V., Hwang, U., Matsuura, M., Ozaki, M., and Holt, S. S. (1995). Evidence for shock acceleration of high-energy electrons in the supernova remnant SN1006. *Nature*, 378(6554):255–258.

[Kozyra et al., 1997] Kozyra, J. U., Jordanova, V. K., Home, R. B., and Thorne, R. M. (1997). Modeling of the contribution of electromagnetic ion cyclotron (EMIC) waves to stormtime ring current erosion. *Washington DC American Geophysical Union Geophysical Monograph Series*, 98:187–202.

[Krasnoselskikh et al., 2013] Krasnoselskikh, V., Balikhin, M., Walker, S. N., Schwartz, S., Sundkvist, D., Lobzin, V., Gedalin, M., Bale, S. D., Mozer, F., Soucek, J., Hobara, Y., and Comisel, H. (2013). The Dynamic Quasiperpendicular Shock: Cluster Discoveries. *Space Sci. Rev.*, 178:535–598.

[Krauss-Varban et al., 1994] Krauss-Varban, D., Omidi, N., and Quest, K. B. (1994). Mode properties of low-frequency waves: Kinetic theory versus Hall-MHD. *J. Geophys. Res.*, 99(A4):5987–6010.

[Kruparova et al., 2019] Kruparova, O., Krupar, V., Å afránková, J., Němeček, Z., Maksimovic, M., Santolik, O., Soucek, J., Němec, F., and Merka, J. (2019). Statistical Survey of the Terrestrial Bow Shock Observed by the Cluster Spacecraft. *Journal of Geophysical Research (Space Physics)*, 124(3):1539–1547.

[Kunz et al., 2011] Kunz, M. W., Schekochihin, A. A., Cowley, S. C., Binney, J. J., and Sanders, J. S. (2011). A thermally stable heating mechanism for the intracluster medium: turbulence, magnetic fields and plasma instabilities. *Monthly Notices of the Royal Astronomical Society*, 410(4):2446–2457.

[Kuramitsu and Krasnoselskikh, 2005] Kuramitsu, Y. and Krasnoselskikh, V. (2005). Gyroresonant Surfing Acceleration. *Physical Review Letters*, 94(3):031102–+.

[Lalti et al., 2022a] Lalti, A., Khotyaintsev, Y. V., Dimmock, A. P., Johlander, A., Graham, D. B., and Olshevsky, V. (2022a). A Database of MMS Bow Shock Crossings Compiled Using Machine Learning. *Journal of Geophysical Research (Space Physics)*, 127(8):e30454.

[Lalti et al., 2023] Lalti, A., Khotyaintsev, Y. V., and Graham, D. B. (2023). Short-Wavelength Electrostatic Wave Measurement Using MMS Spacecraft. *Journal of Geophysical Research (Space Physics)*, 128(4):e2022JA031150.

[Lalti et al., 2022b] Lalti, A., Khotyaintsev, Y. V., Graham, D. B., Vaivads, A., Steinvall, K., and Russell, C. T. (2022b). Whistler Waves in the Foot of Quasi-Perpendicular Supercritical Shocks. *Journal of Geophysical Research (Space Physics)*, 127(5):e29969.

[Le Contel et al., 2016] Le Contel, O., Retinò, A., Breuillard, H., Mirioni, L., Robert, P., Chasapis, A., Lavraud, B., Chust, T., Rezeau, L., Wilder, F. D., Graham, D. B., Argall, M. R., Gershman, D. J., Lindqvist, P.-A., Khotyaintsev, Y. V., Marklund, G., Ergun, R. E., Goodrich, K. A., Burch, J. L., Torbert, R. B., Needell, J., Chutter, M., Rau, D., Dors, I., Russell, C. T., Magnes, W., Strangeway, R. J., Bromund, K. R., Leinweber, H. K., Plaschke, F., Fischer, D., Anderson, B. J., Le, G., Moore, T. E., Pollock, C. J., Giles, B. L., Dorelli, J. C., Avanov, L., and Saito, Y. (2016). Whistler mode waves and Hall fields detected by MMS during a dayside magnetopause crossing. *Geophys. Res. Lett.*, 43:5943–5952.

[Le Queau and Roux, 1987] Le Queau, D. and Roux, A. (1987). Quasi-monochromatic wave-particle interactions in magnetospheric plasmas. *Solar Physics*, 111:59–80.

[Leroy et al., 1982] Leroy, M. M., Winske, D., Goodrich, C. C., Wu, C. S., and Papadopoulos, K. (1982). The structure of perpendicular bow shocks. *J. Geophys. Res.*, 87(A7):5081–5094.

[Ley et al., 2023] Ley, F., Zweibel, E. G., Riquelme, M., Sironi, L., Miller, D., and Tran, A. (2023). A Heating Mechanism via Magnetic Pumping in the Intracluster Medium. *Astrophys. J.* , 947(2):89.

[Li and Hudson, 2019] Li, W. and Hudson, M. K. (2019). Earth's Van Allen Radiation Belts: From Discovery to the Van Allen Probes Era. *Journal of Geophysical Research (Space Physics)*, 124(11):8319–8351.

[Li et al., 2016] Li, W., Mourenas, D., Artemyev, A. V., Bortnik, J., Thorne, R. M., Kletzing, C. A., Kurth, W. S., Hospodarsky, G. B., Reeves, G. D., Funsten, H. O., and Spence, H. E. (2016). Unraveling the excitation mechanisms of highly oblique lower band chorus waves. *Geophys. Res. Lett.*, 43:8867–8875.

[Li et al., 2008] Li, W., Thorne, R. M., Meredith, N. P., Horne, R. B., Bortnik, J., Shprits, Y. Y., and Ni, B. (2008). Evaluation of whistler mode chorus amplification during an injection event observed on CRRES. *J. Geophys. Res.*, 113:9210.

[Lichko and Egedal, 2020] Lichko, E. and Egedal, J. (2020). Magnetic pumping model for energizing superthermal particles applied to observations of the Earth's bow shock. *Nature Communications*, 11:2942.

[Lichko et al., 2017] Lichko, E., Egedal, J., Daughton, W., and Kasper, J. (2017). Magnetic Pumping as a Source of Particle Heating and Power-law Distributions in the Solar Wind. *Astrophys. J. Lett.*, 850:L28.

[Lin, 1997] Lin, Y. (1997). Generation of anomalous flows near the bow shock by its interaction with interplanetary discontinuities. *J. Geophys. Res.*, 102(A11):24265–24282.

[Lin, 2002] Lin, Y. (2002). Global hybrid simulation of hot flow anomalies near the bow shock and in the magnetosheath. *Plan. Sp. Sci.*, 50(5-6):577–591.

[Lin et al., 2022] Lin, Y., Wang, X., Sibeck, D. G., Wang, C.-P., and Lee, S.-H. (2022). Global Asymmetries of Hot Flow Anomalies. *Geophys. Res. Lett.*, 49(4):e96970.

[Liu et al., 2017a] Liu, T. Z., Angelopoulos, V., Hietala, H., and Wilson, Lynn B., I. (2017a). Statistical study of particle acceleration in the core of foreshock transients. *Journal of Geophysical Research (Space Physics)*, 122(7):7197–7208.

[Liu et al., 2019] Liu, T. Z., Angelopoulos, V., and Lu, S. (2019). Relativistic electrons generated at Earth's quasi-parallel bow shock. *Science Advances*, 5(7):eaaw1368.

[Liu et al., 2017b] Liu, T. Z., Lu, S., Angelopoulos, V., Hietala, H., and Wilson, L. B. (2017b). Fermi acceleration of electrons inside foreshock transient cores. *Journal of Geophysical Research (Space Physics)*, 122(9):9248–9263.

[Liu et al., 2018] Liu, T. Z., Lu, S., Angelopoulos, V., Lin, Y., and Wang, X. Y. (2018). Ion Acceleration Inside Foreshock Transients. *Journal of Geophysical Research (Space Physics)*, 123(1):163–178.

[Liu et al., 2016] Liu, T. Z., Turner, D. L., Angelopoulos, V., and Omidi, N. (2016). Multipoint observations of the structure and evolution of foreshock bubbles and their relation to hot flow anomalies. *Journal of Geophysical Research*, 121(6):5489–5509.

[Lorentzen et al., 2001] Lorentzen, K. R., Blake, J. B., Inan, U. S., and Bortnik, J. (2001). Observations of relativistic electron microbursts in association with VLF chorus. *J. Geophys. Res.*, 106(A4):6017–6028.

[Lu et al., 2022] Lu, X., Zhang, H., Liu, T., Vu, A., Pollock, C., and Wang, B. (2022). Statistical Study of Foreshock Density Holes. *Journal of Geophysical Research (Space Physics)*, 127(4):e29981.

[Lukin et al., 2021] Lukin, A. S., Artemyev, A. V., and Petrukovich, A. A. (2021). On application of stochastic differential equations for simulation of nonlinear wave-particle resonant interactions. *Physics of Plasmas*, 28(9):092904.

[Lyons, 1974] Lyons, L. R. (1974). Pitch angle and energy diffusion coefficients from resonant interactions with ion-cyclotron and whistler waves. *Journal of Plasma Physics*, 12:417–432.

[Lyons et al., 1972] Lyons, L. R., Thorne, R. M., and Kennel, C. F. (1972). Pitch-angle diffusion of radiation belt electrons within the plasmasphere. *J. Geophys. Res.*, 77:3455–3474.

[Lyons and Williams, 1984] Lyons, L. R. and Williams, D. J. (1984). *Quantitative aspects of magnetospheric physics.*

[Malaspina et al., 2018] Malaspina, D. M., Ukhorskiy, A., Chu, X., and Wygant, J. (2018). A Census of Plasma Waves and Structures Associated With an Injection Front in the Inner Magnetosphere. *J. Geophys. Res.*, 123:2566–2587.

[Malaspina et al., 2015] Malaspina, D. M., Wygant, J. R., Ergun, R. E., Reeves, G. D., Skoug, R. M., and Larsen, B. A. (2015). Electric field structures and waves at plasma boundaries in the inner magnetosphere. *J. Geophys. Res.*, 120:n/a–n/a. 2015JA021137.

[Masters et al., 2013] Masters, A., Stawarz, L., Fujimoto, M., Schwartz, S. J., Sergis, N., Thomsen, M. F., Retinò, A., Hasegawa, H., Zieger, B., Lewis, G. R., Coates, A. J., Canu, P., and Dougherty, M. K. (2013). Electron acceleration to relativistic energies at a strong quasi-parallel shock wave. *Nature Physics*, 9:164–167.

[Masters et al., 2016] Masters, A., Sulaiman, A. H., Sergis, N., Stawarz, L., Fujimoto, M., Coates, A. J., and Dougherty, M. K. (2016). Suprathermal Electrons at Saturn's Bow Shock. *Astrophys. J.* , 826(1):48.

[McFadden et al., 2008] McFadden, J. P., Carlson, C. W., Larson, D., Ludlam, M., Abiad, R., Elliott, B., Turin, P., Marckwordt, M., and Angelopoulos, V. (2008). The THEMIS ESA Plasma Instrument and In-flight Calibration. *Space Sci. Rev.*, 141:277–302.

[Meredith et al., 2001] Meredith, N. P., Horne, R. B., and Anderson, R. R. (2001). Substorm dependence of chorus amplitudes: Implications for the acceleration of electrons to relativistic energies. *J. Geophys. Res.*, 106:13165–13178.

[Meredith et al., 2013] Meredith, N. P., Horne, R. B., Bortnik, J., Thorne, R. M., Chen, L., Li, W., and Sicard-Piet, A. (2013). Global statistical evidence for chorus as the embryonic source of plasmaspheric hiss. *Geophys. Res. Lett.*, 40:2891–2896.

[Meredith et al., 2007] Meredith, N. P., Horne, R. B., Glauert, S. A., and Anderson, R. R. (2007). Slot region electron loss timescales due to plasmaspheric hiss and lightning-generated whistlers. *J. Geophys. Res.*, 112:8214.

[Meredith et al., 2018] Meredith, N. P., Horne, R. B., Kersten, T., Li, W., Bortnik, J., Sicard, A., and Yearby, K. H. (2018). Global Model of Plasmaspheric Hiss From Multiple Satellite Observations. *Journal of Geophysical Research (Space Physics)*, 123(6):4526–4541.

[Meredith et al., 2004] Meredith, N. P., Horne, R. B., Thorne, R. M., Summers, D., and Anderson, R. R. (2004). Substorm dependence of plasmaspheric hiss. *J. Geophys. Res.*, 109:6209.

[Millan and Baker, 2012] Millan, R. M. and Baker, D. N. (2012). Acceleration of Particles to High Energies in Earth's Radiation Belts. *Space Sci. Rev.*, 173:103–131.

[Montag and Howes, 2022] Montag, P. and Howes, G. G. (2022). A field-particle correlation analysis of magnetic pumping. *Physics of Plasmas*, 29(3):032901.

[Mourenas et al., 2012] Mourenas, D., Artemyev, A., Agapitov, O., and Krasnoselskikh, V. (2012). Acceleration of radiation belts electrons by oblique chorus waves. *J. Geophys. Res.*, 117:10212.

[Mourenas et al., 2018] Mourenas, D., Zhang, X.-J., Artemyev, A. V., Angelopoulos, V., Thorne, R. M., Bortnik, J., Neishtadt, A. I., and Vasiliev, A. A. (2018). Electron Nonlinear Resonant Interaction With Short and Intense Parallel Chorus Wave Packets. *J. Geophys. Res.*, 123:4979–4999.

[Mourenas et al., 2022] Mourenas, D., Zhang, X. J., Nunn, D., Artemyev, A. V., Angelopoulos, V., Tsai, E., and Wilkins, C. (2022). Short Chorus Wave Packets: Generation Within Chorus Elements, Statistics, and Consequences on Energetic Electron Precipitation. *Journal of Geophysical Research (Space Physics)*, 127(5):e30310.

[Mozer et al., 2015] Mozer, F. S., Agapitov, O., Artemyev, A., Drake, J. F., Krasnoselskikh, V., Lejosne, S., and Vasko, I. (2015). Time domain structures: What and where they are, what they do, and how they are made. *Geophys. Res. Lett.*, 42:3627–3638.

[Neishtadt, 1975] Neishtadt, A. I. (1975). Passage through a separatrix in a resonance problem with a slowly-varying parameter. *Journal of Applied Mathematics and Mechanics*, 39:594–605.

[Neishtadt, 2014] Neishtadt, A. I. (2014). Averaging, passage through resonances, and capture into resonance in two-frequency systems. *Russian Mathematical Surveys*, 69(5):771.

[Neishtadt and Vasiliev, 2006] Neishtadt, A. I. and Vasiliev, A. A. (2006). Destruction of adiabatic invariance at resonances in slow fast Hamiltonian systems. *Nuclear Instruments and Methods in Physics Research A*, 561:158–165.

[Ni et al., 2013] Ni, B., Bortnik, J., Thorne, R. M., Ma, Q., and Chen, L. (2013). Resonant scattering and resultant pitch angle evolution of relativistic electrons by plasmaspheric hiss. *J. Geophys. Res.*, 118:7740–7751.

[Ni et al., 2016] Ni, B., Thorne, R. M., Zhang, X., Bortnik, J., Pu, Z., Xie, L., Hu, Z.-j., Han, D., Shi, R., Zhou, C., and Gu, X. (2016). Origins of the Earth's Diffuse Auroral Precipitation. *Space Sci. Rev.*, 200:205–259.

[Nunn, 1971] Nunn, D. (1971). Wave-particle interactions in electrostatic waves in an inhomogeneous medium. *Journal of Plasma Physics*, 6:291.

[Nunn et al., 2021] Nunn, D., Zhang, X. J., Mourenas, D., and Artemyev, A. V. (2021). Generation of Realistic Short Chorus Wave Packets. *Geophys. Res. Lett.*, 48(7):e92178.

[Němec et al., 2005] Němec, F., Santolík, O., Gereová, K., Macúšová, E., de Conchy, Y., and Cornilleau-Wehrlin, N. (2005). Initial results of a survey of equatorial noise emissions observed by the Cluster spacecraft. *Plan. Sp. Sci.*, 53:291–298.

[Oka et al., 2019] Oka, M., Otsuka, F., Matsukiyo, S., Wilson, L. B., I., Argall, M. R., Amano, T., Phan, T. D., Hoshino, M., Le Contel, O., Gershman, D. J., Burch, J. L., Torbert, R. B., Dorelli, J. C., Giles, B. L., Ergun, R. E., Russell, C. T., and Lindqvist, P. A. (2019). Electron Scattering by Low-frequency Whistler Waves at Earth's Bow Shock. *Astrophys. J.* , 886(1):53.

[Oka et al., 2017] Oka, M., Wilson, III, L. B., Phan, T. D., Hull, A. J., Amano, T., Hoshino, M., Argall, M. R., Le Contel, O., Agapitov, O., Gershman, D. J., Khotyaintsev, Y. V., Burch, J. L., Torbert, R. B., Pollock, C., Dorelli, J. C., Giles, B. L., Moore, T. E., Saito, Y., Avanov, L. A., Paterson, W., Ergun, R. E., Strangeway, R. J., Russell, C. T., and Lindqvist, P. A. (2017). Electron Scattering by High-frequency Whistler Waves at Earth's Bow Shock. *Astrophys. J. Lett.*, 842:L11.

[Omidi et al., 2010] Omidi, N., Eastwood, J. P., and Sibeck, D. G. (2010). Foreshock bubbles and their global magnetospheric impacts. *Journal of Geophysical Research (Space Physics)*, 115(A6):A06204.

[Omidi et al., 2009] Omidi, N., Sibeck, D. G., and Blanco-Cano, X. (2009). Foreshock compressional boundary. *Journal of Geophysical Research (Space Physics)*, 114:A08205.

[Omura, 2021] Omura, Y. (2021). Nonlinear wave growth theory of whistler-mode chorus and hiss emissions in the magnetosphere. *Earth, Planets and Space*, 73(1):95.

[Omura et al., 2008] Omura, Y., Katoh, Y., and Summers, D. (2008). Theory and simulation of the generation of whistler-mode chorus. *J. Geophys. Res.*, 113:4223.

[Omura et al., 1991] Omura, Y., Matsumoto, H., Nunn, D., and Rycroft, M. J. (1991). A review of observational, theoretical and numerical studies of VLF triggered emissions. *Journal of Atmospheric and Terrestrial Physics*, 53:351–368.

[Omura et al., 2015] Omura, Y., Miyashita, Y., Yoshikawa, M., Summers, D., Hikishima, M., Ebihara, Y., and Kubota, Y. (2015). Formation process of relativistic electron flux through interaction with chorus emissions in the Earth's inner magnetosphere. *J. Geophys. Res.*, 120:9545–9562.

[O'Neil, 1965] O'Neil, T. (1965). Collisionless Damping of Nonlinear Plasma Oscillations. *Physics of Fluids*, 8:2255–2262.

[Page et al., 2021] Page, B., Vasko, I. Y., Artemyev, A. V., and Bale, S. D. (2021). Generation of High-frequency Whistler Waves in the Earth's Quasi-perpendicular Bow Shock. *Astrophys. J. Lett.*, 919(2):L17.

[Paschmann and Schwartz, 2000a] Paschmann, G. and Schwartz, S. J. (2000a). ISSI Book on Analysis Methods for Multi-Spacecraft Data. In Harris, R. A., editor, *Cluster-II Workshop Multiscale / Multipoint Plasma Measurements*, volume 449 of *ESA Special Publication*, page 99.

[Paschmann and Schwartz, 2000b] Paschmann, G. and Schwartz, S. J. (2000b). ISSI Book on Analysis Methods for Multi-Spacecraft Data. In Harris, R. A., editor, *Cluster-II Workshop Multiscale / Multipoint Plasma Measurements*, volume 449 of *ESA Special Publication*, page 99.

[Peng et al., 2022] Peng, Y., Ma, Q., Li, W., Gan, L., and Shen, X.-C. (2022). Multi-event analysis of the correlation between chorus waves and electron butterfly distribution using van allen probes observation. *Journal of Geophysical Research: Space Physics*, 127(12):e2022JA030806.

[Penz et al., 2004] Penz, T., Erkaev, N. V., Biernat, H. K., Lammer, H., Amerstorfer, U. V., Gunell, H., Kallio, E., Barabash, S., Orsini, S., Milillo, A., and Baumjohann, W. (2004). Ion loss on Mars caused by the Kelvin Helmholtz instability. *Plan. Sp. Sci.*, 52(13):1157–1167.

[Perri et al., 2022] Perri, S., Bykov, A., Fahr, H., Fichtner, H., and Giacalone, J. (2022). Recent Developments in Particle Acceleration at Shocks: Theory and Observations. *Space Sci. Rev.*, 218(4):26.

[Pollock et al., 2016] Pollock, C., Moore, T., Jacques, A., Burch, J., Gliese, U., Saito, Y., Omoto, T., Avanov, L., Barrie, A., Coffey, V., Dorelli, J., Gershman, D., Giles, B., Rosnack, T., Salo, C., Yokota, S., Adrian, M., Aoustin, C., Auletti, C., Aung, S., Bigio, V., Cao, N., Chandler, M., Chornay, D., Christian, K., Clark, G., Collinson, G., Corris, T., De Los Santos, A., Devlin, R., Diaz, T., Dickerson, T., Dickson, C., Diekmann, A., Diggs, F., Duncan, C., Figueroa-Vinas, A., Firman, C., Freeman, M., Galassi, N., Garcia, K., Goodhart, G., Guererro, D., Hageman, J., Hanley, J., Hemminger, E., Holland, M., Hutchins, M., James, T., Jones, W., Kreisler, S., Kujawski, J., Lavu, V., Lobell, J., LeCompte, E., Lukemire, A., MacDonald, E., Mariano, A., Mukai, T., Narayanan, K., Nguyan, Q., Onizuka, M., Paterson, W., Persyn, S., Piepgrass, B., Cheney, F., Rager, A., Raghuram, T., Ramil, A., Reichenthal, L., Rodriguez, H., Rouzaud, J., Rucker, A., Saito, Y., Samara, M., Sauvaud, J.-A., Schuster, D., Shappirio, M., Shelton, K., Sher, D., Smith, D., Smith, K., Smith, S., Steinfeld, D., Szymkiewicz, R., Tanimoto, K., Taylor, J., Tucker, C., Tull, K., Uhl, A., Vloet, J., Walpole, P., Weidner, S., White, D., Winkert, G., Yeh, P.-S., and Zeuch, M. (2016). Fast Plasma Investigation for Magnetospheric Multiscale. *Space Sci. Rev.*, 199:331–406.

[Roux et al., 2008] Roux, A., Le Contel, O., Coillot, C., Bouabdellah, A., de La Porte, B., Alison, D., Ruocco, S., and Vassal, M. C. (2008). The Search Coil Magnetometer for THEMIS. *Space Sci. Rev.*, 141:265–275.

[Russell et al., 2016] Russell, C. T., Anderson, B. J., Baumjohann, W., Bromund, K. R., Dearborn, D., Fischer, D., Le, G., Leinweber, H. K., Leneman, D., Magnes, W., Means, J. D., Moldwin, M. B., Nakamura, R., Pierce, D., Plaschke, F., Rowe, K. M., Slavin, J. A., Strangeway, R. J., Torbert, R., Hagen, C., Jernej, I., Valavanoglou, A., and Richter, I. (2016). The Magnetospheric Multiscale Magnetometers. *Space Sci. Rev.*, 199:189–256.

[Sagdeev and Shafranov, 1961] Sagdeev, R. Z. and Shafranov, V. D. (1961). On the Instability of a Plasma with an Anisotropic Distribution of Velocities in a Magnetic Field. *Soviet Phys. JETP*, 12(1):130–132.

[Saito and Miyoshi, 2022] Saito, S. and Miyoshi, Y. (2022). Butterfly Distribution of Relativistic Electrons Driven by Parallel Propagating Lower Band Whistler Chorus Waves. *Geophys. Res. Lett.*, 49(12):e99605.

[Santolík et al., 2004] Santolík, O., Gurnett, D., and Pickett, J. (2004). Multipoint investigation of the source region of storm-time chorus. *Annales Geophysicae*, 22(7):2555–2563.

[Santolík et al., 2014] Santolík, O., Kletzing, C. A., Kurth, W. S., Hospodarsky, G. B., and Bounds, S. R. (2014). Fine structure of large-amplitude chorus wave packets. *Geophys. Res. Lett.*, 41:293–299.

[Schulz and Lanzerotti, 1974] Schulz, M. and Lanzerotti, L. J. (1974). *Particle diffusion in the radiation belts*. Springer, New York.

[Schwartz et al., 1985] Schwartz, S. J., Chaloner, C. P., Christiansen, P. J., Coates, A. J., Hall, D. S., Johnstone, A. D., Gough, M. P., Norris, A. J., Rijnbeek, R. P., Southwood, D. J., and Woolliscroft, L. J. C. (1985). An active current sheet in the solar wind. *Nature*, 318(6043):269–271.

[Scudder, 1995] Scudder, J. D. (1995). A review of the physics of electron heating at collisionless shocks. *Advances in Space Research*, 15:181–223.

[Shapiro and Sagdeev, 1997] Shapiro, V. D. and Sagdeev, R. Z. (1997). Nonlinear wave-particle interaction and conditions for the applicability of quasilinear theory. *Physics Reports*, 283:49–71.

[Shi et al., 2023a] Shi, X., Artemyev, A., Angelopoulos, V., Liu, T., and Zhang, X.-J. (2023a). Evidence of Electron Acceleration via Nonlinear Resonant Interactions with Whistler-mode Waves at Foreshock Transients. *Astrophys. J.* , 952(1):38.

[Shi et al., 2023b] Shi, X., Liu, T., Artemyev, A., Angelopoulos, V., Zhang, X.-J., and Turner, D. L. (2023b). Intense Whistler-mode Waves at Foreshock Transients: Characteristics and Regimes of Wave-Particle Resonant Interaction. *Astrophys. J.* , 944(2):193.

[Shi et al., 2020] Shi, X., Liu, T. Z., Angelopoulos, V., and Zhang, X.-J. (2020). Whistler Mode Waves in the Compressional Boundary of Foreshock Transients. *Journal of Geophysical Research (Space Physics)*, 125(8):e27758.

[Shi et al., 2023] Shi, X., Tonoian, D. S., Artemyev, A. V., Zhang, X.-J., and Angelopoulos, V. (2023). Electron resonant interaction with whistler-mode waves around the Earth's bow shock I: The probabilistic approach. *Physics of Plasmas*, 30(12):122902.

[Shklyar, 1981] Shklyar, D. R. (1981). Stochastic motion of relativistic particles in the field of a monochromatic wave. *Sov. Phys. JETP*, 53:1197–1192.

[Shklyar, 2011] Shklyar, D. R. (2011). On the nature of particle energization via resonant wave-particle interaction in the inhomogeneous magnetospheric plasma. *Annales Geophysicae*, 29:1179–1188.

[Shklyar, 2021] Shklyar, D. R. (2021). A Theory of Interaction Between Relativistic Electrons and Magnetospherically Reflected Whistlers. *Journal of Geophysical Research (Space Physics)*, 126(2):e28799.

[Shklyar et al., 2004] Shklyar, D. R., Chum, J., and Jirícek, F. (2004). Characteristic properties of Nu whistlers as inferred from observations and numerical modelling. *Annales Geophysicae*, 22:3589–3606.

[Shklyar and Matsumoto, 2009] Shklyar, D. R. and Matsumoto, H. (2009). Oblique Whistler-Mode Waves in the Inhomogeneous Magnetospheric Plasma: Resonant Interactions with Energetic Charged Particles. *Surveys in Geophysics*, 30:55–104.

[Slavin et al., 2007] Slavin, J. A., Krimigis, S. M., Acuña, M. H., Anderson, B. J., Baker, D. N., Koehn, P. L., Korth, H., Livi, S., Mauk, B. H., and Solomon, S. C. (2007). MESSENGER: Exploring Mercury's Magnetosphere. *Space Sci. Rev.*, 131(1-4):133–160.

[Solovev and Shkliar, 1986] Solovev, V. V. and Shkliar, D. R. (1986). Particle heating by a low-amplitude wave in an inhomogeneous magnetoplasma. *Sov. Phys. JETP*, 63:272–277.

[Sonnerup and Cahill, 1968] Sonnerup, B. U. Ö. and Cahill, Jr., L. J. (1968). Explorer 12 observations of the magnetopause current layer. *J. Geophys. Res.*, 73:1757.

[Sonnerup and Scheible, 2000] Sonnerup, B. U. Ö. and Scheible, M. (2000). *ISSI Book on Analysis Methods for Multi-Spacecraft Data*, volume 449 of *ESA Special Publication*.

[Sonnerup and Su, 1967] Sonnerup, B. U. Ö. and Su, S.-Y. (1967). Large Amplitude Whistler Waves in a Hot Collision-Free Plasma. *Physics of Fluids*, 10:462–464.

[Stix, 1962] Stix, T. H. (1962). *The Theory of Plasma Waves*.

[Summers, 2005] Summers, D. (2005). Quasi-linear diffusion coefficients for field-aligned electromagnetic waves with applications to the magnetosphere. *J. Geophys. Res.*, 110:8213.

[Tao et al., 2013] Tao, X., Bortnik, J., Albert, J. M., Thorne, R. M., and Li, W. (2013). The importance of amplitude modulation in nonlinear interactions between electrons and large amplitude whistler waves. *Journal of Atmospheric and Solar-Terrestrial Physics*, 99:67–72.

[Tao et al., 2008] Tao, X., Chan, A. A., Albert, J. M., and Miller, J. A. (2008). Stochastic modeling of multidimensional diffusion in the radiation belts. *Journal of Geophysical Research (Space Physics)*, 113(A7):A07212.

[Tao et al., 2011] Tao, X., Thorne, R. M., Li, W., Ni, B., Meredith, N. P., and Horne, R. B. (2011). Evolution of electron pitch angle distributions following injection from the plasma sheet. *J. Geophys. Res.*, 116:A04229.

[Tao et al., 2020] Tao, X., Zonca, F., Chen, L., and Wu, Y. (2020). Theoretical and numerical studies of chorus waves: A review. *Science China Earth Sciences*, 63(1):78–92.

[Terasawa, 1979] Terasawa, T. (1979). Origin of 30-100 keV protons observed in the upstream region of the earth's bow shock. *Plan. Sp. Sci.*, 27:365–384.

[Thorne, 2010] Thorne, R. M. (2010). Radiation belt dynamics: The importance of wave-particle interactions. *Geophys. Res. Lett.*, 372:22107.

[Thorne et al., 2013] Thorne, R. M., Li, W., Ni, B., Ma, Q., Bortnik, J., Chen, L., Baker, D. N., Spence, H. E., Reeves, G. D., Henderson, M. G., Kletzing, C. A., Kurth, W. S., Hospodarsky, G. B., Blake, J. B., Fennell, J. F., Claudepierre, S. G., and Kanekal, S. G. (2013). Rapid local acceleration of relativistic radiation-belt electrons by magnetospheric chorus. *Nature*, 504:411–414.

[Tokar et al., 1984] Tokar, R. L., Gurnett, D. A., and Feldman, W. C. (1984). Whistler mode turbulence generated by electron beams in earth's bow shock. *J. Geophys. Res.*, 89(A1):105–114.

[Tong et al., 2019a] Tong, Y., Vasko, I. Y., Artemyev, A. V., Bale, S. D., and Mozer, F. S. (2019a). Statistical Study of Whistler Waves in the Solar Wind at 1 au. *Astrophys. J.* , 878(1):41.

[Tong et al., 2019b] Tong, Y., Vasko, I. Y., Pulupa, M., Mozer, F. S., Bale, S. D., Artemyev, A. V., and Krasnoselskikh, V. (2019b). Whistler Wave Generation by Halo Electrons in the Solar Wind. *Astrophys. J. Lett.*, 870(1):L6.

[Trakhtengerts et al., 2003] Trakhtengerts, V. Y., Rycroft, M. J., Nunn, D., and Demekhov, A. G. (2003). Cyclotron acceleration of radiation belt electrons by whistlers. *J. Geophys. Res.*, 108:1138.

[Treumann, 2009] Treumann, R. A. (2009). Fundamentals of collisionless shocks for astrophysical application, 1. Non-relativistic shocks. *The Astronomy and Astrophysics Review*, 17:409–535.

[Tsai et al., 2022] Tsai, E., Artemyev, A., Zhang, X.-J., and Angelopoulos, V. (2022). Relativistic Electron Precipitation Driven by Nonlinear Resonance With Whistler-Mode Waves. *Journal of Geophysical Research (Space Physics)*, 127(5):e30338.

[Turner et al., 2017] Turner, D. L., Lee, J. H., Claudepierre, S. G., Fennell, J. F., Blake, J. B., Jaynes, A. N., Leonard, T., Wilder, F. D., Ergun, R. E., Baker, D. N., Cohen, I. J., Mauk, B. H., Strangeway, R. J., Hartley, D. P., Kletzing, C. A., Breuillard, H., Le Contel, O., Khotyaintsev, Y. V., Torbert, R. B., Allen, R. C., Burch, J. L., and Santolik, O. (2017). Examining Coherency Scales, Substructure, and Propagation of Whistler Mode Chorus Elements With Magnetospheric Multiscale (MMS). *Journal of Geophysical Research (Space Physics)*, 122(11):11,201–11,226.

[Turner et al., 2013] Turner, D. L., Omidi, N., Sibeck, D. G., and Angelopoulos, V. (2013). First observations of foreshock bubbles upstream of Earth's bow shock: Characteristics and comparisons to HFAs. *Journal of Geophysical Research (Space Physics)*, 118(4):1552–1570.

[Turner et al., 2018] Turner, D. L., Wilson, L. B., Liu, T. Z., Cohen, I. J., Schwartz, S. J., Osmane, A., Fennell, J. F., Clemmons, J. H., Blake, J. B., Westlake, J., Mauk, B. H., Jaynes, A. N., Leonard, T., Baker, D. N., Strangeway, R. J., Russell, C. T., Gershman, D. J., Avanov, L., Giles, B. L., Torbert, R. B., Broll, J., Gomez, R. G., Fuselier, S. A., and Burch, J. L. (2018). Autogenous and efficient acceleration of energetic ions upstream of Earth's bow shock. *Nature*, 561(7722):206–210.

[Ucer and Shapiro, 2001] Ucer, D. and Shapiro, V. D. (2001). Unlimited Relativistic Shock Surfing Acceleration. *Physical Review Letters*, 87(7):075001.

[Vainchtein et al., 2018] Vainchtein, D., Zhang, X. J., Artemyev, A. V., Mourenas, D., Angelopoulos, V., and Thorne, R. M. (2018). Evolution of Electron Distribution Driven by Nonlinear Resonances With Intense Field-Aligned Chorus Waves. *Journal of Geophysical Research (Space Physics)*, 123(10):8149–8169.

[van Weeren et al., 2017] van Weeren, R. J., Andrade-Santos, F., Dawson, W. A., Golovich, N., Lal, D. V., Kang, H., Ryu, D., Brìggen, M., Ogrean, G. A., Forman, W. R., Jones, C., Placco, V. M., Santucci, R. M., Wittman, D., Jee, M. J., Kraft, R. P., Sobral, D., Stroe, A., and Fogarty, K. (2017). The case for electron re-acceleration at galaxy cluster shocks. *Nature Astronomy*, 1:0005.

[Vandas, 2001] Vandas, M. (2001). Shock drift acceleration of electrons: A parametric study. *J. Geophys. Res.*, 106(A2):1859–1872.

[Vasko et al., 2018a] Vasko, I. Y., Krasnoselskikh, V. V., Mozer, F. S., and Artemyev, A. V. (2018a). Scattering by the broadband electrostatic turbulence in the space plasma. *Physics of Plasmas*, 25(7):072903.

[Vasko et al., 2020] Vasko, I. Y., Kuzichev, I. V., Artemyev, A. V., Bale, S. D., Bonnell, J. W., and Mozer, F. S. (2020). On quasi-parallel whistler waves in the solar wind. *Physics of Plasmas*, 27(8):082902.

[Vasko et al., 2022] Vasko, I. Y., Mozer, F. S., Bale, S. D., and Artemyev, A. V. (2022). Ion-Acoustic Waves in a Quasi-Perpendicular Earth's Bow Shock. *Geophys. Res. Lett.*, 49(11):e98640.

[Vasko et al., 2018b] Vasko, I. Y., Mozer, F. S., Krasnoselskikh, V. V., Artemyev, A. V., Agapitov, O. V., Bale, S. D., Avanov, L., Ergun, R., Giles, B., Lindqvist, P.-A., Russell, C. T., Strangeway, R., and Torbert, R. (2018b). Solitary Waves Across Supercritical Quasi-Perpendicular Shocks. *Geophys. Res. Lett.*, 45:5809–5817.

[Vedenov et al., 1962] Vedenov, A. A., Velikhov, E., and Sagdeev, R. (1962). Quasilinear theory of plasma oscillations. *Nuclear Fusion Suppl.*, 2:465–475.

[Veltri and Zimbardo, 1993] Veltri, P. and Zimbardo, G. (1993). Electron-whistler interaction at the Earth's bow shock: 2. Electron pitch angle diffusion. *J. Geophys. Res.*, 98:13335–13346.

[Verkhoglyadova et al., 2010] Verkhoglyadova, O. P., Tsurutani, B. T., and Lakhina, G. S. (2010). Properties of obliquely propagating chorus. *Journal of Geophysical Research (Space Physics)*, 115(1):A00F19.

[Verkhoglyadova et al., 2013] Verkhoglyadova, O. P., Tsurutani, B. T., and Lakhina, G. S. (2013). Theoretical analysis of Poynting flux and polarization for ELF-VLF electromagnetic waves in the Earth's magnetosphere. *Journal of Geophysical Research (Space Physics)*, 118(12):7695–7702.

[Verscharen et al., 2022] Verscharen, D., Chandran, B. D. G., Boella, E., Halekas, J., Innocenti, M. E., Jagarlamudi, V. K., Micera, A., Pierrard, V., Štverák, Š., Vasko, I. Y., Velli, M., and Whittlesey, P. L. (2022). Electron-Driven Instabilities in the Solar Wind. *Frontiers in Astronomy and Space Sciences*, 9:951628.

[Voshchepynets et al., 2015] Voshchepynets, A., Krasnoselskikh, V., Artemyev, A., and Volokitin, A. (2015). Probabilistic model of beam-plasma interaction in randomly inhomogeneous plasma. *The Astrophysical Journal*, 807(1):38.

[Vu et al., 2022a] Vu, A., Liu, T. Z., Zhang, H., and Delamere, P. (2022a). Hybrid Simulations of a Tangential Discontinuity-Driven Foreshock Bubble Formation in Comparison With a Hot Flow Anomaly Formation. *Journal of Geophysical Research (Space Physics)*, 127(6):e29973.

[Vu et al., 2022b] Vu, A., Liu, T. Z., Zhang, H., and Delamere, P. (2022b). Hybrid Simulations of a Tangential Discontinuity-Driven Foreshock Bubble Formation in Comparison With a Hot Flow Anomaly Formation. *Journal of Geophysical Research (Space Physics)*, 127(6):e29973.

[Wang et al., 2020] Wang, R., Vasko, I. Y., Mozer, F. S., Bale, S. D., Artemyev, A. V., Bonnell, J. W., Ergun, R., Giles, B., Lindqvist, P. A., Russell, C. T., and Strangeway, R. (2020). Electrostatic Turbulence and Debye-scale Structures in Collisionless Shocks. *Astrophys. J. Lett.*, 889(1):L9.

[Webb et al., 1983] Webb, G. M., Axford, W. I., and Terasawa, T. (1983). On the drift mechanism for energetic charged particles at shocks. *Astrophys. J.* , 270:537–553.

[Wilson, 2016] Wilson, L. B. (2016). Low Frequency Waves at and Upstream of Collisionless Shocks. *Washington DC American Geophysical Union Geophysical Monograph Series*, 216:269–291.

[Wilson et al., 2013] Wilson, L. B., Koval, A., Szabo, A., Breneman, A., Cattell, C. A., Goetz, K., Kellogg, P. J., Kersten, K., Kasper, J. C., Maruca, B. A., and Pulupa, M. (2013). Electromagnetic waves and electron anisotropies downstream of supercritical interplanetary shocks. *J. Geophys. Res.*, 118:5–16.

[Wilson et al., 2014] Wilson, L. B., Sibeck, D. G., Breneman, A. W., Contel, O. L., Cully, C., Turner, D. L., Angelopoulos, V., and Malaspina, D. M. (2014). Quantified energy dissipation rates in the terrestrial bow shock: 2. Waves and dissipation. *J. Geophys. Res.*, 119:6475–6495.

[Wilson et al., 2016a] Wilson, L. B., Sibeck, D. G., Turner, D. L., Osmane, A., Caprioli, D., and Angelopoulos, V. (2016a). Relativistic Electrons Produced by Foreshock Disturbances Observed Upstream of Earth's Bow Shock. *Physical Review Letters*, 117(21):215101.

[Wilson et al., 2016b] Wilson, L. B., Sibeck, D. G., Turner, D. L., Osmane, A., Caprioli, D., and Angelopoulos, V. (2016b). Relativistic Electrons Produced by Foreshock Disturbances Observed Upstream of Earth's Bow Shock. *Phys. Rev. Lett.*, 117(21):215101.

[Wilson et al., 2012] Wilson, III, L. B., Koval, A., Szabo, A., Breneman, A., Cattell, C. A., Goetz, K., Kellogg, P. J., Kersten, K., Kasper, J. C., Maruca, B. A., and Pulupa, M. (2012). Observations of electromagnetic whistler precursors at supercritical interplanetary shocks. *Geophys. Res. Lett.*, 39:8109.

[Wilson et al., 2018] Wilson, III, L. B., Stevens, M. L., Kasper, J. C., Klein, K. G., Maruca, B. A., Bale, S. D., Bowen, T. A., Pulupa, M. P., and Salem, C. S. (2018). The Statistical Properties of Solar Wind Temperature Parameters Near 1 au. *Astrophys. J. Supp.*, 236:41.

[Yao et al., 2021] Yao, S. T., Shi, Q. Q., Zong, Q. G., Degeling, A. W., Guo, R. L., Li, L., Li, J. X., Tian, A. M., Zhang, H., Yao, Z. H., Fu, H. S., Liu, C. M., Sun, W. J., Niu, Z., Li, W. Y., Liu, Z. Y., Le Contel, O., Zhang, S., Xiao, C., Shang, W. S., Torbert, R. B., Ergun, R. E., Lindqvist, P. A., and Pollock, C. J. (2021). Low-frequency Whistler Waves Modulate Electrons and Generate Higher-frequency Whistler Waves in the Solar Wind. *Astrophys. J.* , 923(2):216.

[Zhang et al., 2022] Zhang, H., Zong, Q., Connor, H., Delamere, P., Facskó, G., Han, D., Hasegawa, H., Kallio, E., Kis, Á., Le, G., Lembège, B., Lin, Y., Liu, T., Oksavik, K., Omidi, N., Otto, A., Ren, J., Shi, Q., Sibeck, D., and Yao, S. (2022). Dayside Transient Phenomena and Their Impact on the Magnetosphere and Ionosphere. *Space Sci. Rev.*, 218(5):40.

[Zhang et al., 2018a] Zhang, X., Angelopoulos, V., Artemyev, A. V., and Liu, J. (2018a). Whistler and Electron Firehose Instability Control of Electron Distributions in and Around Dipolarizing Flux Bundles. *Geophys. Res. Lett.*, 45:9380–9389.

[Zhang et al., 2021] Zhang, X., Angelopoulos, V., Artemyev, A. V., Zhang, X.-J., and Liu, J. (2021). Beam Driven Electron Cyclotron Harmonic Waves in Earth's Magnetotail. *Journal of Geophysical Research (Space Physics)*, 126(3):e28743.

[Zhang et al., 2020] Zhang, X. J., Agapitov, O., Artemyev, A. V., Mourenas, D., Angelopoulos, V., Kurth, W. S., Bonnell, J. W., and Hospodarsky, G. B. (2020). Phase Decoherence Within Intense Chorus Wave Packets Constrains the Efficiency of Nonlinear Resonant Electron Acceleration. *Geophys. Res. Lett.*, 47(20):e89807.

[Zhang et al., 2019] Zhang, X. J., Mourenas, D., Artemyev, A. V., Angelopoulos, V., Bortnik, J., Thorne, R. M., Kurth, W. S., Kletzing, C. A., and Hospodarsky, G. B. (2019). Nonlinear Electron Interaction With Intense Chorus Waves: Statistics of Occurrence Rates. *Geophys. Res. Lett.*, 46(13):7182–7190.

[Zhang et al., 2018b] Zhang, X. J., Thorne, R., Artemyev, A., Mourenas, D., Angelopoulos, V., Bortnik, J., Kletzing, C. A., Kurth, W. S., and Hospodarsky, G. B. (2018b). Properties of Intense Field-Aligned Lower-Band Chorus Waves: Implications for Nonlinear Wave-Particle Interactions. *Journal of Geophysical Research (Space Physics)*, 123(7):5379–5393.